DEPARTMENT OF PHYSICS
UNIVERSITY OF JYVÄSKYLÄ
RESEARCH REPORT No. 10/2013

DEVELOPMENT AND USE OF COMPUTATIONAL TOOLS FOR MODELLING NEGATIVE HYDROGEN ION SOURCE EXTRACTION SYSTEMS

BY
TANELI KALVAS

Academic Dissertation
for the Degree of
Doctor of Philosophy

To be presented, by permission of the
Faculty of Mathematics and Natural Sciences
of the University of Jyväskylä,
for public examination in Auditorium FYS1 of the
University of Jyväskylä on December 5th, 2013
at 12 o'clock noon

Jyväskylä, Finland
December 2013

Preface

The work reported in this thesis was conducted in the Plasma and Ion Source Technology Group at the Lawrence Berkeley National Laboratory (LBNL) in Berkeley, California during years 2004–2006 and at the Department of Physics of the University of Jyväskylä (JYFL) during years 2007–2013. During this time I have worked on a wide range of projects, mostly related to production and extraction of ions and electrons. On this thesis I have mainly concentrated on selected negative hydrogen ion extraction projects and the development of the ion optical modelling tool IBSimu.

First, I want to sincerely thank my thesis supervisor and friend Dr. Olli Tarvainen for all the help and guidance in the magical world of ion "sourcery". Very special thanks also go to my other supervisor Dr. Ari Virtanen for providing me the opportunity to work in this fascinating field and all the support he has given me during these years. I would like to thank Dr. Marco Cavenago and Dr. Lawrence Rybarcyk for reviewing my thesis and for the suggestions and comments, which helped to improve it.

I would like to thank all the members of the LBNL group and especially Prof. Ka-Ngo Leung, Dr. Sami Hahto and Dr. Jani Reijonen for presenting the need for charged particle modelling capabilities, which did not exist at the time. In this situation the first crude simulations were made, which finally, after some years, led to the work presented here. In Jyväskylä I have had the pleasure of working with the ion source group — I want to thank Dr. Hannu Koivisto for making it possible. I also want to thank all the past and current group members, especially Dr. Juha Ärje, Mr. Jani Komppula, Mr. Janne Laulainen, Mr. Risto Kronholm, Dr. Tommi Ropponen and Dr. Ville Toivanen, for the the years of collaboration. Dr. Jan Sarén is gratefully acknowledged for the numerous brainstorming sessions a.k.a. lunch breaks.

Special thanks goes to Dr. Henry Clark, who provided the first stimulus to direct my simulation efforts towards negative ion extraction systems. I also wish to thank Dr. Jacques Lettry, Mr. Øystein Midttun, Dr. Martin Stockli, Dr. Robert Welton, Dr. Timo Sajavaara, Mr. Mikko Laitinen and Mr. Jaakko Julin for collaboration during the work.

I would like to thank Mr. Veikko Nieminen and Mr. Juha Tuunanen for engineering and the personnel of the electrical and mechanical workshops for helping to realize the charged particle sources used in this work. I wish to express my gratitude to Dr. Pekka Koskinen for helping me with the manuscript and to Ms. Ulrika Jakobsson for the introduction to the field of nuclear physics.

I would like to thank my parents for all the support and encouragement. I thank my lovely daughters, Ronja and Milla for providing a counterbalance to the world of physics. Finally, I want to thank my beloved wife Kaisa for the perseverance during these years.

The work presented in this thesis was supported by the Academy of Finland under the Finnish Center of Excellence in Nuclear and Accelerator Based Physics Research Programmes 2006–2011 and 2012–2017 and the U.S. Department of Energy under contract No. DE-AC02-05CH11231. Also the financial support from Emil Aaltonen Foundation and Finnish Academy of Science and Letters (Viljo, Yrjö ja Kalle Väisälän Rahasto) is gratefully acknowledged.

Jyväskylä, December 2013

Taneli Kalvas

Abstract

Kalvas, Taneli, 1981–
Development and use of computational tools for modelling negative hydrogen ion source extraction systems
Jyväskylä, University of Jyväskylä, 2013, 159 p.
Department of Physics Research Report No. 10/2013
ISBN paper copy: 978-951-39-5420-8
ISBN PDF: 978-951-39-5421-5
ISSN: 0075-465X

A computational tool for modelling extraction of positive and negative ion beams and electron beams from plasma sources has been developed. The code utilizes an iteration cycle to find a self-consistent solution satisfying the time-independent non-linear Poisson-Vlasov system of equations in three-dimensional, two-dimensional and cylindrically symmetric bound geometries. The computational methods used in the gun-type code are thoroughly presented and analyzed. The convergence characteristics of the iteration cycle are shown and the error sources in simulations are analyzed.

Three completely new negative hydrogen ion extraction systems designed with the simulation tool are presented: (1) Texas A&M University Cyclotron Institute H^-/D^- ion source extraction, which was built and is successfully providing beams to the cyclotron, (2) extraction of the University of Jyväskylä Pelletron H^- ion source PELLIS, which was thoroughly characterized with current and emittance measurements and (3) extraction of the University of Jyväskylä RF H^- ion source RADIS, which is still under development. The simulation tool is also used to analyze the baseline extraction system and a newly proposed high-current low-emittance extraction of the United States Spallation Neutron Source H^- ion source. The simulations are compared to experiments where applicable. The simulated emittances agree well with measurements in flat and convex plasma sheath conditions, but diverge from the observations when plasma sheath becomes highly concave. It is suspected that this is a result of the variation of current density arriving to the plasma sheath as a function of the local slope of the sheath, which results from the planar definition of the plasma flux at the simulation boundary.

Despite of the shortcomings of this type of codes, the results suggest that gun-type codes such as the one developed in this work can be used for modelling and designing new extraction systems with good confidence in the correct parameter space.

Keywords: Computer modelling, beam formation, ion extraction, negative hydrogen ion, ion source, ion optics, beam transport

Author Mr. Taneli Kalvas
Department of Physics
University of Jyväskylä
Jyväskylä, Finland

Supervisors Dr. Olli Tarvainen
Department of Physics
University of Jyväskylä
Jyväskylä, Finland

Dr. Ari Virtanen
Department of Physics
University of Jyväskylä
Jyväskylä, Finland

Reviewers Dr. Marco Cavenago
Laboratori Nazionali di Legnaro
Legnaro, Italy

Dr. Lawrence J. Rybarcyk
Los Alamos
New Mexico, USA

Opponent Dr. Edwin Chacon-Golcher
Insitut de Recherche Mathématique Avancée
Strasbourg
Alsace, France

Contents

Chapter 1

Introduction

Particle accelerators, from the cathode-ray tubes and the first four-inch cyclotron built by Earnst Lawrence in Berkeley, California in the 1930s [1] to CERN's 27-km-circumference Large Hadron Collider, have been traditionally built as tools for basic science. The discoveries of nuclear and particle physics would not have been possible without them and even more explorations lie ahead in the fields of neutron and photon sciences, for example. During the last decades the number of machines used for applications has increased rapidly. Possible future energy production methods, such as inertial and magnetic confinement fusion and accelerator driven systems for fission, rely heavily on accelerator technology. Also industrial and medical fields use the devices in semiconductor device manufacturing, hadron therapy cancer treatment and medical isotope production, for example. Currently there are more than 30 000 particle accelerators operating with ions in the world and in every case, the first and quite probably the most critical part of the whole system, is the *ion source* and its beam extraction system. [2]

Even though it is more difficult to produce negative ions than positive ions, some accelerators use them to facilitate so-called double stripping process for converting negative ions to positive at some stage. In cyclotrons, for example at University of Jyväskylä, Department of Physics (JYFL), this is done for extracting energetic H^-/D^- as protons/deuterons from the accelerator with high efficiency, avoiding activation of the machine [3]. In large proton storage rings the same phenomenon is used in so-called charge exchange injection [4] to fill the ring efficiently using H^- ions converted to protons. Due to opposite curvature of circulating and injected beams it is possible to accumulate beam bunches in the ring, enabling high peak intensities of consequent beam. Large-scale facilities using such method include Japan Proton Accelerator Research Complex (J-PARC); Spallation Neutron Source at Oak Ridge National Laboratory, USA (SNS); Fermilab, USA; Los Alamos Neutron Science Center (LANSCE), USA and CERN, France/Switzerland after the future Linac4 upgrade. A third type of accelerator utilizing stripping of negative ions is the tandem accelerator [5]. It

first accelerates negative beam to a positive high voltage terminal, where the ions are stripped to a positive charge state and then accelerated back to the laboratory ground potential. The use of negative ions in tandem accelerators makes it possible to achieve at least double the energy that would be available to positive ions using a conventional single-stage high voltage accelerator. It also allows the convenience of having both ion source and target close to the ground potential. Negative ions of hydrogen and deuterium are also used in neutral beam plasma heating systems of magnetic confinement fusion plasma devices, for example, the ITER tokamak experimental reactor [6]. In this case negative ions are chosen instead of positive due to higher neutralization efficiency at high energies needed for the neutral beam.

The work done in this thesis brings new methods and simulation tools available for the scientific community for designing and modelling extraction systems for negative hydrogen ion sources. The new three-dimensional simulation tool, IBSimu — Ion Beam Simulator, enables modelling of the beam extraction from the ion source plasma in presence of magnetic field and calculation of the low energy beam transport (LEBT) including the dumping of the co-extracted electrons in a single simulation. Previously such designs have been made using separate simulation codes modelling beam formation in cylindrically symmetric geometry and magnetic deflection of electrons in 2D or 3D with questionable or non-existent modelling of space charge forces. This type of modelling completely neglects the effects of the magnetic field on the negative ions and often requires additional approximations if the extraction geometry is not cylindrically symmetric. Now with the new three-dimensional tool it is possible to model extraction systems with fewer approximations and higher level of confidence.

The thesis is divided in the following way: First, basic plasma physics and operation principle of ion sources is introduced in chapters 2 and 3. Chapter 4 discusses ion optics and beam extraction from plasma ion sources. In chapter 5 the computer simulation methods developed in this work are described. Chapter 6 descibes extraction systems designed using the tools developed together with experimental observations. Finally, in chapter 7 the conclusions of the work are drawn. Appendices A and B list commonly used symbols and input parameters of the simulation code, respectively. In appendix C methods for two dimensional modelling are described.

This thesis is partially based on work previously published by the author. The extraction system designs and experimental work on them (chapter 6) have been presented in references [7, 8, 9, 10] and chapter 4 is based on reference [11]. The analysis of the simulation methods (chapter 5) has not been published prior to this thesis.

Chapter 2

Basic plasma properties

Originally the word *plasma*, which was coined by Irving Langmuir, was used for describing a low-pressure gas discharge "carrying" positive and negative charged particles in a similar manner as blood plasma carries the red and white cells in blood [12]. More precisely, plasma is a collection of ionized matter consisting of electrons, ions and neutral particles. For a more formal definition, we need to define the so-called plasma criteria in the next section. A low-pressure gas discharge is just one example of a laboratory created plasma. The most known examples of natural plasmas are the stars, solar wind and lightning strokes. Human-made plasmas are used nowadays in a large variety of applications including semiconductor manufacturing, magnetic confinement fusion and plasma cutters for metal working.

In most of the existing ion sources the charged particles of the extracted beam are either created in a plasma or at least transported through a plasma before forming the beam. Thus, it is obvious that the properties of the plasma have an effect on the beam properties.

2.1 Thermal properties of gases and plasmas

According to the kinetic theory of gases, the velocity distribution of particles in gas follows the Maxwell-Boltzmann (MB) distribution

$$f(v_x, v_y, v_z) = n \left(\frac{m}{2\pi kT}\right)^{3/2} \exp\left(-\frac{m(v_x^2 + v_y^2 + v_z^2)}{2kT}\right), \tag{2.1}$$

where n is the particle density, m is the particle mass, k is the Boltzmann constant, T is the temperature and v_x, v_y and v_z are the particle velocity components. As the temperature of gas increases the width of the distribution becomes broader. Due to

the tail of the distribution there are always some particles which have high enough velocity to cause ionization in a finite temperature gas. At very high temperatures the fraction of ionized material becomes large enough for the volume of material to show plasma behaviour. Also the charged particles interact with each other and the neutrals via numerous elastic collisions and therefore they also have a tendency towards Maxwell-Boltzmann distribution. From (2.1), one can calculate that the mean velocity of particles

$$\langle v \rangle = \sqrt{\frac{8kT}{\pi m}}, \tag{2.2}$$

and the mean kinetic energy of particles

$$\langle E_K \rangle = \frac{3}{2} kT, \tag{2.3}$$

which is divided equally between the coordinate directions, i.e.

$$\langle E_{K,x} \rangle = \langle E_{K,y} \rangle = \langle E_{K,z} \rangle = \frac{1}{2} kT. \tag{2.4}$$

It is common that temperatures are defined in electron volts instead of Kelvins, using the relation (2.4) and dropping the dimension dependent coefficient. Therefore

$$E_K = kT, \tag{2.5}$$

which gives that 1 eV corresponds to about 11600 K.

Usually laboratory plasmas are not really in thermal equilibrium: plasma particles constantly interact with boundaries, photons carry away energy from the plasma and the plasma is often being driven by a power source destroying the equilibrium assumed for MB-distribution. Under typical hydrogen ion source plasma conditions, the ionization degree is about one percent. The neutral particles, electrons and different ion species all interact differently with each other and with the boundaries and therefore all the particle species have their own unique velocity distributions. Typically Maxwellian distributions and temperatures are used to describe the velocities of each particle species nevertheless.

2.2 Plasma criteria

For a collection of particles to be considered as plasma, three conditions must be fulfilled: 1) the so-called Debye length is smaller than the size of the plasma, 2) number of particles inside Debye sphere is large and 3) plasma frequency must be larger than the average electron-neutral collision frequency [13].

2.2.1 Debye length

When neutral gas is ionized, equal amounts of free positive and negative charge are created. Therefore

$$\sum_i Q_i n_i - n_e = 0, \tag{2.6}$$

where Q_i are the charge states of ion species, n_i are the densities of ion species and n_e is the electron density. This condition is called quasineutrality, meaning that the neutrality condition is fulfilled over macroscopic distances. If this would not be the case, strong electric fields would quickly disperse the charged particles. In atomic scale the charge distribution is obviously not flat because of discrete nature of charges, but also in microscopic scales there may be local deviations from the neutrality for example due to thermal fluctuations or external perturbation. Deviations in charge distribution of plasma will be shielded by redistribution of the surrounding charges. The shielded potential around a point-like charge q in a plasma is commonly known as the *Debye potential*

$$\phi(r) = \frac{q}{4\pi\epsilon_0 r} \exp\left(-\frac{\sqrt{2}r}{\lambda_D}\right), \tag{2.7}$$

where ϵ_0 is the vacuum permittivity, r is the distance from the charge and

$$\lambda_D = \sqrt{\frac{\epsilon_0 kT}{n_e e^2}} \tag{2.8}$$

is the *Debye length*, where e is the elementary charge [14]. Debye length is roughly the length-scale for the volume of charge imbalance around a perturbation. If an electrically conducting object, an electrode, is immersed in the plasma, a *plasma sheath* will be formed around it, which has a thickness on the order of the Debye length. For plasma to be neutral over macroscopic distances, the plasma dimension denoted as L, must be larger than the Debye length. Therefore

$$L \gg \lambda_D \tag{2.9}$$

is the first plasma criterion.

The average number of particles inside a sphere of λ_D radius, known as the *Debye sphere*, is

$$\Lambda = \frac{4}{3}\pi\lambda_D^3 n_e = \frac{4\pi}{3}\left(\frac{\epsilon_0 kT}{n_e^{1/3} e^2}\right)^{3/2}, \tag{2.10}$$

where Λ is also known as the *plasma parameter*. For a plasma with electron density $n_e = 10^{18}$ and temperature $T_e = 1.5$ eV the plasma parameter $\Lambda = 3161$. As the plasma parameter range of naturally occuring and laboratory plasmas is very wide it is more practical to use $\log\Lambda$ instead. For the example presented here $\log\Lambda = 8.1$.

In many cases physical phenomena (such as collision processes presented below) are dependent on $\log \Lambda$, often referred as Coulomb logarithm.

Because the Debye shielding arises from collective behaviour of charged particles, it is required that the sphere contains a large number of particles. Therefore

$$n_e \lambda_D^3 \gg 1 \tag{2.11}$$

is the second criterion for achieving plasma behavior. Together the first two plasma criteria can be stated as

$$\frac{1}{n_e^{1/3}} \ll \lambda_D \ll L. \tag{2.12}$$

In other words the Debye length must be much larger than the average distance between electrons and much smaller than the size of the plasma.

2.2.2 Plasma frequency

If a plasma is disturbed by locally changing the space charge neutrality, an electric field will be generated. This results in collective behaviour of charged particles trying to restore the neutrality. Because of the large mass difference between the electrons and the ions, the electrons will react faster to the field and, to a first approximation, the ions will stay stationary. Because of inertia of the electrons, there will be an oscillation of electrons around the disturbance with a natural (angular) frequency

$$\omega_{pe} = \sqrt{\frac{n_e e^2}{\epsilon_0 m_e}} \tag{2.13}$$

known as the *plasma frequency*, where m_e is the electron mass.

The plasma oscillation is damped by collisions of the electrons with neutral particles. For the plasma to exhibit collective behaviour, the collision frequency must be less than the frequency of the plasma oscillation ($\nu_{pe} = \omega_{pe}/2\pi$). This leads to the third plasma criterion

$$\nu_{pe} > \nu_{en}, \tag{2.14}$$

where ν_{en} is the electron-to-neutral collision frequency. If the collision frequency is higher, the behaviour is dominated by collisions similar to a neutral gas. In practice (2.14) sets a lower limit to the ionization degree of the plasma.

2.3 Collisions in plasma

In many cases, interesting physics can be understood by making a simplification assuming that the plasma is collisionless. This approximation is most accurate in the

case of sparse plasmas but strictly speaking collisionless plasmas do not exist. In some cases it is necessary to take into account the collisions, because the phenomena being studied, such as particle diffusion, are dependent on collisions.

Collisions of charged particles can be divided into two categories: collisions with neutral particles and collisions with other charged particles. From the ratio of these collision types, collisional plasmas are divided into two types: (1) weakly ionized plasmas, where charged-neutral collisions are dominant and (2) highly ionized plasmas, where the charged-charged collisions dominate. Because of the long range of the Coulomb interaction the charged-charged collisions tend to dominate already when the ionization degree is only a few percent. Above this limit the plasma is considered to be highly ionized or fully ionized, even though the ionization degree is often not 100 %.

2.3.1 Weakly ionized plasma

In weakly ionized plasmas most of the interactions are direct neutral-neutral collisions and direct charged-neutral collisions. The interactions may be elastic, in which the total kinetic energy of particles is conserved and the processes drive the particles towards thermodynamic equilibrium. On the other hand, if the kinetic energy of the particles is high enough, the interaction may be inelastic leading to excitation or ionization of particles.

At the typical hydrogen ion source electron energies (< 100 eV) the total cross section σ_{en} for electron-hydrogen molecule collision processes is roughly 10^{-19} m^2 [15]. The average collision frequency of a charged particle can be calculated using

$$\langle \nu_{en} \rangle = n_n \sigma_{en} \langle v_e \rangle, \tag{2.15}$$

which gives 8 MHz for $T_e = 1.5$ eV electrons with $n_n = 1.2 \cdot 10^{20}$ m^{-3} neutral density (corresponding to a typical hydrogen ion source with 0.5 Pa pressure at 300 K). To understand better the electron behaviour in the plasma, it is convenient to define the mean-free-path

$$\lambda_{\mathrm{mfp}} = \frac{\langle v_e \rangle}{\langle \nu_{en} \rangle} = \frac{1}{n_n \sigma_{en}}, \tag{2.16}$$

which for the given example corresponds to a mean-free-path of 0.1 m, which is on the order of the typical ion source plasma size.

2.3.2 Fully ionized plasma

The collisions in highly ionized plasmas differ from the weakly ionized case. The elastic scattering cross section is much higher because of the long range of the Coulomb force

acting between the charged particles, even though the interaction length is limited by the shielding effect of the plasma. In fact, the small-angle deflections happening at relatively long distances are so much more frequent than the large-angle collisions that the cumulative effect of such deflections turns out to be more significant than the effect of the fewer large-angle interactions. To be able to compare the cross-section of the electron-ion collision process to a charged-neutral process, a cross-section formula has been derived for the cumulative collision process [16]:

$$\sigma_{ei} = \frac{Q_i^2 e^4 \log \Lambda}{4\pi\epsilon_0 m_e^2 v^4}. \tag{2.17}$$

Assuming the Maxwell-Boltzmann distribution for the electrons an average collision frequency can be derived as

$$\langle \nu_{ei} \rangle = n_i \sigma_{ei} \langle v_e \rangle = \frac{\sqrt{2} n_i Q_i^2 e^4 \log \Lambda}{12\pi^{3/2}\epsilon_0^2 \sqrt{m_e}(kT_e)^{3/2}}. \tag{2.18}$$

In addition to the electron-ion collisions also electron-electron and ion-ion collisions take place. The collision frequencies for these processes can be approximated as [16]

$$\langle \nu_{ee} \rangle \approx \frac{\langle \nu_{ei} \rangle}{n_i Q_i^2 / n_e} \tag{2.19}$$

and

$$\langle \nu_{ii} \rangle = \frac{n_i Q_i^4 e^4 \log \Lambda}{12\pi^{3/2}\epsilon_0^2 \sqrt{M}(kT_i)^{3/2}}, \tag{2.20}$$

where $M = m_1 m_2/(m_1 + m_2)$ is the reduced mass in the collision of ions with masses m_1 and m_2.

In a typical hydrogen ion source plasma, the average collision frequencies can be calculated as $\langle \nu_{ii} \rangle \approx 300$ kHz, $\langle \nu_{ei} \rangle \approx 13$ MHz using $T = 1.5$ eV and $n_e = n_i = 10^{18}$ m^{-3}. Because the average charge state in a hydrogen ion source is very close to 1, the electron-electron collison rate $\langle \nu_{ee} \rangle \lesssim \langle \nu_{ei} \rangle$. Comparing the electron-electron and electron-ion collision frequencies to the electron-neutral collision frequency of 8 MHz calculated before, we can see that for electrons the charged particle collisions are about as significant as the neutral collisions in a plasma with the assumed 1 % ionization degree.

2.4 Plasma-wall interactions

In all laboratory plasmas there exists a boundary for the plasma: the vacuum vessel wall. Most of the time the wall is considered as a sink of particles even though it may also act as a source of charged and neutral particles through secondary electron and

ion emission, wall sputtering, formation of negative ions through surface conversion and other processes. These subjects are discussed in more detail in the next chapter. In this chapter only the simplified behaviour of the plasma near the wall is considered.

2.4.1 Plasma sheath

Because of the higher mobility, electron flux out of the plasma tends to be larger than the ion flux. If the vessel walls are kept at fixed potential ϕ_W, the plasma will assume a positive potential with respect to the walls to compensate for the difference in the flux. An equilibrium will form at equal flux of positive and negative charge in order for the plasma to stay quasineutral. A plasma sheath with a thickness on the order of λ_D is formed at the plasma-wall interface, in which the most of the potential drop takes place [17].

The simplest description of the plasma sheath is given by Bohm for a singly charged ion-electron plasma [17, 18]: The density of ions in the sheath can be calculated by assuming a monoenergetic flux of ions arriving to the sheath with velocity v_0 and by assuming a quasineutral situation $n_0 = n_i = n_e$ at sheath edge at $\phi_S = 0$ V. Using ion continuity $n_0 v_0 = n_i v_i$ and energy conservation $m_i v_i^2/2 - e\phi = m_i v_0^2/2$ the ion density becomes

$$n_i = n_0 \sqrt{1 + \frac{2e\phi}{m_i v_0^2}}. \tag{2.21}$$

The electrons are assumed to be in thermal equilibrium and therefore their density is given by the MB-distribution

$$n_e = n_0 \exp\left(-\frac{e\phi}{kT_e}\right). \tag{2.22}$$

The potential in the sheath is described by the Poisson equation

$$\frac{d^2\phi}{dx^2} = -\frac{(n_i - n_e)e}{\epsilon_0} = -\frac{en_0}{\epsilon_0}\left[\sqrt{1 + \frac{2e\phi}{m_i v_0^2}} - \exp\left(-\frac{e\phi}{kT_e}\right)\right]. \tag{2.23}$$

The Poisson equation is impossible to solve analytically and often numerical approach or approximations are used even in the presented one-dimensional case. An important feature can be observed from the equation: the shielding condition in the sheath is only fulfilled when the space charge is non-negative, i.e. $n_i \geq n_e$ for all $\phi \leq 0$. This necessary condition

$$v_0 \geq v_B = \sqrt{\frac{kT_e}{m_i}} \tag{2.24}$$

is known as the *Bohm sheath criterion* and v_B as *Bohm velocity*. The criterion sets a low-velocity limit for ions arriving to the sheath edge and in most cases the equation

holds with equality [19]. In a typical case this is much higher than the average thermal velocity of ions. Therefore, there must be an electric field accelerating the ions in the plasma region preceding the sheath. This region is known as the *presheath*. The bulk plasma to sheath edge potential difference is therefore

$$\phi_P - \phi_S = \frac{kT_e}{2e}. \tag{2.25}$$

The potential variation close by to the electrode is sketched in figure 2.1.

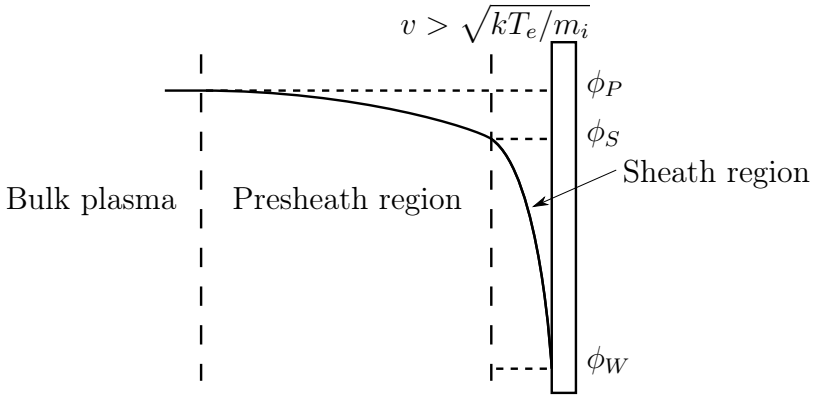

Figure 2.1: Potential variation near the plasma vessel wall.

2.4.2 Plasma potential

The ion flux in the sheath is defined by the Bohm velocity and plasma density at sheath edge to be

$$\Gamma_i = n_0 v_B \tag{2.26}$$

and it is assumed to be constant through the sheath. The electron flux at the wall is given by the impinging flux modified by the Boltzmann relation

$$\Gamma_e = \frac{1}{4} n_0 \langle v_e \rangle \exp\left(\frac{-e\phi_W}{kT_e}\right), \tag{2.27}$$

where $\langle v_e \rangle = (8kT_e/\pi m)^{1/2}$ is the average electron speed. Equalizing the particle fluxes and using (2.25) gives the plasma potential [20]

$$\phi_P - \phi_W = \frac{kT_e}{2e}\left(1 + \log\left(\frac{m_i}{2\pi m_e}\right)\right). \tag{2.28}$$

For example, calculating the plasma potential for a hydrogen plasma with $T_e = 5.0$ eV gives $\phi_P - \phi_W = 17$ V.

2.5 Magnetized plasmas

External magnetic fields, in addition to electric fields, can be used to control charged particles. Many ion sources use magnetic fields for plasma confinement for example.

2.5.1 Cyclotron frequency

The equation of motion of a charged particle is defined by the Lorentz force

$$\frac{d\vec{p}}{dt} = q(\vec{E} + \vec{v} \times \vec{B}), \tag{2.29}$$

where $\vec{p}$ is the particle momentum, $\vec{E}$ is the electric field and $\vec{B}$ is the magnetic field. Using Newton's second law in the absence of electric field at nonrelativistic velocities it becomes

$$\frac{d\vec{v}}{dt} = \frac{q}{m}(\vec{v} \times \vec{B}). \tag{2.30}$$

In a uniform field, the particle takes a helical orbit with gyro-motion in the plane perpendicular to the magnetic field with a radius

$$r_L = \frac{mv_\perp}{qB}, \tag{2.31}$$

which is known as the *gyroradius* or the *Larmor* radius. The velocity component parallel to the magnetic field is unaffected. The rotation frequency of the particle is known as the *cyclotron frequency* and it is

$$\omega_c = \frac{qB}{m}. \tag{2.32}$$

2.5.2 Magnetic confinement

Magnetic fields can be used to increase the life time of the charged particles in a limited size plasma by confinement. The most commonly used magnetic field configurations in ion sources are the magnetic bottle and the multicusp field shown in figure 2.2. In both of these configurations, the plasma is occupying the central volume with lower magnetic field and is surrounded by stronger field regions.

As a first approximation, when the spatial variation of B within the particle gyro-orbit is small compared to B, the particle's magnetic moment

$$\mu = \frac{1}{2}\frac{mv_\perp^2}{B} \tag{2.33}$$

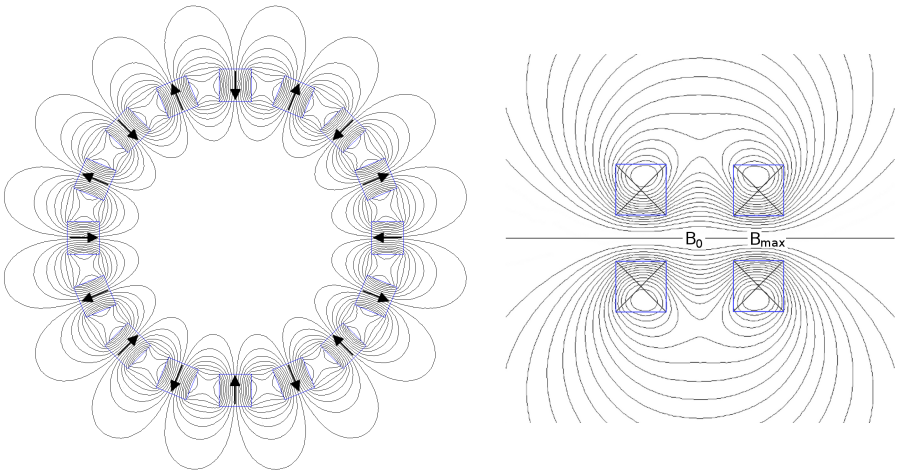

Figure 2.2: Most commonly used magnetic confinement configurations: Multicusp magnetic field with 16 poles on the left and magnetic bottle generated by two solenoids on the right.

can be considered to be constant, which is known as the first adiabatic invariant. Because of the conservation of the total kinetic energy E_k

$$\frac{1}{2}mv_{\parallel}^2 = E_k - \mu B. \tag{2.34}$$

From equation (2.34) and taking in account the first adiabatic invariant it can be seen that, as a particle with non-zero transverse velocity component moves towards stronger magnetic field region, the parallel velocity component $v_{\parallel}$ will decrease. If the magnetic field becomes strong enough, the parallel velocity component becomes zero and the particle will be reflected back. This phenomenon is called the *magnetic mirror effect* and it is the basis of magnetic plasma confinement. [16]

A solenoidal magnetic bottle is a major part of the magnetic confinement system of electron cyclotron resonance (ECR) ion sources, for example. The effectiveness of the system is measured by the mirror ratio $B_{\max}/B_0$, where $B_{\max}$ is the magnetic field maximum at the bottle ends and B_0 is the magnetic field at the center of the magnetic bottle. By defining the pitch angle $\alpha = \tan^{-1}(v_{\perp}/v_{\parallel})$ and using the first adiabatic invariant, a relation can be derived between the pitch angle at an arbitrary location and at the center of the bottle:

$$\frac{mv^2 \sin^2 \alpha_0}{2B_0} = \frac{mv^2 \sin^2 \alpha}{2B}. \tag{2.35}$$

At the end of the bottle the particles with positive parallel velocity ($\alpha < \pi/2$) at the magnetic field maximum will pass magnetic mirror. Therefore, the particles having a

pitch angle at the center greater than

$$\alpha_0 = \sin^{-1}(\sqrt{B_0/B_{\max}}) \tag{2.36}$$

will be trapped in the bottle.

In a traditional multicusp magnetic configuration, like used in many negative hydrogen ion sources, permanent magnets are placed around the plasma chamber with alternating poles facing towards the plasma. This produces a magnetic field structure with high magnetic field close to the plasma chamber walls and a low magnetic field in a relatively large volume inside the chamber for production and extraction of plasma particles.

The main particle losses in a multicusp ion sources happen along the cusp lines through particle diffusion and at surfaces, which are not covered by the multicusp field. The particle loss rate can be written as [21]

$$\frac{dn}{dt} = n\langle v\rangle \frac{S_{\text{cusp}} + S_{\text{surface}}}{V}, \tag{2.37}$$

where n is the plasma density, $\langle v\rangle$ is the average ion or electron velocity, S_{cusp} is the loss area along cusp lines, S_{surface} is the loss area for other surfaces and V is the plasma volume. The cusp line width w defining the loss area by $S_{\text{cusp}} = L_{\text{cusp}}w$, where L_{cusp} is the total length of cusp lines, is relatively hard to estimate. There are several papers dedicated to the matter [22, 23, 24]. An order-of-magnitude estimate of the loss width can be calculated from

$$w = 2\sqrt{r_{Le}r_{Li}}, \tag{2.38}$$

where r_{Le} is the Larmor radius of electrons and r_{Li} is the Larmor radius of ions in the average magnetic field at the cusp line [24]. For an electron with 1 eV perpendicular kinetic energy component in 1 T field, the $r_{Le} = 8$ μm, while for a proton $r_{Le} =$ 0.3 mm. The corresponding loss width $w = 0.1$ mm according to (2.38).

2.5.3 Charged particle diffusion in magnetic field

The collisions of the charged particles in plasmas play an especially important role in the case of a magnetized plasma. Without collisions for example a transverse magnetic field would be a perfect mirror for low energy charged particles. In collisional systems the particles follow their helical orbits from collision to collision and they can propagate through the transverse magnetic field by diffusion, as is illustrated in figure 2.3. While the collisions enhance the transport of particles in the transverse direction, they reduce the transport in the parallel direction.

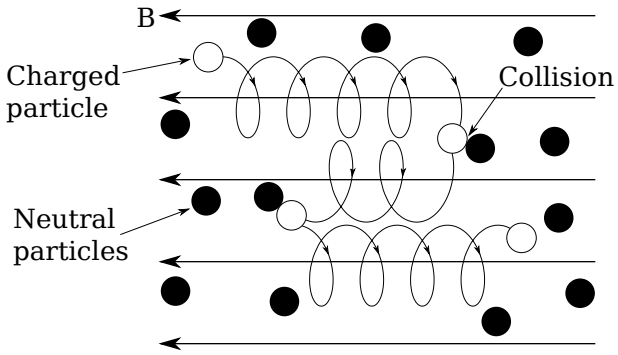

Figure 2.3: Diffusion of charged particle in magnetic field. Reproduced from reference [16].

Assuming that the mean free path between collisions is small compared to the size of the system, the particle motion can be described by the diffusion equation

$$\frac{\partial n}{\partial t} = \nabla \cdot (D \nabla n), \tag{2.39}$$

where n is the local particle density and D is the diffusion coefficient. In a non-magnetic system, where particles follow straight paths between collisions, the diffusion coefficient

$$D \approx \nu \lambda_{\text{mfp}}^2 \approx \frac{kT}{\nu m}. \tag{2.40}$$

In the case of magnetized plasma, the step size between each collision is different. In the transverse direction, assuming $2\pi r_L < \lambda_{\text{mfp}}$ the step size is of the order of r_L and the diffusion coefficient becomes

$$D_\perp \approx \nu r_L^2. \tag{2.41}$$

The average step size in the parallel direction is smaller than λ_{mfp} due to helical trajectory of the particle, but only by a small factor. Therefore, as an order-of-magnitude estimate, (2.40) is also valid for $D_\parallel$. [16]

Comparing the diffusion coefficient in transverse direction for electrons and ions, it can be seen that the ions diffuse faster than electrons due to their larger r_L. As a plasma must remain quasineutral, the particle fluxes must adjust to correct for the imbalance. The diffusion process, which results from the conservation of neutrality is called *ambipolar diffusion* and is described by a diffusion constant

$$D_\perp \approx \nu_{ei} \langle r_{Le}^2 \rangle \left(1 + \frac{T_i}{T_e}\right). \tag{2.42}$$

The electron-ion collision frequency ν_{ei} is proportional to $T_e^{-3/2}$ and the average electron Larmor radius

$$\langle r_{Le}^2 \rangle = \left\langle \frac{m_e^2 v_\perp^2}{q^2 B^2} \right\rangle \propto T_e. \tag{2.43}$$

In a typical case $(1 + T_i/T_e)$ is close to unity. Therefore the ambipolar diffusion coefficient $D_\perp$ is proportional to $T_e^{-1/2}$. The diffusion is slower for high electron temperature [16].

In negative ion sources, a transverse magnetic field is used as a filter for high temperature electrons, while cold electrons pass through the filter with positive ions due to diffusion. The situation in negative ion sources is more complicated than in the case of simple ambipolar diffusion due to the contribution of the significant H^- density to the charge balance. In some ion sources, the electron charge density in the filtered region can be as low as 2 % of the positive ion density, i.e. electrons are almost entirely replaced by negative ions [25]. In practice the complicated filter field phenomena are studied with numerical models [26].

Chapter 3

Ion sources

There are several types of ion sources for different applications. The ion sources are usually classified by the method of plasma or ion formation. In this work the main emphasis is on hot filament and radio frequency negative ion sources. The production mechanisms in these ion sources are discussed in this chapter. As a comparison, also ECR heating is introduced.

The details of the operational principle of an ion source depend on the type of the ion source, but generally most of the ion sources work in a similar way. The main part of an ion source is a chamber, which is evacuated constantly by pumping. The element which is to be ionized is introduced into the chamber in a controlled manner to maintain an optimal neutral density. In the simplest case, if the element is available as gas, it can be injected through a finely controlled valve. The chamber also contains a source of energetic electrons, which ionize the neutral particles and thus form a plasma. The ions can be pulled from the plasma generator by a high voltage at the extraction region to form an ion beam from the charged particles of the plasma.

3.1 Ionization

To form plasma, neutral particles need to be ionized i.e. all or part of their electrons must be detached. The various ways in which the ionization can be done, include electron impact ionization, ion impact ionization, photoionization, field ionization, surface ionization, etc. Whatever the ionization process, it needs to provide energy to overcome the binding energy of the electron. The first ionization energy, which is needed for ionizing a neutral atom $\mathrm{X} \rightarrow \mathrm{X}^{+} + e$, has been measured for most elements and is presented in figure 3.1. The ionization energies fall between 3.89 eV of caesium and 24.6 eV of helium. The ionization energy of hydrogen is 13.6 eV.

1 **H** 13.5984																	2 **He** 24.5874
3 **Li** 5.3917	4 **Be** 9.3227											5 **B** 8.298	6 **C** 11.2603	7 **N** 14.5341	8 **O** 13.6181	9 **F** 17.4228	10 **Ne** 21.5645
11 **Na** 5.1391	12 **Mg** 7.6462											13 **Al** 5.9858	14 **Si** 8.1517	15 **P** 10.4867	16 **S** 10.36	17 **Cl** 12.9676	18 **Ar** 15.7596
19 **K** 4.3407	20 **Ca** 6.1132	21 **Sc** 6.5615	22 **Ti** 6.8281	23 **V** 6.7462	24 **Cr** 6.7665	25 **Mn** 7.434	26 **Fe** 7.9024	27 **Co** 7.881	28 **Ni** 7.6398	29 **Cu** 7.7264	30 **Zn** 9.3942	31 **Ga** 5.9993	32 **Ge** 7.8994	33 **As** 9.7886	34 **Se** 9.7524	35 **Br** 11.8138	36 **Kr** 13.9996
37 **Rb** 4.1771	38 **Sr** 5.6949	39 **Y** 6.2173	40 **Zr** 6.6339	41 **Nb** 6.7589	42 **Mo** 7.092	43 **Tc** 7.28	44 **Ru** 7.3605	45 **Rh** 7.4589	46 **Pd** 8.3369	47 **Ag** 7.5762	48 **Cd** 8.9938	49 **In** 5.7864	50 **Sn** 7.3439	51 **Sb** 8.6084	52 **Te** 9.0096	53 **I** 10.4513	54 **Xe** 12.1298
55 **Cs** 3.8939	56 **Ba** 5.2117	57-71 Lantha- noids	72 **Hf** 6.8251	73 **Ta** 7.5496	74 **W** 7.864	75 **Re** 7.8335	76 **Os** 8.4382	77 **Ir** 8.967	78 **Pt** 8.9587	79 **Au** 9.2255	80 **Hg** 10.4375	81 **Tl** 6.1082	82 **Pb** 7.4167	83 **Bi** 7.2856	84 **Po** 8.417	85 **At** 9.3	86 **Rn** 10.7485
87 **Fr** 4.0727	88 **Ra** 5.2784	89-103 Acti- noids	104 **Rf**	105 **Db**	106 **Sg**	107 **Bh**	108 **Hs**	109 **Mt**	110 **Ds**	111 **Rg**	112 **Cn**						

Lanthanoids	57 **La** 5.5769	58 **Ce** 5.5387	59 **Pr** 5.473	60 **Nd** 5.525	61 **Pm** 5.582	62 **Sm** 5.6437	63 **Eu** 5.6704	64 **Gd** 6.1501	65 **Tb** 5.8638	66 **Dy** 5.9389	67 **Ho** 6.0215	68 **Er** 6.1077	69 **Tm** 6.1843	70 **Yb** 6.2542	71 **Lu** 5.4259
Actinoids	89 **Ac** 5.17	90 **Th** 6.3067	91 **Pa** 5.89	92 **U** 6.1941	93 **Np** 6.2657	94 **Pu** 6.0262	95 **Am** 5.9738	96 **Cm** 5.9915	97 **Bk** 6.1979	98 **Cf** 6.2817	99 **Es** 6.42	100 **Fm** 6.5	101 **Md** 6.58	102 **No** 6.65	103 **Lr** 4.9

Figure 3.1: First ionization energies in electron volts for most elements presented in a periodic table. Data from reference [27].

3.1.1 Electron impact ionization

The most common and probably the easiest way of ionizing neutral particles in laboratory conditions is by bombarding them with energetic electrons. If the element is monoatomic like noble gases, the process can simply be described as

$$\mathrm{X} + \mathrm{e} \rightarrow \mathrm{X}^+ + 2\mathrm{e}, \tag{3.1}$$

where X is the element ionized and e is a free electron. The probability of the ionization process varies with the incident electron energy. The cross-section rises from zero at the electron center-of-mass kinetic energy equal to the ionization energy and peaks at roughly 3–4 times the ionization energy. Some of the cross-sections for production of hydrogen, helium and oxygen ions are shown in figure 3.2.

In the case of hydrogen the ionization process is more complicated involving molecular ions H_2^+ and H_3^+ in addition to monoatomic H^+. The most common processes leading to production of ions in a hydrogen plasma include

$$\mathrm{H} + \mathrm{e} \rightarrow \mathrm{H}^+ + 2\mathrm{e}, \tag{3.2}$$

$$\mathrm{H}_2 + \mathrm{e} \rightarrow \mathrm{H}^+ + \mathrm{H} + 2\mathrm{e}, \tag{3.3}$$

$$\mathrm{H}_2 + \mathrm{e} \rightarrow \mathrm{H}_2^+ + 2\mathrm{e}, \tag{3.4}$$

$$\mathrm{H}_2^+ + \mathrm{e} \rightarrow \mathrm{H}^+ + \mathrm{H} + \mathrm{e}, \tag{3.5}$$

$$\mathrm{H}_2^+ + \mathrm{H}_2 \rightarrow \mathrm{H}_3^+ + \mathrm{H} \qquad \text{and} \tag{3.6}$$

$$\mathrm{H}_3^+ + \mathrm{e} \rightarrow \mathrm{H}^+ + 2\mathrm{H} + \mathrm{e}. \tag{3.7}$$

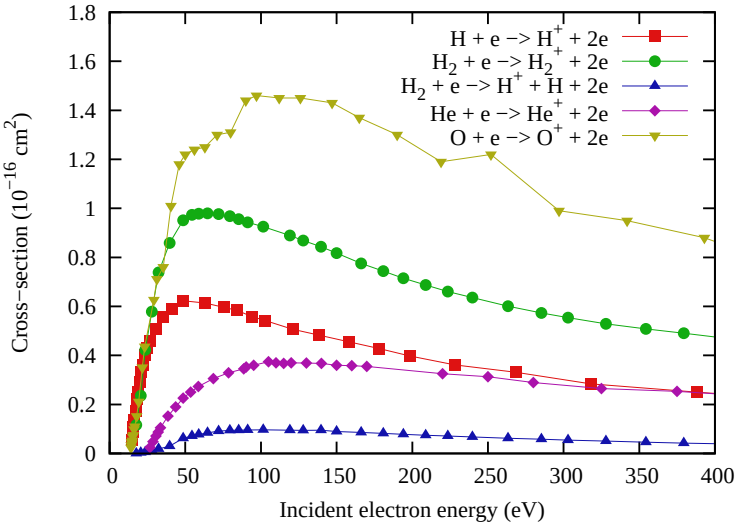

Figure 3.2: Electron impact ionization cross-sections for hydrogen [28, 29], helium [30] and oxygen [31] as a function of incident electron energy.

In hydrogen plasma, the main channel for production of H^+ is through (3.3) regardless of the relatively low cross-section because of the high density of molecular neutral gas. The other channels, such as (3.2) and (3.4) followed by (3.5) do not produce as much protons due to the low densities of H_2^+ and atomic H compared to H_2 density in a typical hydrogen ion source. From the cross-sections it is also obvious that a hydrogen plasma will always contain molecular ions, even though many applications would prefer an ion source producing protons only. On the other hand, some ion sources are optimized for production of H_2^+ for use in cyclotrons with efficient stripping extraction [32, 33].

3.1.2 Multiple ionization

If more than one electron is removed from a neutral atom, the produced ion is said to be *multiply ionized* or *highly charged*. Most commonly in ion source plasmas the ionization process of highly charged ions goes stepwise through several events in which a single electron is removed at each step. The ionization energy needed at each step grows dramatically higher as the charge state increases. For oxygen, for example, the ionization energies for producing ions from O^+ to O^{8+} are 13.6 eV, 35.1 eV, 54.9 eV, 77.4 eV, 114 eV, 138 eV, 739 eV and 871 eV respectively [34]. In ion sources with high neutral pressure and low electron temperature, the production of singly charged ions strongly dominates because of the electron energy distribution. To produce significant amounts of multiply charged ions the neutral pressure has to be low enough to suppress charge exchange reactions, the ion lifetime in the plasma has to be long enough for

multiple ionizations to happen and the plasma has to contain significant amounts of electrons with energy higher than the ionization energy needed for producing the desired ion charged state. Devices especially optimized for the production of multiply charged ions are the ECR ion source [35] and the electron beam ion source EBIS [36].

3.2 Hot electron generation

The electron collision ionization is the most important process for plasma formation in many ion sources. There are several different methods for producing the energetic electrons required for this process including thermionic emission from heated cathode, cold cathode discharge, facilitation of radio frequency power for electron heating with or without magnetic resonance, etc. [37]

3.2.1 Thermionic emission

Possibly the simplest way of producing energetic electrons is to use a heated cathode at an elevated negative potential with respect to the ion source body. The electrons emitted from the cathode are accelerated in the surrounding plasma sheath. A flux of electrons leaves the material as the thermal energy of the electrons in the tail of the distribution overcomes the binding energy or work function of the material. This process is known as the thermionic emission. The flux of electrons can be characterized by the Richardson-Dushman equation

$$J = A_G T^2 \exp\left(\frac{-W}{kT}\right), \tag{3.8}$$

where A_G is the Richardson's constant, T is temperature and W is the work function of the material. A value for the constant A_G can be derived from theory, but in practice

$$A_G = \lambda_R A_0 \tag{3.9}$$

is used, where λ_R is a material correction factor and $A_0 = 4\pi m_e k^2 e/h^3$ is the theoretical value. In ion source applications most commonly used materials for thermionic emissions are high-melting-point metals such as tantalum, tungsten and thoriated tungsten. Resistively heated filament wires can be made out of these metals. Directly or indirectly heated low-work-function materials such as LaB_6, Cs, IrCe and Ba are also used in some applications. See table 3.1 for material parameters. [38, 39]

For example, a typical arc discharge ion source plasma may be driven with a 1.5 mm diameter tantalum wire with length of 100 mm. Assuming that the wire is at constant

Table 3.1: Richardson's constants and work functions for selected materials [38, 40, 41].

Material	A_G (A cm^{-2} K^{-2})	W (eV)
Tantalum	60	4.25
Tungsten	60	4.55
Barium	60	2.7
Caesium	160	2.14
W+Th(1%)	3	2.63
LaB_6	29	2.70

temperature, a 1 A electron emission is achieved at 2300 K temperature. Maintaining such a temperature requires about 250 W of heating power due to radiative losses.

At the typical temperatures needed for electron emission, the main failure mechanism for metallic filaments is breakage mainly due to material evaporation and possibly because of positive ion sputtering. Other failure modes also exist, such as softening of filament material [42]. The material evaporation rates have an exponential dependence on temperature and therefore lifetimes of ion source filaments are highly varied ranging from hundred hours in high performance systems to tens of thousands of hours in lower beam intensity applications.

In a typical filament-driven ion source the positive (or negative) terminal of the filament is biased to about -100 V with respect to the ion source body. The filament on the other hand is heated with a high DC current corresponding to a potential difference of a few volts across the filament terminals. Therefore the energy distribution of the electrons accelerated into the plasma is a rather sharp peak close to 100 eV. Around this energy the total ionization cross section of H_2 is about $1 \cdot 10^{-16}$ cm^2. At a typical ion source pressure of 0.5 Pa the H_2 molecule density is $1.2 \cdot 10^{20}$ m^{-3}. The mean-free-path for the ionization process is therefore about 80 cm, which is much larger than the typical size of the ion source chamber. This is the reason why good magnetic confinement of electrons is important for igniting and maintaining a plasma discharge at low hydrogen pressure.

3.2.2 Radio frequency heating

The limited lifetime of the filament can be a problem in high performance ion source applications. Plasma heating using radio frequency (RF) electromagnetic field provides an elegant alternative solution [43]. This method works by accelerating cold electrons in the plasma with time-varying electric field. The electric field can be introduced in the plasma by an antenna or an electrode immersed in the plasma or by an external antenna behind a window transparent to the RF. In the case of a high voltage electrode immersed in the plasma, the accelerating electric field is created directly in

the plasma sheath surrounding the electrode. This is known as *capacitively coupled* plasma heating, which is seldom used in ion beam sources, but often in plasma processing devices for example. In ion sources a high current RF antenna is often used, which creates a varying magnetic field around the antenna, which induces an electric field accelerating the electrons. This is known as *inductively coupled* plasma.

Starting the discharge in RF ion sources is based on the few free electrons in the neutral gas filling the ion source chamber. When the RF is switched on these electrons are accelerated and cause first ionization reactions and more electrons become available for the discharge. Maintaining the RF heated plasma is much easier than igniting it and therefore high pressure pulsing or other ignition procedures are often needed in these sources [44].

The typical inductively coupled RF heated ion source operates between 1 MHz and 100 MHz and uses either an *internal antenna* [45] or an *external antenna* [46] to feed the RF power to the plasma. The internal antenna ion sources often have a solenoidal antenna with an insulating coating immersed in the plasma. The external antennas, which are separated from the plasma by an RF window, usually have a geometry of a flat spiral or a solenoid. The maintenance-free lifetime of these ion sources is very high and is mainly limited by coating of the RF window with metal in case of external antenna or puncturing through the antenna coating in case of internal antenna [45].

The induced electric field penetrating from the antenna to the plasma decays as

$$E = E_0 \exp\left(\frac{-x}{\delta_p}\right) \tag{3.10}$$

as a function of distance x from the antenna due to the shielding effect of plasma. The distance of penetration is known as *skin depth* and can be calculated as

$$\delta_p \approx \frac{c}{\omega_{pe}} = \sqrt{\frac{m_e}{e^2 \mu_0 n_e}} \tag{3.11}$$

assuming low collision frequency compared to frequency of RF field. The coupling of the solenoidal RF antenna to the cylindrical plasma skin can be modelled as a simple transformer with N turn primary and one turn secondary as shown in figure 3.3. [47]

The resistance of the plasma loop resulting from electron collisional processes can be calculated from

$$R_p = \frac{2\pi r}{\sigma l \delta_p}. \tag{3.12}$$

Here

$$\sigma = \frac{e^2 n_e}{m_e \nu_e} \tag{3.13}$$

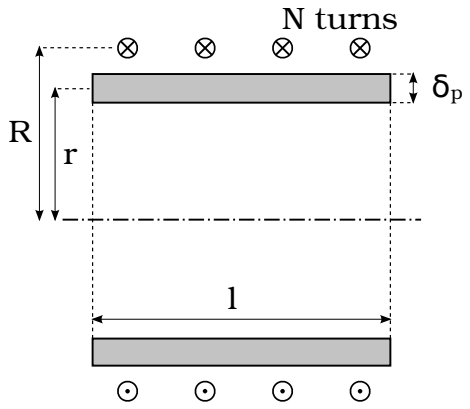

Figure 3.3: Transformer formed by the N turn solenoidal RF antenna at radius R and the cylindrical plasma skin at radius r.

is the plasma conductivity, where ν_e is the total collision frequency of electrons. The inductance L_p of the plasma loop can be calculated from

$$L_p = \frac{\Phi_B}{I} = \frac{\mu_0 \pi r^2}{l}. \tag{3.14}$$

Similarly the inductance L_{ant} of the solenoidal RF antenna and the mutual inductance L_m linking the coils can be calculated from

$$L_{\text{ant}} = \frac{\mu_0 \pi R^2 N^2}{l} \tag{3.15}$$

$$L_m = \frac{\mu_0 \pi r^2 N}{l}. \tag{3.16}$$

The resulting RF antenna circuit model is shown in figure 3.4a. By solving the circuit equations

$$V_{\text{rf}} = j\omega_{rf} L_{\text{ant}} I_{\text{rf}} + j\omega_{rf} L_m I_p \tag{3.17}$$

$$V_p = j\omega_{rf} L_m I_{\text{rf}} + j\omega_{rf} L_p I_p \tag{3.18}$$

$$V_p = -I_p R_p \tag{3.19}$$

and assuming $\omega_{rf} L_p \gg R_p$ a simplified model shown in figure 3.4b can be constructed, where

$$R_{\text{eq}} = N^2 \frac{2\pi r}{\sigma l \delta_p} \tag{3.20}$$

$$L_{\text{eq}} = \frac{\mu_0 \pi R^2 N^2}{l} \left(1 - \frac{r^2}{R^2}\right). \tag{3.21}$$

For example, a typical antenna geometry for a 13.56 MHz RF frequency system is $N = 5$, $l = 50$ mm, $R = 50$ mm and $r = 45$ mm. Assuming a typical plasma density

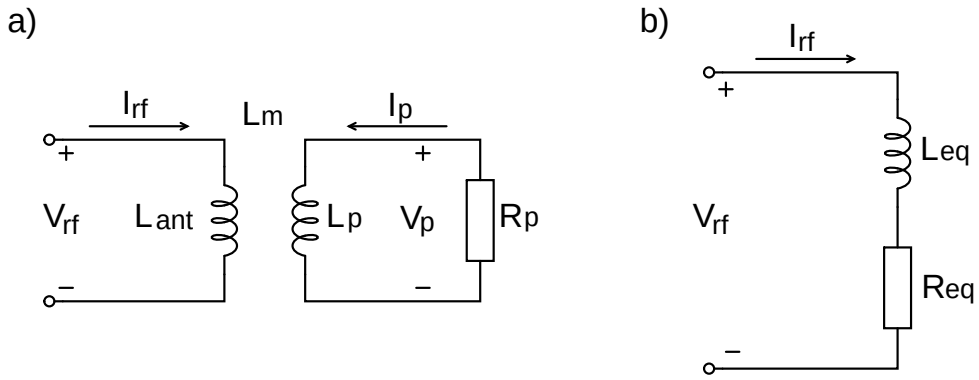

Figure 3.4: RF antenna circuit models: a) Transformer system with primary antenna coil and secondary plasma coil with resistance. b) Simplified equivalent impedance circuit.

of 10^{18} m^{-3} and electron collision rate of 10 MHz the R_{eq} becomes 11 Ω and L_{eq} becomes 0.94 μH ($\omega_{rf} L_{\mathrm{eq}} = 80$ Ω). It is obvious that an RF power supply designed to operate with a resistive 50 Ω load is not capable of directly delivering high power to the complex impedance of the antenna. Therefore, an impedance matching network is needed to adapt the load to the driver. In figure 3.5, three different type of networks for impedance matching are presented.

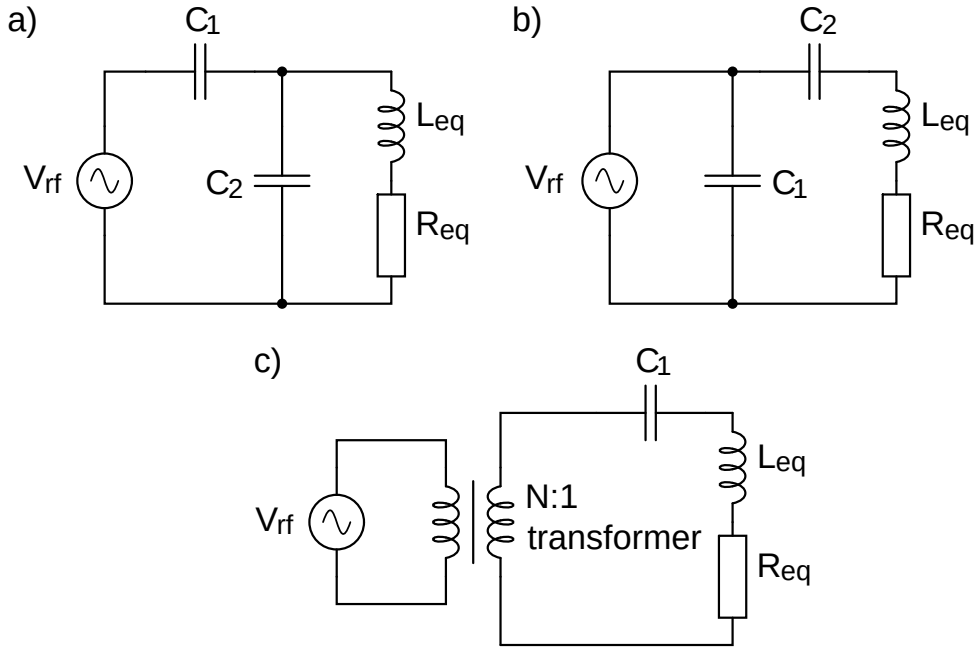

Figure 3.5: Circuit diagrams presenting three different RF matching networks: a) the T network, b) the L network and c) inductively coupled network. The capacitors are typically adjustable.

Figures 3.5a and 3.5b present T and L matching networks respectively, which are both based on two adjustable capacitors. The T network has been the traditional choice in RF ion source systems, but the tuning range at low R_{eq} is limited by low C_1 value, which approaches the value of typical stray capacitances. The L network is a better solution at these conditions with higher, more practical capacitance values. Figure 3.5c presents a third possible matching circuit known as the inductively coupled network. It is based on an adjustable N-to-one ferrite transformer driving a secondary circuit, which includes the antenna and an adjustable capacitor. The transformer circuit is easier to operate than capacitive networks but suffers from inefficiency due to transformer core losses especially at high power levels. [48]

3.2.3 Electron cyclotron resonance heating

Similarly to the radio frequency ion sources, the *electron cyclotron resonance* or ECR ion sources are based on heating electrons in the plasma with radio frequency power. The difference to RF ion sources is that in the ECR ion sources the plasma particles are confined by strong magnetic field and there is no field free region. The electrons are forced to helical trajectories around the field lines and they can not be accelerated to high energies by an electric field perpendicular to the magnetic field. An efficient means of electron heating in the magnetized plasma is by electron cyclotron resonance, where the heating electric field frequency equals electron cycle frequency in the magnetic field as given by eq. (2.32). In ECR ion sources it has been observed that the achievable plasma density $n_e \propto \omega_{rf}$. Therefore, there is a drive towards higher frequencies in the devices. The current state-of-the-art is at 28 GHz, meaning that the resonance magnetic field is about one and peak fields are several Teslas. [35, 49]

3.3 Negative ion sources

Most of the elements and some molecules are capable of forming bound states as negative ions. The *electron affinity* of an element is the amount of energy needed to separate an electron from the negative ion and is therefore a measure of the stability of the ion e.g. in a plasma environment. A negative electron affinity means that the element does not form a stable bound state as a negative ion. Such elements include beryllium, nitrogen, magnesium and all noble gases. The electron affinities range from the negative numbers up to 3.62 eV of chlorine. The electron affinity of hydrogen is 0.75 eV. The electron affinities of most elements are presented in figure 3.6.

Negative ions can be formed by numerous different processes including double charge exchange of positive ions, surface conversion and so-called direct volume production. The double charge exchange process is usually used to convert a positive ion beam

1 **H** 0.7542																	2 **He** <0
3 **Li** 0.6180	4 **Be** <0											5 **B** 0.2797	6 **C** 1.2621	7 **N** <0	8 **O** 1.4611	9 **F** 3.4012	10 **Ne** <0
11 **Na** 0.5479	12 **Mg** <0											13 **Al** 0.4328	14 **Si** 1.3895	15 **P** 0.7465	16 **S** 2.0771	17 **Cl** 3.6127	18 **Ar** <0
19 **K** 0.5015	20 **Ca** 0.0246	21 **Sc** 0.189	22 **Ti** 0.084	23 **V** 0.525	24 **Cr** 0.6758	25 **Mn** <0	26 **Fe** 0.151	27 **Co** 0.6633	28 **Ni** 1.1572	29 **Cu** 1.2359	30 **Zn** <0	31 **Ga** 0.41	32 **Ge** 1.2327	33 **As** 0.814	34 **Se** 2.0207	35 **Br** 3.3636	36 **Kr** <0
37 **Rb** 0.4859	38 **Sr** 0.11	39 **Y** 0.307	40 **Zr** 0.426	41 **Nb** 0.893	42 **Mo** 0.7472	43 **Tc** 0.55	44 **Ru** 1.046	45 **Rh** 1.1429	46 **Pd** 0.5621	47 **Ag** 1.3045	48 **Cd** <0	49 **In** 0.404	50 **Sn** 1.1121	51 **Sb** 1.0474	52 **Te** 1.9709	53 **I** 3.0590	54 **Xe** <0
55 **Cs** 0.4716	56 **Ba** 0.1446	57-71 Lantha- noids	72 **Hf** <0.1	73 **Ta** 0.322	74 **W** 0.815	75 **Re** 0.15	76 **Os** 1.0778	77 **Ir** 1.5644	78 **Pt** 2.1251	79 **Au** 2.3086	80 **Hg** <0	81 **Tl** 0.377	82 **Pb** 0.364	83 **Bi** 0.9424	84 **Po** 1.9	85 **At** 2.8	86 **Rn** <0
87 **Fr**	88 **Ra** 0.17	89-103 Acti- noids	104 **Rf**	105 **Db**	106 **Sg**	107 **Bh**	108 **Hs**	109 **Mt**	110 **Ds**	111 **Rg**	112 **Cn**						

Lanthanoids	57 **La** 0.47	58 **Ce** 0.5	59 **Pr** 0.0	60 **Nd** <0	61 **Pm** <0	62 **Sm** 0.3	63 **Eu** <0	64 **Gd** 0.5	65 **Tb** 0.5	66 **Dy** <0	67 **Ho** <0	68 **Er** <0	69 **Tm** 0.3	70 **Yb** <0	71 **Lu** 0.5
Actinoids	89 **Ac**	90 **Th** 0.5	91 **Pa** 0.3	92 **U** 0.3	93 **Np**	94 **Pu**	95 **Am**	96 **Cm**	97 **Bk**	98 **Cf**	99 **Es**	100 **Fm**	101 **Md**	102 **No**	103 **Lr**

Figure 3.6: Electron affinities in electron volts for most elements presented in a form of the periodic table. Data from references [50, 51, 52].

into negative beam by passing it through a vapor of neutrals with low ionization energy. The negative ions are formed either by single step process using alkaline earth vapors such as magnesium, calcium, strontium or barium or by a two step process using alkali metal vapors such as sodium, potassium, rubidium or caesium. The one step process is more efficient for charge exchange of high electron affinity elements such as chlorine [53]

$$\mathrm{Cl}^+ + \mathrm{Mg} \rightarrow \mathrm{Cl}^- + \mathrm{Mg}^{2+}. \tag{3.22}$$

On the other hand, the two step process is more efficient for lower electron affinity elements. Using alkali metal vapors it is also possible to make negative ion beams out of negative electron affinity elements, which do not form bound states. Negative helium, which has a lifetime of 18 μs can be produced from low-energy He^+ beam using e.g. caesium vapor with charge exchange process [54, 55]

$$\mathrm{He}^+ + \mathrm{Cs} \rightarrow \mathrm{He}^0 + \mathrm{Cs}^+ \tag{3.23}$$

$$\mathrm{He}^0 + \mathrm{Cs} \rightarrow \mathrm{He}^- + \mathrm{Cs}^+. \tag{3.24}$$

3.3.1 Volume production

The volume production is a process, where the formation of negative ions happens in the plasma volume at thermal energies. In case of hydrogen the dominant process leading to production of H^- is generally believed to be the dissociative attachment reaction of ro-vibrationally excited hydrogen molecules [56]. The production of the

required ro-vibrational molecules happens via several processes on the walls and in the plasma volume. One of the most important processes is recombinative desorption of hydrogen atoms from surfaces [57, 58]. Depending on the exact reaction kinetics, the reaction is able to populate different vibrational and rotational levels. Especially in case of gas-phase hydrogen atoms interacting with the surface, it is possible to populate ro-vibrational levels with $\nu > 4$ [59]:

$$\mathrm{H_{gas}} + \mathrm{H_{surface}} \rightarrow \mathrm{H_2}(\nu, J). \tag{3.25}$$

Another important channel for production of vibrational molecules is via high energy ($E > 20$ eV) electron collisions on molecules leading to electronic excitation of the molecule to electronic $B^1\epsilon_u^+$, $C^1\Pi_u$, $B'\Sigma_u^+$ and $D^1\Pi_u$ states, which decay to vibrational states or generate atomic fragments via dissociation. The cross-sections for the total process

$$\mathrm{H_2}(\nu = 0) + \mathrm{e_{fast}} \rightarrow \mathrm{H_2}(B^1\epsilon_u^+, C^1\Pi_u, B'\Sigma_u^+, D^1\Pi_u, \nu) + \mathrm{e} \tag{3.26}$$

$$\rightarrow \mathrm{H_2}(\nu) + \mathrm{e} \tag{3.27}$$

leading to the final vibrational states that are on electronic ground state have been evaluated [60] and are shown in figure 3.7 as a function of incident electron energy.

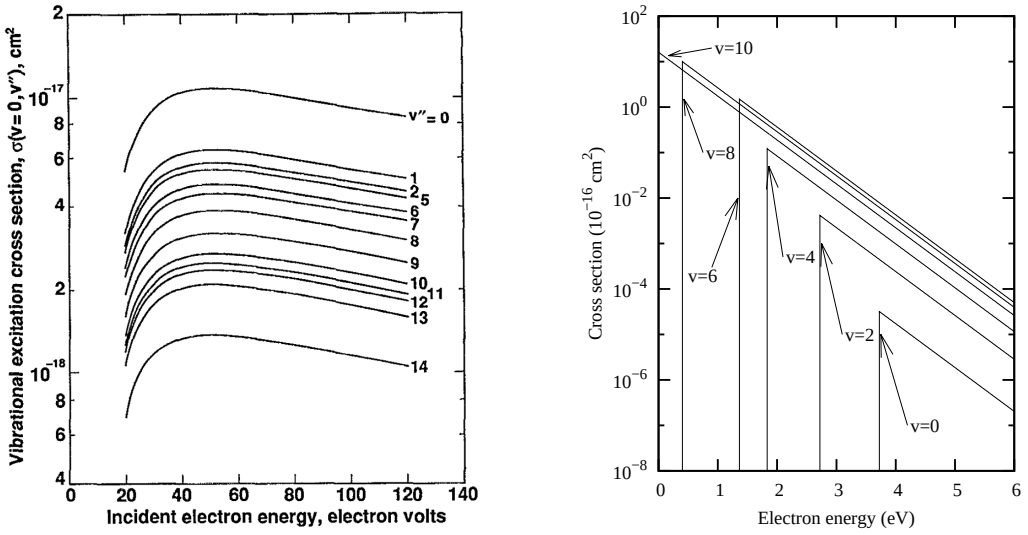

Figure 3.7: Cross sections for volume production of H^-. Cross section for production of vibrationally excited electronic ground state hydrogen molecules via electron collision on the left [60] and dependence of the dissociative attachment reaction cross section on the vibrational state of the hydrogen molecule on the right [61].

The dissociative attachment reaction

$$\mathrm{H_2}(\nu, J) + \mathrm{e_{slow}} \rightarrow \mathrm{H_2^-} \rightarrow \mathrm{H^-} + \mathrm{H} \tag{3.28}$$

producing the H^- is most probable at low incident electron energies and high molecular vibrational states. The cross section decreases exponentially as a function of the electron energy above the threshold energy as is shown in figure 3.7. Also the destruction of H^- by collisional detachment by electrons increases with electron energy. For significant production of H^- to take place, the plasma temperature needs to be lower than what is generally required for efficient generation of plasma and ro-vibrational molecules. The ion sources for volume production of H^- are therefore typically separated into two regions as shown in figure 3.8: The first region contains the plasma driver, a thermionic filament for example, and thus contains a hot electron population. The second region is separated from the first by a transverse magnetic filter field, which lets low energy electrons pass through by diffusion with heavier positive ions and neutrals. Fast electrons are mostly reflected back to the first region. In the second region the production rate of negative ions by the ro-vibrational molecules originating from the first region and from the plasma chamber surfaces of the second region outweighs the destruction rate. Therefore, the H^- ions form a significant fraction of the plasma of this region, from which the negative ion beam is then extracted along with the co-extracted electron beam.

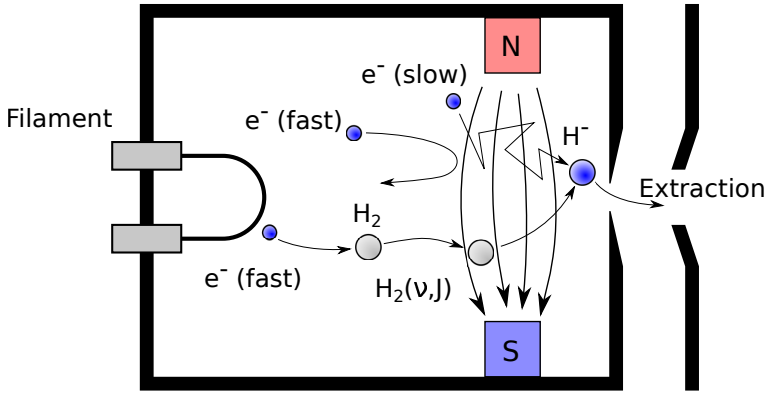

Figure 3.8: Schematic presentation of the most important processes leading to negative hydrogen ions in a volume production ion source: Excited hydrogen molecules and slow electrons are able to pass the magnetic filter field to the region near the extraction aperture, where dissociative attachment reaction produces H^-.

The dissociative attachment reaction is generally considered to be the most dominant process for negative ion production. However, there are other processes, which may be of similar importance. For example, the dissociative attachment on molecular Rydberg states

$$H_2^* + e \rightarrow H^- + H \tag{3.29}$$

has been suggested as one [62, 59].

3.3.2 Surface production

The surface production of negative ions relies on bombardment of a surface with positive ions or atoms. As the incoming atom moves close to the surface its electron affinity level shifts and broadens. If the electron affinity level is then below the Fermi level of the surface material, electrons have a finite probability of tunneling to the atom, forming a negative ion [63]. Such negative ions can be ejected from the surface via two processes. The incoming positive ion may be directly reflected away from the surface after experiencing double charge exchange [64] and negative ions can be ejected by the conversion of atoms sputtered from the surface by the incoming positive ions. Ion sources based on caesium sputtering are widely used in a range of applications routinely producing beams from solid sputtering targets [65]. In production of negative hydrogen ions in plasma sources, it is believed that the dominating process is the sputtering of hydrogen atoms adsorbed to the surface [64, 66, 67].

The formation of negative ions from particles ejected from a metal surface is described with two models: a *probability model* and an *amplitude model* [63, 68]. According to the probability model the negative ion formation probability is

$$p \propto \frac{v_\perp}{\phi - E_a - \Delta E_a}, \tag{3.30}$$

where $v_\perp$ is the velocity of the ejected ion normal to the surface, ϕ is the surface work function, E_a is the electron affinity of the negative ion and ΔE_a is the shift of the affinity level near the surface. According to the amplitude model the negative ion formation probability is

$$p \propto \exp\left(\frac{E_a - \phi}{v_\perp}\right). \tag{3.31}$$

The amplitude model has been found to be more accurate for low velocities, while the probability model is better for high velocities ($E > 20$ eV). Both models predict that increasing ion velocity and decreasing surface work function enhance the negative ion yield. For this reason, caesiation of metal surfaces is typically used to dramatically decrease the surface work function. The addition of caesium to the plasma discharge plays a double role as it also increases the sputtering effect in these sources because it is a heavy element. The conversion surface is often biased with respect to the plasma in the ion sources relying on surface production. This bias increases the energy and flux of positive ions to the surface, leading to higher sputtering yield and increasing the ejected particle velocity. Both of these effects increase the negative ion production. On the other hand, the increased surface bombardment may decrease the caesium coverage away from the optimal. The surface production is used mainly in pulsed ion sources where caesium coverage can be recovered between the pulses. [69]

The use of caesium has an important role in the negative ion production but it does have problems such as difficulty of operation (maintaining constant caesium coverage),

accumulation of caesium in the system (i.e. the extraction, causing high voltage holding problems) and safety hazards (caesium is highly reactive). Generally caesium-free ion sources are more reliable but are not capable of producing as high beam intensities as caesiated sources, but alternatives for high intensity negative ion production have been studied [70]. As an example of new ideas, the use of negative electron affinity materials such as hydrogen-terminated boron nitride and diamond has been proposed to be used in caesium-free surface production ion sources [71].

3.3.3 Negative ion destruction processes

The negative ion destruction processes are an important part of the physics affecting the efficiency of production of negative beams. For H^- important destructive processes include (1) mutual neutralization reactions with the positive ion species

$$H^- + H^+ \rightarrow H_2^+ + e \tag{3.32}$$
$$H^- + H^+ \rightarrow H + H(n) \tag{3.33}$$
$$H^- + H_2^+ \rightarrow H + H_2 \tag{3.34}$$
$$H^- + H_3^+ \rightarrow 2H + H_2, \tag{3.35}$$

(2) associative and non-associative electron detachment reactions

$$H^- + H \rightarrow H_2 + e \tag{3.36}$$
$$H^- + H \rightarrow H + H + e, \tag{3.37}$$

and (3) detachment in collisions with fast electrons

$$H^- + e \rightarrow H + 2e. \tag{3.38}$$

By calculating the H^- mean free path from the cross-sections (from references [72, 73]) using reasonable estimates for the particle densities and temperatures near the extraction aperture the reaction rates can be evaluated. The evaluation has been done for the JYFL LIISA filament driven negative ion source ($n_{H_2} = 10^{20}$ m^{-3}, $n_H = 10^{19}$ m^{-3}, $n_{H^-} = 2 \cdot 10^{17}$ m^{-3}, $n_e = 2 \cdot 10^{16}$ m^{-3}, $n_H = 10^{19}$ m^{-3}, $n_{H^+} = 2.2 \cdot 10^{17}$ m^{-3}, $T_H \sim 0.03$ eV, $T_{H^-} = T_{H^+} = 0.1$ eV, $T_e = 1.0$ eV [74, 75]). The mutual neutralization (3.33) and associative electron detachment (3.36) are the most important destruction processes. The reaction rate of the fast electron induced detachment process (3.38) is negligible in these conditions, but it is highly sensitive to electron temperature, which is one of the reasons why volume production is greatly enhanced by the magnetic filter. According to the calculation, the total mean free path of H^- in these conditions becomes 14 cm. Due to the magnetic filter field and high elastic collision frequency compared to the destructive collisions, the negative ion transport is highly diffusive. This means that most of the negative ions are only capable of propagating about a few centimeters from their birth locations. [76]

The negative ion may also be destroyed in collisions with neutral gas molecules [72]

$$H^- + H_2 \rightarrow H + H_2 + e. \tag{3.39}$$

This process becomes probable at energies higher than 2–3 eV. In the typical ion source pressure range, the mean free path for this process is about 10 cm. In surface conversion H^- sources such as Los Alamos Neutron Science Center (LANSCE) ion source [77], the losses through this process may be significant, as the negative ion beam is transported from the converter surface to the extraction aperture through the ion source. In volume production ion sources H^- collisions with the background gas cause beam losses or *stripping* in the extraction, especially in the first acceleration gap, where the gas pressure is typically much higher than in the rest of the extraction system.

3.3.4 Overview of H^- ion sources for accelerators

Currently there are several H^- ion sources of different types in operational use at accelerator laboratories world wide. Also several ion sources are being run at test stands for development purposes. It is impossible to cover all varieties of devices here. Instead, a brief overview of selected ion sources is given. More thorough reviews of operational H^- ion sources are available for example in references [78, 79, 80].

At TRIUMF in Vancouver, Canada, a tantalum filament driven multicusp ion source is used to produce up to 15 mA of continuous H^- beam at 28 keV for acceleration in cyclotrons. The source is driven with up to 5 kW of arc power. The source is based on volume production and it has a unique permanent magnet configuration for multicusp confinement and electron filter field [81]. The JYFL LIISA ion source, described later in this thesis, is a version of the TRIUMF source regularly producing 1 mA of H^- at 5.9 keV [74].

At the Spallation Neutron Source (SNS) in Oak Ridge National Laboratory, USA, a multicusp ion source is used to produce 0.9 ms long 50 mA H^- pulses at 60 Hz repetition rate. The source is driven by a continuous low power 13.56 MHz RF to maintain the plasma and a 50–70 kW 2 MHz RF during the pulses. The RF power is coupled to the plasma by an internal porcelain coated antenna. The source is equipped with a caesiated, temperature controlled molybdenum collar near the extraction to enhance production of H^-. It is estimated that caesium enhanced surface processes contribute to production of about 70 % of the extracted beam. An external antenna version of this ion source is under development. [82, 83]

At Deutsches Elektronen-Synchrotron (DESY) facility the Hadron Elektron Ring Anlage (HERA) accelerator was driven by a cesium-free volume-production multicusp ion source producing 36 keV 40 mA 150 μs H^- pulses with 8 Hz repetition rate. The

source was driven by a 30 kW RF power coupled to the plasma by a coil antenna external to the Al_2O_3 source chamber. The source has proven over 150 week long maintenance-free runs. The HERA accelerator is no longer operational, but the ion source design continues to be developed for a new application at CERN. [46, 84]

The Penning H^- ion source is based on an arc discharge plasma in a geometry where electrons are magnetically confined between two cathodes. The H^- surface production takes place on caesiated cathode surfaces, from which the negative ions are accelerated to the plasma by the cathode bias. The extracted negative ions have experienced resonant charge exchange with slow hydrogen atoms ($H^-_{fast} + H_{slow} \rightarrow H_{fast} + H^-_{slow}$) leading to high quality beam. At Rutherford Appleton Laboratory in UK, a Penning-type source is producing 200 μs, 45 mA H^- pulses from a 0.6×10 mm^2 plasma electrode slit with 50 Hz repetition rate into the ISIS spallation neutron source accelerator. [79]

The surface converter H^- ion source at Los Alamos Neutron Science Center (LANSCE) is driven by pulsed 180 V, 30–40 A discharge ignited by electrons emitted from continuously heated tungsten filaments. The H^- production takes place on a molybdenum converter, which is caesiated using an external oven. The converter is biased to 250–300 V negative potential with respect to the ion source body to draw positive ion species towards it. Because of the low surface work function achieved with caesiation the particles sputtered from the converter have a high probability of leaving as H^-. These negative ions are accelerated by the bias voltage towards the extraction aperture. The source has been operated with 120 Hz and 60 Hz repetition rates with ~ 1 ms pulse length. [77, 85]

The main operational parameters of the aforementioned ion sources are gathered in table 3.2.

Table 3.2: The main operational parameters of selected negative hydrogen ion sources.

Source	I_{H^-}	e^-/H^-	Pulse len.	Rep. rate	Duty factor	Maintenance
TRIUMF multicusp	15 mA	< 5	cw	cw	100 %	3 weeks
LIISA multicusp	3 mA	< 5	cw	cw	100 %	2 weeks
SNS RF multicusp	50 mA	~ 10	900 μs	60 Hz	5.4 %	6 weeks
DESY RF multicusp	40 mA	~ 20	150 μs	8 Hz	0.12 %	150 weeks
ISIS Penning	45 mA	~ 10	200 μs	50 Hz	1 %	7 weeks
LANSCE converter	16–18 mA	< 10	835 μs	60/120 Hz	5–10 %	4 weeks

Chapter 4

Ion extraction and low energy beam transport

In principle, the task of the beam extraction and the following low energy beam transport or LEBT system is quite simple. Most often the ion source extraction consists of the front plate of the ion source, which is known as the *plasma electrode* and at least one other electrode, the *puller electrode* (or extractor). The potential difference between the electrodes provides the electric field for accelerating the charged particles from the ion source forming an ion beam. Whether or not the extraction contains any other electrodes, the beam leaves the extraction with kinetic energy

$$E_K = q(\phi_{\text{plasma}} - \phi_{\text{beamline}}) \tag{4.1}$$

defined by the charge q of the particles and the potential difference between the plasma ϕ_{plasma}, where the ions are formed and the following beam line ϕ_{beamline}, which is typically at the laboratory ground potential, as shown in figure 4.1. The ion source voltage is therefore set according to the requirements of the following application. The potential difference between the plasma and the ion source body contributes slightly to the beam energy. The intensity of the particle beam depends, as a first approximation, on the thermal flux of charged particles through the plasma electrode aperture. The extracted beam current can therefore be estimated as

$$I = \frac{1}{4} A q n \langle v \rangle, \tag{4.2}$$

where A is the plasma electrode aperture, q is the charge of the particles, n is the density of charged particles which form the beam and $\langle v \rangle$ is the mean velocity of extracted particles in the ion source plasma. Assuming a Maxwell-Boltzmann distribution for the extracted plasma particles the mean velocity is given by eq. (2.2).

The practical solutions are unfortunately much more complicated in most cases. First of all, in the case of negative ion sources, the extraction system needs to separate the

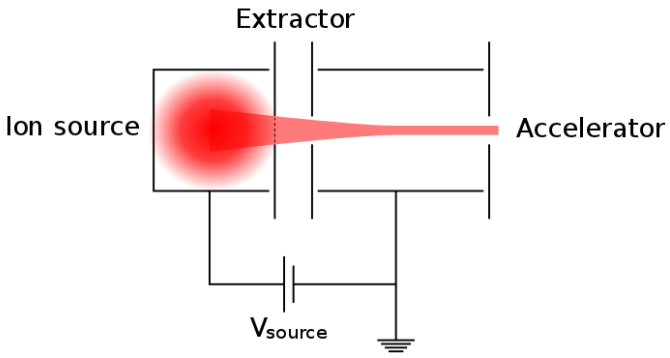

Figure 4.1: A schematic of the electrostatic extraction system.

co-extracted electron beam from the ion beam. The applications following the low energy beam transport, which typically are accelerators to bring the beam to higher energies, often pose strict requirements for the ion beam parameters. Not only the beam intensity, energy and species spectrum need to meet the requirements, but also the beam spatial and temporal structure are specified.

The spatial requirements for the beam raise a need for focusing in the LEBT. Similarly the temporal requirements define the need for beam chopping or bunching. Without careful design of the focusing elements, the initial transverse velocity distribution of the extracted beam and the space charge forces disperse the beam to the walls of the vacuum chamber and only a part of the generated beam is transported to the following accelerator. The extraction focusing systems must also provide some adjustability as in most cases, the plasma conditions might not be constant in day-by-day operations, which is typical especially in the case of caesiated ion sources. The LEBT has to adapt to lower and higher performance, while maximizing the throughput to the following accelerator. Designing such systems is not easy. From the ion optics point of view a system as short as possible would be preferred, but in the same time the system design has to also take in account practical engineering constraints. For example, the beam line needs to have space for diagnostics and vacuum pumps in addition to the focusing elements. Two extreme cases from the opposite ends of the spectrum are the electrostatic extraction of the SNS H^- ion source [86], which is about 15 cm long and the LEBT of the JYFL LIISA H^- ion source, which is almost 15 m long.

This chapter concentrates mainly on the topic of ion optics in the low beam energy systems: the plasma-beam interface, beam quality, space charge effects and focusing elements.

4.1 Beam formation

The charged particles of the extracted ion beam originate from the quasineutral plasma of the ion source. In the case of negative ion source, the electric field between the plasma and puller electrodes accelerates the negative ions and electrons from the plasma, and at the same time prevents the compensating positive particles from penetrating into the extraction. In the case of positive ion source the positive ions are accelerated and the negative, compensating charges are retained in the plasma. In the proximity of the plasma electrode aperture there is a plasma sheath, in which the compensating particle density decays towards the extraction and the beam is formed. Modelling of the sheath is one of the greatest difficulties for computer codes as described later.

4.1.1 Plasma extraction

The potential distribution, which defines the particle trajectories leaving the plasma, is defined not only by the electrode geometry and voltages, but also by the properties of the plasma, i.e. plasma density, plasma potential, electron and ion temperatures. These dependencies are discussed in section 5.2 in more detail, where the plasma sheath model used in the simulations in this work is presented.

The bulk plasma is (almost) free of electric fields. In the sheath region the electric field starts deviating from zero and accelerates the charged particles. It is obvious that there is no well defined boundary between electric field-free quasineutral plasma and the uncompensated extraction region with electric fields. Often, such a boundary would be useful for judging the focusing action of the electric field close to the plasma electrode. Therefore an equipotential surface close to $\phi_{\text{wall}} = 0$ V is often thought as an artificial "boundary" known as the *plasma meniscus*. This terminology is often used even though in reality there is no such sharp boundary. See figure 4.2 for an example of the plasma sheath.

An example of the dependency of the plasma sheath shape on the plasma parameters is presented in figure 4.3, where three simulated cases of H^- extraction are shown with varying plasma densities. All other parameters are unchanged. In case a the plasma density is low and 0.5 mA of H^- is extracted together with 17.5 mA of electrons. The strong electric field in the extraction makes the plasma meniscus concave and the extracted beam is over-focused, causing degradation of beam quality, which most likely results in beam loss in further beam transport (a formal definition of beam quality or emittance is given in section 4.3). In case b the plasma density is higher and 1 mA of H^- beam is extracted together with 35 mA of electrons. The meniscus is slightly concave, which provides the best quality beam in this geometry. A high

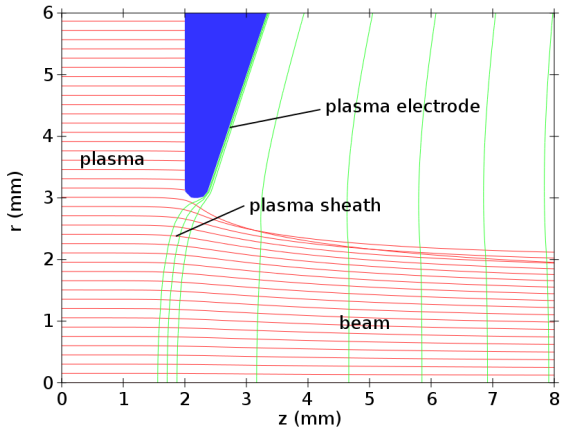

Figure 4.2: Plot from a cylindrically symmetric simulation of H^- extraction with several equipotential lines drawn close to the wall potential to visualize the location of the plasma sheath. The ion temperature in the simulation is set to zero to illustrate how the particles are accelerated perpendicular to the sheath.

fraction of the extracted beam can be transported to be accelerated. In case c the plasma density is even higher and 2 mA of H^- and 70 mA of electrons is extracted. The plasma meniscus is convex, the beam is divergent and the beam quality is again worse than in the optimal case. Lower amount of beam can be transported to the accelerator in this case, even though a more intensive beam is extracted than in case b. Because of this effect, it is important that the electric field strength of the extraction system can be somehow adjusted if varying plasma densities are expected. Possible adjustments are changing the plasma electrode to puller electrode gap or changing the puller electrode voltage.

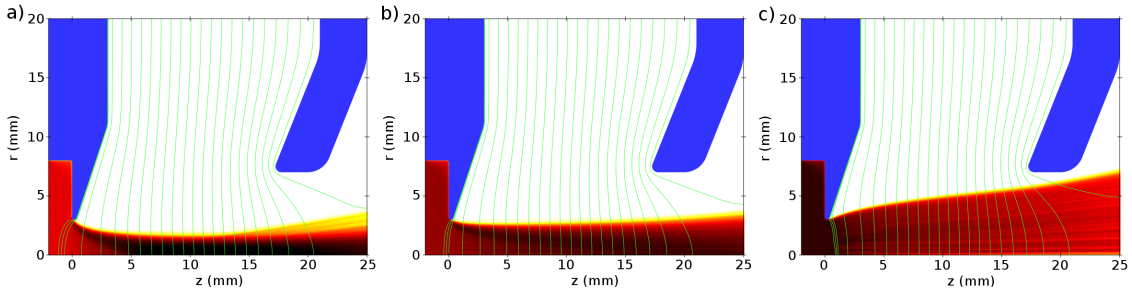

Figure 4.3: Three simulations of 5 keV H^- extraction with varying plasma densities. The extracted beams are a) 0.5 mA, b) 1 mA and c) 2 mA of H^-. The extracted electron to ion ratio in all cases is 35. The highest quality beam is achieved with slightly concave plasma meniscus shape of case b.

4.1.2 Space charge limited emission

In the first acceleration gap, where the beam is formed, the space charge forces acting on the beam are largest. The situation can be evaluated with Poisson equation in one dimension assuming a beam starting with zero velocity. The equation is written as

$$\frac{d^2\phi}{dz^2} = -\frac{\rho}{\epsilon_0} = -\frac{J}{\epsilon_0}\sqrt{\frac{m}{2q\phi}}, \tag{4.3}$$

where z is the location, ϕ is the potential, J is the beam current density, and ϵ_0 is the vacuum permittivity. The emission surface is at $\phi(z = 0) = 0$ and the extractor surface at $\phi(z = d) = V$. For $J = 0$, the potential distribution between the surfaces is linear. As the emission current density increases, the electric field at the emission surface decreases until it becomes zero as is shown in figure 4.4a. At that point the emission current is at the maximum level, which can be solved from (4.3) with the boundary condition $\frac{d\phi}{dz}(z = 0) = 0$. This condition is known as space charge limited emission and the resulting limit for the maximum emission current density can be calculated using the following equation, which is known as the Child-Langmuir law [87]:

$$J_{\max} = \frac{4}{9}\epsilon_0\sqrt{\frac{2q}{m}}\frac{V^{3/2}}{d^2}. \tag{4.4}$$

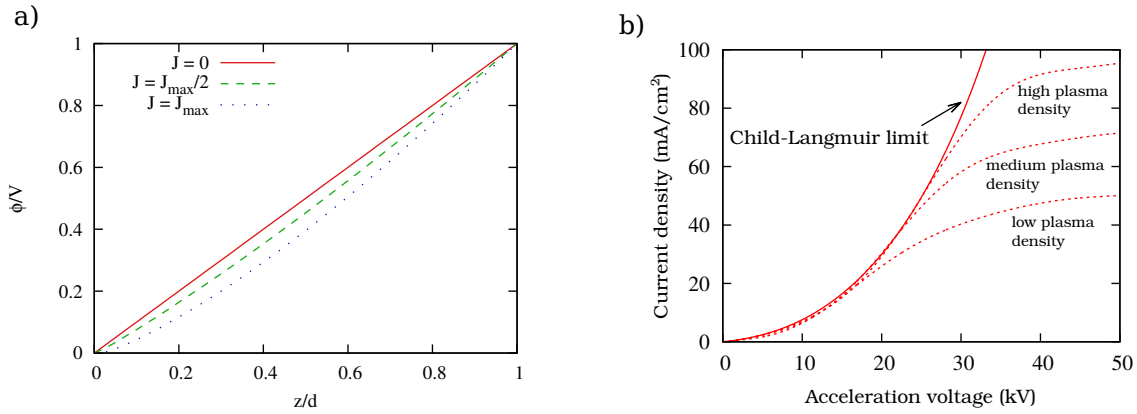

Figure 4.4: a) Potential distribution between emission and extractor surfaces with different beam current densities in the system. b) Typical current-voltage characteristic of plasma extraction. With low acceleration voltages, the emission is operating in the Child-Langmuir limit. At the higher voltages the extracted current density saturates due to emission limit of the plasma.

The plasma ion sources are typically operated in emission limited mode, i.e. the potential difference between the plasma electrode and puller electrode is made sufficiently large to handle the beam space charge. Equation (4.4) is not strictly valid for ion source plasma extraction because of the dynamic nature of the plasma sheath and

non-zero "starting" velocity of particles in plasma extraction. The physics of the space charge limit is still valid and the Child-Langmuir law (4.4) can be used to estimate it.

In any system, the maximum extractable current is dependent on the geometry, the emission current density and voltage via the space charge limit. In the space charge limited region, the current is proportional to $V^{3/2}$. This leads to the definition of beam *perveance*,

$$P = \frac{I}{V^{3/2}}, \tag{4.5}$$

which is the proportionality constant describing the system. As long as the emission is space charge limited, the beam perveance is roughly constant. When voltage is further increased and the beam emission is no longer space charge limited, the beam perveance decreases. See figure 4.4b for an example of the current-voltage characteristic of a plasma extraction.

4.1.3 Electrode geometry

The space charge forces try to disperse the beam as was shown above. This happens especially in the first acceleration gap because of low velocity of the beam. To counteract the space charge forces in the transverse direction, the electrodes can be shaped in such a way that the electric field in the first gap is not only accelerating but also focusing. In the case of space charge limited surface emitted electrons, there is a perfect solution providing parallel electron beam accelerated from the cathode [88]: The solution is to have a field shaping electrode around the cathode (at cathode potential) in a 67.5° angle with respect to the emitting surface normal as shown in figure 4.5. This geometry is known as Pierce geometry. For plasma ion sources, there is no such magic geometry because the ions do not start from a fixed surface, but from plasma with varying starting conditions. The effect of electrode shapes in these systems has been studied using computer simulations modelling the plasma [89].

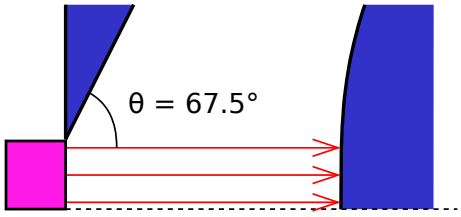

Figure 4.5: Perfectly parallel extraction of space charge limited surface emission electrons using the Pierce geometry in a planar 2D geometry.

4.1.4 Specific features of negative ion extraction systems

In negative ion sources electrons are extracted from the plasma in addition to the ions. Depending on the ion source, the intensity of co-extracted electron beam may be as high as 100–200 times the intensity of extracted negative ion beam or as low as 1 in caesiated surface production H^- sources. Especially in the cases where the electron current is high, the electrons need to be dumped in a controlled manner as soon as possible to mitigate the effects of the additional space charge. Often the electron beam current is so high that dumping cannot be done at the full beam energy required by the application. In other words, the electron beam has to be dumped on an intermediate electrode biased to lower potential than ground. This requirement is often the most significant restriction on negative ion source extraction system designs. Typically the electron dumping is done by utilizing a transverse magnetic field generated with permanent magnets. As the magnetic field also deflects the negative ion beam, the negative ion source may be mounted to the beam transport line at an angle to compensate the deflection [86, 8]. Another solution is to use another transverse magnetic field in opposite direction to correct the angle of the negative ion beam perpendicular to the original axis. The resulting offset in the beam center has to be corrected using deflector plates, xy steering magnets or mechanical offset.

Three electrode configurations shown in figure 4.6 are commonly used for electron dumping. In the first method (a), which is often used in negative ion sources producing continuous beam, the electrons are dumped on a water-cooled puller electrode with low voltage with respect to the ion source [81, 8]. Another solution (b) is the use of an intermediate electron dump electrode before the puller electrode [86]. A third possibility (c) is to dump the electrons on an electrode following the puller electrode. This method allows optimization of the plasma electrode to puller electrode voltage or distance for achieving optimal beam formation without affecting the electron dumping [90, 9].

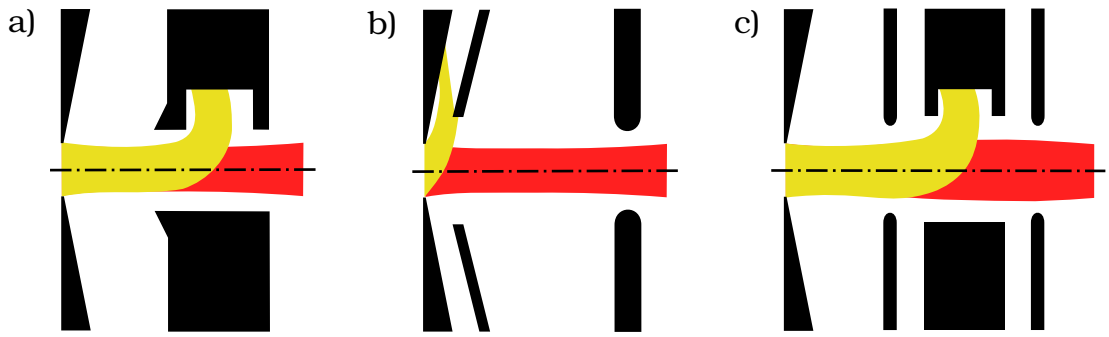

Figure 4.6: Three electrode configurations commonly used for dumping the co-extracted electrons in negative ion sources: a) dumping to puller electrode, b) dumping to intermediate electrode and c) dumping to an electrode after the puller.

4.2 Beam line ion optical elements

The ion optical elements of the beam transport line come in two varieties: magnetic and electric. In the case of high energy beams, where $v \approx c$, magnetic elements are used because the force, which is created with an easily produced magnetic field of 1 T equals the force excerted by an electric field of 300 MV/m, which is impossible to produce in a practical device. In LEBT systems, where the beam velocity is low, and the maximum electric fields are typically about 5 MV/m, the achievable forces are comparable and other factors, such as size, cost, power consumption and the effects to beam space charge compensation come into play. An important factor in the selection of the type of the beam line elements is also the fact that electrostatic fields do not separate ion species. In electrostatic systems the particles follow trajectories defined only by the system voltages. On the other hand, in magnetic fields the particle trajectory is dependent on charge-to-momentum ratio q/p, which allows separation of particle species from each other in magnetic systems. This is utilized in the electron dumping of negative ion extraction systems as was shown in section 4.1.4.

The common beam line elements, which are used to build the extraction and LEBT systems include immersion lens, einzel, solenoid, dipole and quadrupole lenses. A short introduction to each of these elements is given below. More detailed analyses can be found in references [91] and [92], for example.

4.2.1 Immersion lens

The immersion lens (or gap lens) is simply a system of two electrodes with a potential difference of $\Delta V = V_2 - V_1$. The lens can be either accelerating or decelerating and in addition to changing the particle energy by $q\Delta V$ the element also has focusing action. The focal length of the immersion lens is given by [91]

$$\frac{f}{L} = \frac{4(\sqrt{V_2/V_1} + 1)}{V_1/V_2 + V_2/V_1 - 2}, \tag{4.6}$$

where L is the distance between the electrodes and the potentials V_1 and V_2 are defined assuming that $V = 0$ potential is where the beam kinetic energy is zero (ion source plasma). The electrostatic extraction systems always have gap lenses, which accelerate the beam to the required energy. The first acceleration gap (plasma electrode to puller electrode) is a special case of the immersion lens because of the effect of the plasma to the electric field and the focusing effect of it can not be estimated with the equation above.

4.2.2 Einzel lens

The einzel lens is made by combining two gap lenses into one three-electrode system with first and last electrodes in the beam line potential V_0 and the center electrode at a differing potential V_{einzel}. The einzel lens, which is typically cylindrically symmetric, is the main tool for beam focusing in many electrostatic extraction systems. The einzel focusing power is dependent on the geometry and the voltage ratio $R = (V_{\text{einzel}} - V_0)/V_0$, assuming that $V = 0$ potential is where the beam kinetic energy is zero. The einzel lens may have the first gap accelerating and the second gap decelerating (known as accelerating einzel lens, $R > 0$) or vise versa (known as decelerating einzel lens, $R < 0$). Both configurations are focusing, but the refractive power of the einzel in decelerating mode is much higher than in accelerating mode with same lens gap voltage $V_{\text{gap}} = V_{\text{einzel}} - V_0$. As an example, the refractive power of the einzel lens geometry shown in figure 4.7a is calculated as a function of V_{einzel} using numerical methods. The focal length $f \approx 10D$ for a decelerating $V_{\text{einzel}} - V_0 = -0.5V_0$. To achieve the same focal length in accelerating mode a voltage $V_{\text{einzel}} - V_0 = 1.1V_0$ is needed (see figure 4.7b) On the other hand, accelerating einzel lenses should be preferred if the required higher voltage (and electric fields) can be handled, because they have lower spherical aberrations than decelerating einzel lenses, especially when the required refractive power is high. Accelerating einzel lenses also present a potential barrier for the particles compensating the beam space charge in surrounding drift regions making it possible to reach high space charge compensation as discussed in section 4.4.2. Decelerating einzel lenses drain the compensating charges from the beam preventing high space charge compensation degree in the proximity of the lens.

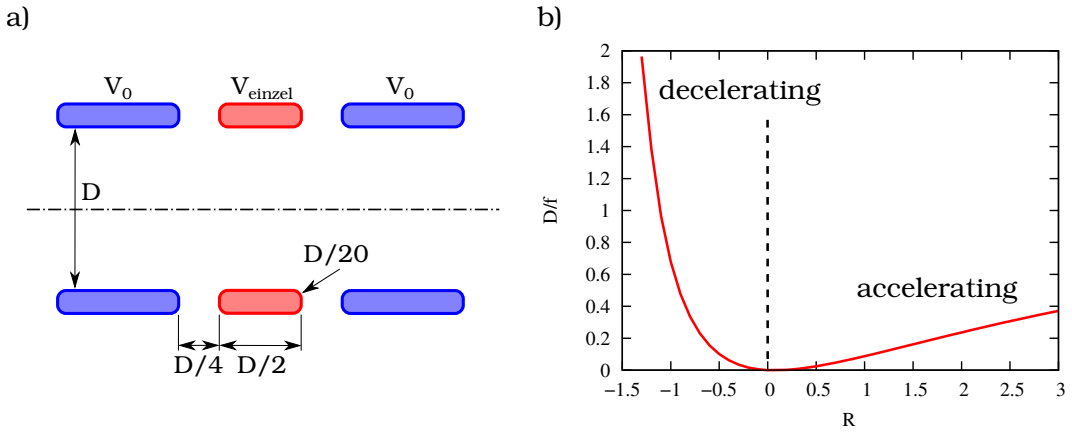

Figure 4.7: An example geometry for an einzel lens and its refractive power scaled with the einzel internal diameter D as a function of the voltage ratio R. The lens is much stronger in decelerating mode compared to accelerating mode. The shown refractive power is valid for particles close to the optical axis in the low-space-charge limit.

A special case of the einzel lens, where the first electrode and the third electrode are at different potentials is also possible, This kind of setup is known as three aperture immersion lens or zoom-lens. It provides adjustable focusing in a system which otherwise acts as an immersion lens. [91]

4.2.3 Solenoid lens

Solenoid lens is a magnetic element providing axisymmetric focusing force. It consists of rotationally symmetric coils wound around the beam tube, creating a longitudinal magnetic field peaking at the center of the solenoid. The focusing action of solenoid is somewhat difficult to derive, but the idea can be described as follows assuming a thin lens [93]: The radial magnetic field at the entrance of the solenoid gives the particle entering the field with $v_r = 0$ at radius r_0 an azimuthal thrust

$$v_\theta = \frac{qBr_0}{2m}, \tag{4.7}$$

which makes the trajectories helical inside the solenoid. At the exit of the solenoid the particle receives a thrust cancelling the azimuthal velocity, but leaving the particle with a radial velocity

$$v_r = -\frac{r_0 q^2}{4m^2 v_z} \int B^2 dz. \tag{4.8}$$

This radial velocity causes the beam to converge towards the optical axis. The refractive power of the lens is given by

$$\frac{1}{f} = \frac{q^2}{8mE_K} \int B^2 dz. \tag{4.9}$$

4.2.4 Electrostatic and magnetic dipoles

The electrostatic dipole and magnetic dipole are elements, which are primarily used to deflect charged particle beams. The magnetic dipole is constructed from coil windings creating a constant magnetic field pointing in the transverse direction. The particles in the magnetic field follow circular trajectories with radius

$$\rho = \frac{p}{qB} \approx \frac{mv_z}{qB} = \frac{1}{B}\sqrt{\frac{2mV_0}{q}}, \tag{4.10}$$

where V_0 is the voltage used to accelerate the particles from zero to v_z. Similarly an electrostatic dipole may be constructed from cylindrical electrodes of radii r_1 and r_2

with voltages V_1 and V_2. The radius of curvature of the particle between the plates becomes

$$\rho = \frac{2\phi}{E}, \tag{4.11}$$

where E is the electric field and ϕ is the potential at the orbit (again assuming that zero potential is where the beam kinetic energy is zero). The voltage and electric field between the plates are

$$V = V_1 + (V_2 - V_1)\frac{\log(r/r_1)}{\log(r_2/r_1)} \quad \text{and} \tag{4.12}$$

$$E = -\frac{V_2 - V_1}{\log(r_2/r_1)}\frac{1}{r}. \tag{4.13}$$

By choosing the plate voltages symmetrically as $V_1 = V_0 + V_{\text{plate}}$ and $V_2 = V_0 - V_{\text{plate}}$, the required plate voltage can be solved as

$$V_{\text{plate}} = V_0 \log(r_2/r_1). \tag{4.14}$$

The optical axis of such a system, where $\phi = V_0$, is at radius $\rho = \sqrt{r_1 r_2}$. This is not the only possibility for the cylindrical dipole. The optical axis can also be chosen to be in the middle of the plates, which leads to asymmetric plate voltages.

The dipole elements also have focusing/defocusing properties. For example, the magnetic dipole with straight edge angles ($\alpha = \beta = 0$) focuses the beam in the bending plane (x) as shown in figure 4.8a. Directly from geometry, a so-called Barber's rule can be derived: the center of curvature of the optical axis and the two focal points are on a straight line. For a symmetric setup it means that $A = B = R/\tan(\frac{\phi}{2})$. There is no focusing action in the y direction.

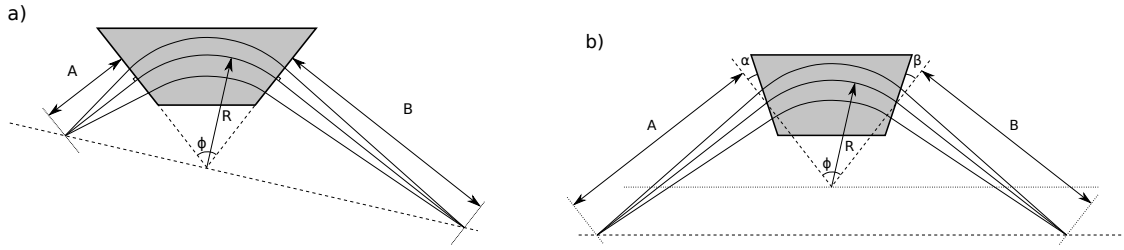

Figure 4.8: Focusing of a magnetic dipole in the bending plane. a) The case where the magnet has straight edge angles ($\alpha = \beta = 0$) is described by Barber's rule: the center of curvature of the optical axis and the two focal points are on a straight line. b) If the edge angles are positive as shown, the focusing power is decreased.

If the magnet edge angles deviate from 90°, the focusing power in x-direction can be adjusted. If the edge angle is made positive (as shown in figure 4.8b), there is weaker focusing in x-direction. If the angle is negative, there is stronger focusing in

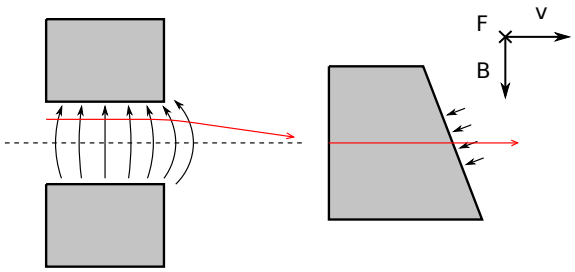

Figure 4.9: In a dipole magnet with positive edge angle the fringing field has a B_x component focusing the beam in y-direction.

x-direction. Changing the edge angle has also an important effect on the y-direction: if the angles are positive the fringing field of the magnet will focus the beam in the y-direction, as shown in figure 4.9. Overall this means that the focusing in x-direction can be traded for y-focusing. The focal length from the edge focusing is given by

$$f_y = \frac{R}{\tan(\alpha)}. \tag{4.15}$$

In a symmetric double focusing dipole, with the is same focal length in x and y, the angles and distances are given by

$$2\tan(\alpha) = 2\tan(\beta) = \tan(\frac{\phi}{2}) \tag{4.16}$$

$$A = B = \frac{2R}{\tan(\frac{\phi}{2})} \tag{4.17}$$

For a $\phi = 90°$ bending magnet the edge angles become $\alpha = \beta = 26.6°$ and the focal distances $A = B = 2R$.

The regular cylindrical electrostatic dipole only has focusing in the x-direction similar to the regular straight edge magnetic dipole. The y-focusing can be introduced by adjusting the ends of the cylindrical plates for edge focusing or by using spherical or toroidal plates.

For small-angle deflection typically electrostatic parallel plates or so-called xy steering magnets are used. The parallel plates with $\pm V_{\text{plate}}$ voltages bend the beam to angle

$$\theta = \frac{V_{\text{plate}} L}{V_0 d}, \tag{4.18}$$

where L is the length of the plates in z-direction and d is the distance between the plates. This kind of system is typically used for small corrections in beam lines and for beam chopping. The xy magnets are the magnetic equivalent of the parallel plates with typically two pairs of windings in a single instrument for correction in both

transverse directions. The beam deflection is given by

$$\theta = LB\sqrt{\frac{q}{2mV_0}}, \tag{4.19}$$

where L is the field length and B is the field strength inside the device.

4.2.5 Quadrupole lenses

Electrostatic and magnetic quadrupoles are often used as focusing elements in LEBT systems in addition to einzel lenses and solenoids. The electrostatic quadrupole consists of four hyperbolic electrodes placed symmetrically around the beam axis with positive potential V_{quad} on the electrodes in $+x$ and $-x$-directions and negative potential $-V_{\text{quad}}$ on the electrodes in $+y$ and $-y$-directions as shown in figure 4.10a. The potential in such configuration is given by

$$V = \frac{x^2 - y^2}{a^2} V_{\text{quad}}, \tag{4.20}$$

where a is the half-aperture of the quadrupole. This leads to electrostatic field

$$\vec{E} = -\frac{2V_{\text{quad}}}{a^2} x\hat{x} + \frac{2V_{\text{quad}}}{a^2} y\hat{y}, \tag{4.21}$$

from which we can see that such quadrupole focuses a positive ion beam in x-direction and defocuses in the y-direction. By analyzing the particle trajectories in such fields, it can be shown that the refractive powers for the thick lens are

$$1/f_x = k\sin(kL) \tag{4.22}$$

$$1/f_y = -k\sinh(kL), \tag{4.23}$$

where $k^2 = \frac{V_{\text{quad}}}{a^2 V_0}$ and L is the effective length of the quadrupole [92].

The magnetic quadrupole has a similar construction to the electrostatic one: the magnet poles are made to be hyperbolic and coils are wound in such a way that opposite poles have magnetic flux towards the beam and the other two poles have flux outwards. Assuming that the magnetic poles are oriented as shown in figure 4.10b, the magnetic field in such system is

$$\vec{B} = \frac{B_T}{a} y\hat{x} + \frac{B_T}{a} x\hat{y}, \tag{4.24}$$

where B_T is the magnetic field density at the pole tip. Positively charged particles having velocity $\vec{v} = v_z\hat{z}$ feel a force $\vec{F} = qB_T v(-x\hat{x} + y\hat{y})/a$, which is focusing in x-direction and defocusing in y-direction. The magnetic force leads to the same refractive powers as presented by (4.22) and (4.23), but with $k_B^2 = \frac{q}{p}\frac{B_T}{a}$.

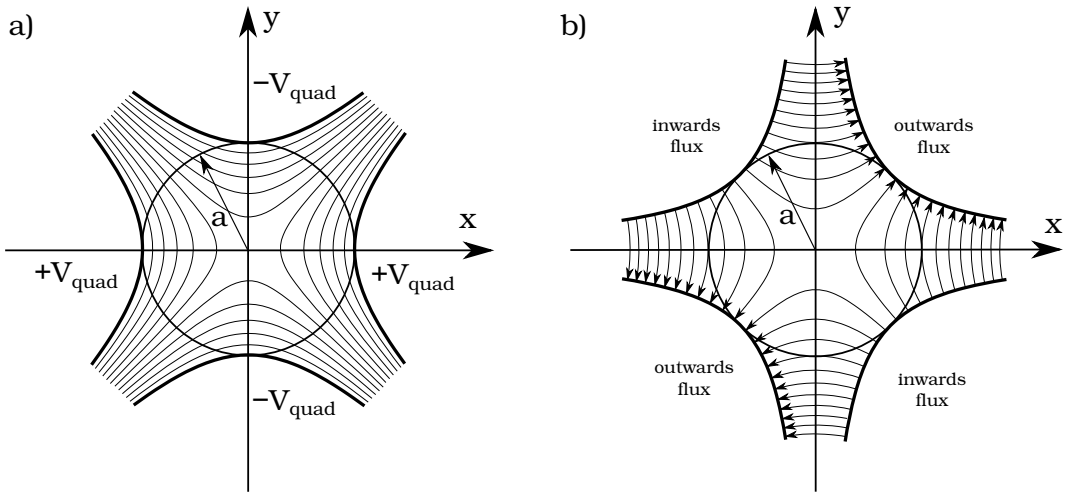

Figure 4.10: Quadrupole lenses: a) Electrostatic quadrupole with a being the distance from the optical axis to the electrode tip. Ten equipotential lines are drawn between potentials $-V_{\text{quad}}$ and $+V_{\text{quad}}$. b) Magnetic quadrupole with a being the distance from the optical axis to the pole tip, where magnetic field density is B_T. Magnetic field lines are illustrated by arrows. Both quadrupole lenses are illustrated as focusing in x-direction and defocusing in y-direction.

The quadrupole lenses are typically used as doublets or triplets for solutions, which are focusing in both transverse directions. Quadrupoles can also be used for transforming unsymmetric beams such as slit-beams from a Penning ion source for example, into a round beam.

4.3 Beam emittance

The ion beam travels in the beam transport line from one ion optical element to another along a curved path, which is usually defined as the longitudinal direction z. The transverse directions x and y are defined relative to the center of the transport line, the optical axis, where $x = y = 0$. The transport line is usually designed in such a way that a so-called reference particle travels along the optical axis with nominal design parameters. The ion beam (bunch) is an ensemble of charged particles around the reference particle with each individual particle at any given time described by spatial coordinates (x, y, z) and momentum coordinates (p_x, p_y, p_z). This six-dimensional space is known as the particle *phase space*. In addition to these coordinates, often inclination angles α and β or the corresponding tangents x' and y' are used. These are defined by

$$x' = \tan\alpha = \frac{p_x}{p_z} \quad \text{and} \quad y' = \tan\beta = \frac{p_y}{p_z}. \tag{4.25}$$

Traditionally the emittance is defined as the 6-dimensional volume limited by a contour of constant particle density in the (x, p_x, y, p_y, z, p_z) phase space. This volume obeys the Liouville theorem and is constant in conservative fields. With practical accelerators a more important beam quality measure is the volume of the *envelope* surrounding the beam bunch. This is conserved only in the case where forces acting on the particles are linear (see figure 4.11). Typically in the case of continuous (or long pulse) beams, where the longitudinal direction of the beam is of less interest, transverse distributions (x, x') and (y, y') are used instead of the full phase space distribution for simplicity. Also for these distributions the envelope surrounding the distribution changes when non-linear forces (unidealities of beam line elements for example) act on the particles. The size and shape of the transverse distribution envelope is an important quality measure for beams because most complex ion optical devices such as accelerators have an acceptance window in the phase space within which they can operate.

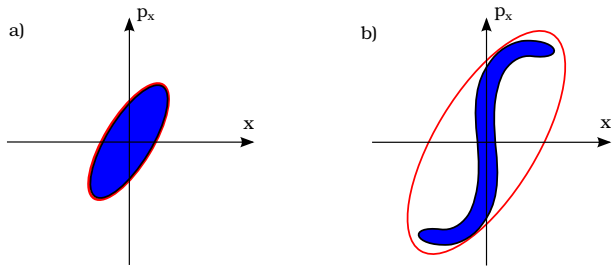

Figure 4.11: A 2-dimensional projection of an ensemble of particles before going through a non-linear optical system (a) and after it (b). The area of the particle distribution (shown in blue) is conserved but the area of the elliptical envelope (shown in red) increases.

4.3.1 Emittance ellipse

For calculation and modelling purposes a simple shape is needed to model the ion beam envelope in transverse (x, x') and (y, y') phase spaces. Real, low-aberration ion beam distributions usually have roughly elliptical contours. Therefore, it is an obvious solution to use ellipse as the model in the 2-dimensional phase spaces (and ellipsoids in higher dimensions). Equation for an origin-centered ellipse is

$$\gamma x^2 + 2\alpha x x' + \beta x'^2 = \epsilon, \tag{4.26}$$

where a scaling

$$\beta\gamma - \alpha^2 = 1 \tag{4.27}$$

is chosen. Here ϵ is the *2-dimensional transverse emittance* and α, β and γ are known as the *Twiss parameters* defining the ellipse orientation and aspect ratio. The area of

the ellipse is

$$A = \pi\epsilon = \pi R_1 R_2, \tag{4.28}$$

where R_1 and R_2 are the major and minor radii of the ellipse. Because of the connection between the area of the ellipse and ϵ there is sometimes confusion in whether to include the π in the above formula to quoted emittance values, the unit of emittance is often written as π·mm·mrad. This is done to emphasize that the quoted emittance number is the product of the radii and **not** the area of the ellipse. Always when communicating about emittance numbers it should be clearly indicated what the number is to avoid confusion [94]. In this work the pi is not included in the unit and ϵ is used as defined by eq. (4.28).

From equation 4.26 the dimensions of the ellipse can be calculated. Some of the most important dimensions needed in calculations are shown in figure 4.12.

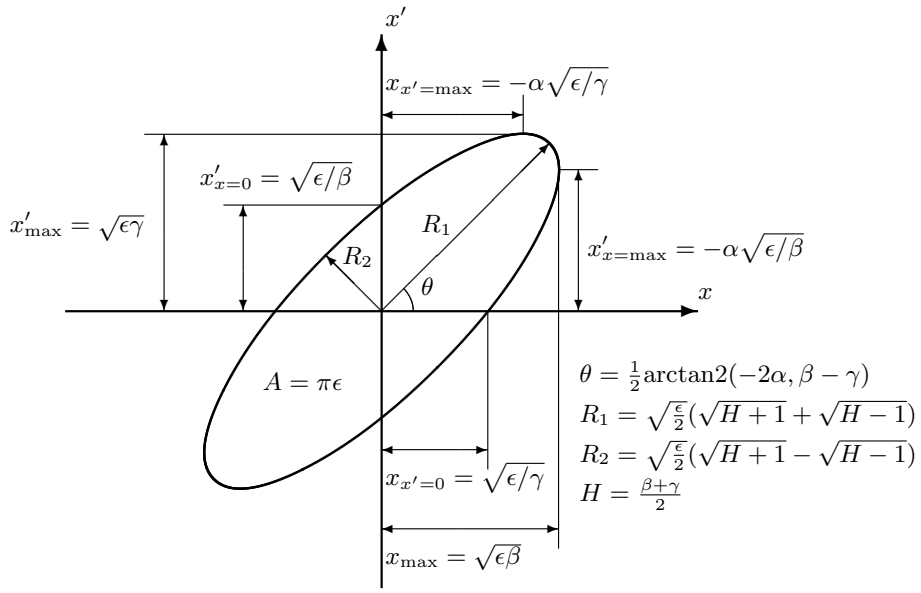

Figure 4.12: Emittance ellipse geometry with the most important dimensions.

4.3.2 Calculating rms emittance

How does ϵ and Twiss parameters relate to phase space distributions? How is the envelope defined? There are numerous ways to fit an ellipse to particle data. Often a minimum area ellipse containing some fraction of the beam is wanted (e.g. $\epsilon_{90\%}$), but unfortunately this is difficult to produce in a robust way. A well-defined way for producing the ellipse is by using a statistical definition known as the *rms emittance*

$$\epsilon_{\mathrm{rms}} = \sqrt{\langle x'^2 \rangle \langle x^2 \rangle - \langle x x' \rangle^2}, \tag{4.29}$$

with the expectation values defined as

$$\left\langle x^2 \right\rangle = \frac{\iint x^2 I(x,x')\,dx\,dx'}{\iint I(x,x')\,dx\,dx'}, \tag{4.30}$$

$$\left\langle x'^2 \right\rangle = \frac{\iint x'^2 I(x,x')\,dx\,dx'}{\iint I(x,x')\,dx\,dx'}, \tag{4.31}$$

$$\left\langle xx' \right\rangle = \frac{\iint xx' I(x,x')\,dx\,dx'}{\iint I(x,x')\,dx\,dx'}, \tag{4.32}$$

where $I(x,x')\,dx\,dx'$ is the magnitude of beam current at the differential area $dx\,dx'$ of phase space at (x,x'). Similarly, the Twiss parameters can be calculated from the particle distribution with

$$\alpha = -\frac{\langle xx' \rangle}{\epsilon}, \quad \beta = \frac{\langle x^2 \rangle}{\epsilon} \quad \text{and} \quad \gamma = \frac{\langle x'^2 \rangle}{\epsilon}. \tag{4.33}$$

For these formulas, it is assumed that the emittance distribution is centered to origin, so that $\langle x \rangle = 0$ and $\langle x' \rangle = 0$. With measured emittances additional difficulties arise from background noise and amplifier offsets in $I(x,x')$ data. Filtering methods for processing experimental data exists, from simple thresholding to more refined algorithms such as SCUBEEx [95].

4.3.3 Phase space distributions

A range of different beam phase space distributions have been encountered in practice. For theoretical work there are several distributions which are used for modelling beams. Three probably most used model distributions are Gaussian, KV (Kapchinskij-Vladimirskij), and waterbag distributions (or combinations of these). For continuous (non-bunched) beams the distributions are defined in 4D transverse phase space. For simplicity, the distributions given here are oriented along the axes. These distributions can be rotated in (x,x') and (y,y') planes to achieve more practical beams. In all of these cases the transverse emittances are $\epsilon_{\mathrm{rms,x}} = \sigma_x \sigma_{x'}$ and $\epsilon_{\mathrm{rms,y}} = \sigma_y \sigma_{y'}$, where σ_x, $\sigma_{x'}$, σ_y and $\sigma_{y'}$ are the standard deviations of the distribution.

The Gaussian distribution is given by

$$I(x,x',y,y') = \frac{1}{4\pi^2 \sigma_x \sigma_{x'} \sigma_y \sigma_{y'}} \exp\left(-\frac{1}{2} \left(\frac{x^2}{\sigma_x^2} + \frac{x'^2}{\sigma_{x'}^2} + \frac{y^2}{\sigma_y^2} + \frac{y'^2}{\sigma_{y'}^2} \right) \right). \tag{4.34}$$

In KV distribution the particles populate evenly the surface of an ellipsoid. The distribution is given by

$$I(x,x',y,y') = \frac{1}{\pi^2 x_0\, x'_0\, y_0\, y'_0}\ \delta(x^2/x_0^2 + x'^2/{x'_0}^2 + y^2/y_0^2 + y'^2/{y'_0}^2 - 1), \tag{4.35}$$

where x_0, x_0', y_0 and y_0' are the radii of the ellipsoid. The radii are related to the distribution standard deviations as $x_0 = 2\sigma_x$, $x_0' = 2\sigma_{x'}$, $y_0 = 2\sigma_y$ and $y_0' = 2\sigma_{y'}$. In waterbag distribution the particles evenly fill the volume of the ellipsoid. The distribution is given by

$$I(x, x', y, y') = \begin{cases} \frac{2}{\pi^2 x_0\, x_0'\, y_0\, y_0'} & \text{if } x^2/x_0^2 + x'^2/{x_0'}^2 + y^2/y_0^2 + y'^2/{y_0'}^2 < 1 \\ 0 & \text{otherwise,} \end{cases} \tag{4.36}$$

where the radii are related to the distribution standard deviations as $x_0 = \sqrt{6}\sigma_x$, $x_0' = \sqrt{6}\sigma_{x'}$, $y_0 = \sqrt{6}\sigma_y$ and $y_0' = \sqrt{6}\sigma_{y'}$. Cross-sections of these distributions are shown in figure 4.13a.

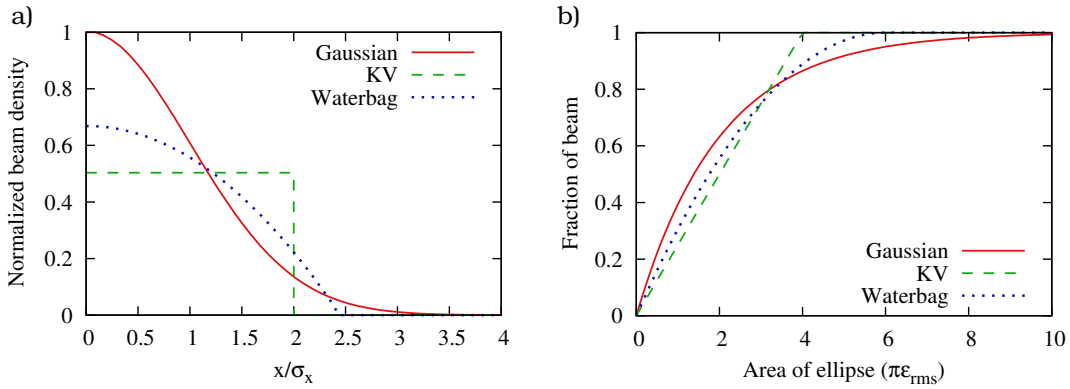

Figure 4.13: Gaussian, KV and waterbag distributions: a) cross-section of $\epsilon_{rms,x} = \sigma_x\sigma_{x'}$ beams oriented along the axes in x (or any other phase space coordinate), b) fraction of beam inside an ellipse with area relative to $\pi\epsilon_{\mathrm{rms}}$.

When dealing with emittance values it should be remembered that the fraction of the beam contained by the rms emittance ellipse depends on the particle distribution. For real measured distributions there is no direct rule but for known distributions this can be calculated. In figure 4.13b the beam fraction inside the ellipse (with same Twiss parameters as the rms emittance) is shown as a function of the area of the ellipse for Gaussian, KV and waterbag distributions. Because an ellipse with area 4 times the area of the rms ellipse fully encloses the KV distribution, the so-called 4-rms emittance is often used as the quoted number instead of 1-rms emittance. The waterbag distribution is fully enclosed inside 6 times the rms ellipse. The Gaussian distribution is infinite in size, the 1-rms ellipse contains 39 %, the 4-rms ellipse contains 86 % of the beam and the 6-rms ellipse contains 95 % of the beam.

4.3.4 Normalization of emittance

The transverse emittance defined in (x, x') space has the property that it is also dependent on the longitudinal beam velocity. If the beam is accelerated and p_z increases,

$x' = p_x/p_z$ decreases. This effect is taken into account by normalizing the velocity to the speed of light c, which gives

$$x'_n = \frac{p_x}{p_{z1}}\frac{v_{z1}}{c} = \frac{v_x}{c} = \frac{p_x}{p_{z2}}\frac{v_{z2}}{c} \tag{4.37}$$

at non-relativistic velocities. The *normalized emittance* can therefore be calculated from un-normalized or *geometric emittance* ϵ with

$$\epsilon_n = \epsilon\frac{v_z}{c} \tag{4.38}$$

in the un-relativistic limit, or with

$$\epsilon_n = \epsilon\beta\frac{1}{\sqrt{1-\beta}}, \tag{4.39}$$

where $\beta = v_z/c$ for relativistic particles.

4.3.5 Mismatch factor

The magnitude of the difference between two emittance ellipses having the same area and the same center can be quantified by evaluating the relative increase in radius of the first ellipse, which is needed to fully enclose the second ellipse with it. This relative increase in radius (area is used instead of radius in some literature) is known as the emittance *mismatch factor*. It can be shown that the mismatch factor is given by [96]

$$M = \left(\frac{1}{2}\left(R + \sqrt{R^2 - 4}\right)\right)^{1/2} - 1 \tag{4.40}$$

where

$$R = \beta_1\gamma_2 + \beta_2\gamma_1 - 2\alpha_1\alpha_2. \tag{4.41}$$

The mismatch factor can also be used for evaluating the ellipse shape (orientation and aspect ratio) difference of ellipses with differing sizes.

4.3.6 Emittance of extracted beam

An ion beam formed by letting charged particles from plasma to be emitted through a round aperture has an emittance defined by the plasma ion temperature T and the aperture radius r assuming that the acceleration to velocity v_z does not add aberrations. This minimum emittance can be calculated by using equations (4.29)–(4.32)

and using a particle distribution defined by circular extraction hole and Gaussian transverse velocity distribution

$$I(x, x') = \frac{2}{\pi r^2}\sqrt{r^2 - x^2}\ \sqrt{\frac{m}{2\pi kT}}\exp\left(\frac{-m(x'v_z)^2}{2kT}\right). \tag{4.42}$$

After normalization, the resulting rms emittance becomes

$$\epsilon_{\mathrm{rms,n}} = \frac{1}{2}\sqrt{\frac{kT}{m}}\frac{r}{c}. \tag{4.43}$$

The calculation can be made similarly for a beam extracted through an infinitely long and w wide slit. The resulting normalized rms emittance

$$\epsilon_{\mathrm{rms,n}} = \frac{1}{2}\sqrt{\frac{kT}{3m}}\frac{w}{c}. \tag{4.44}$$

In the round aperture case, the emittance of the beam is linearly proportional to the plasma aperture radius. On the other hand, beam current is roughly proportional to the area of the plasma aperture. Scaling of the aperture size does not therefore change the *beam brightness*

$$B = \frac{I}{\epsilon_{n,x} \cdot \epsilon_{n,y}} \tag{4.45}$$

in the first approximation.

The rms emittance of the ion beam is increased from the spread induced by the plasma ion temperature by several other phenomena. The non-linear focusing forces caused by highly curved plasma sheath and large diameter of the beam compared to the bore sizes of the electrodes produce aberrations in the beam, which are seen as rms emittance growth. In the case of negative ion sources the electron filter and electron dump magnetic fields may induce emittance growth due to inhomogeneities and by steering the beam off-axis. In ECR ion sources the solenoidal magnetic field of the ion source has a strong influence on the beam quality [97]. Also space charge forces discussed below may cause emittance growth.

4.3.7 Emittance measurement

Several types of devices have been developed and built for measuring $I(x, x')$, the beam intensity distribution in the phase space. In this work, an Allison emittance scanner [98] was used. The scanner shown in figure 4.14 is moved by a stepper motor to select a slice of the beam at coordinate x with the entrance slit of the device. Each slice is analyzed by a using a pair of deflector plates with $\pm V$ voltages to select an angular component x' to pass through the exit slit into a Faraday cup having

secondary electron suppression. The entrance angle of the ions passing through the slits is

$$x' = \frac{VL_{\text{eff}}}{2V_0 d}, \tag{4.46}$$

where $\pm V$ are the voltages on the deflector plates, L_{eff} is the effective length of the deflection electric field, V_0 is the voltage difference of the ion source and the beamline and d is the gap between the plates.

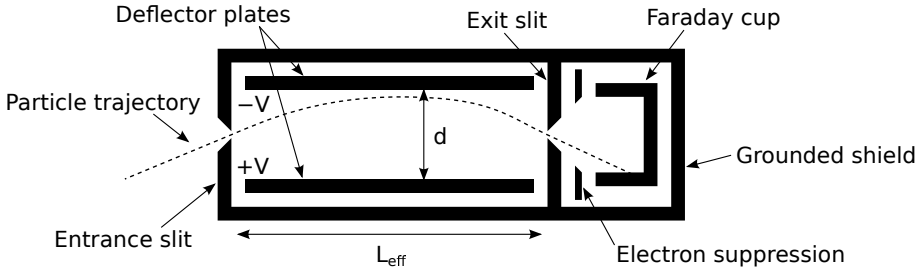

Figure 4.14: Schematic presentation of the Allison emittance scanner.

4.4 Space charge

The ion beam charge density

$$\rho = \frac{J}{v} = \frac{I}{Av} \tag{4.47}$$

plays a major role in beam extraction systems, where current densities are high and velocities are low compared to other parts of accelerator systems. The space charge induces forces, which increase the divergence and emittance decreasing the transportability of the beam. In the higher energy portions of the accelerator, the magnetic self-force of the beam starts compensating the space-charge blow-up. However, this effect is insignificant for $v \ll c$.

4.4.1 Space charge effects on beam

Assuming a cylindrical constant current density beam with radius r_{beam} propagating with constant velocity v_z, the beam generated electric field is given by Gauss law

$$E = \begin{cases} \frac{I}{2\pi\epsilon_0 v_z}\frac{r}{r_{\text{beam}}^2} & \text{if } r \leq r_{\text{beam}} \\ \frac{I}{2\pi\epsilon_0 v_z}\frac{1}{r} & \text{otherwise.} \end{cases} \tag{4.48}$$

The potential inside a beam line tube with radius r_{tube} is therefore

$$\phi = \begin{cases} \frac{I}{2\pi\epsilon_0 v}\left[\frac{r^2}{2r_{\text{beam}}^2} + \log\left(\frac{r_{\text{beam}}}{r_{\text{tube}}}\right) - \frac{1}{2}\right] & \text{if } r \leq r_{\text{beam}} \\ \frac{I}{2\pi\epsilon_0 v}\log\left(\frac{r}{r_{\text{tube}}}\right) & \text{otherwise.} \end{cases} \tag{4.49}$$

The potential distribution is plotted in figure 4.15 for a 10 mA, 10 keV H^- beam inside a 100 mm diameter beam line tube.

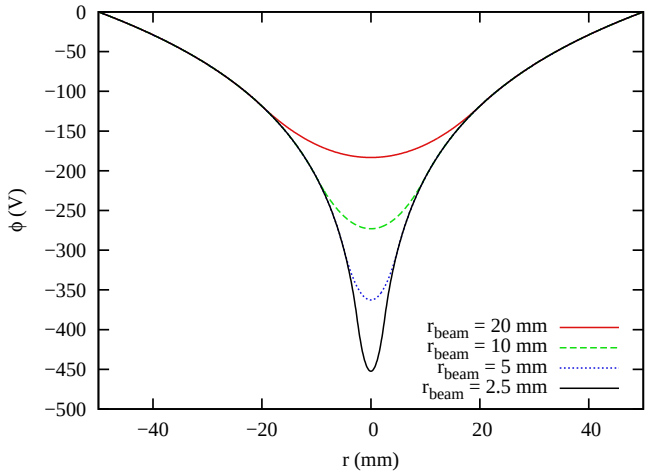

Figure 4.15: The potential distribution inside a cylindrical 100 mm tube with uncompensated 10 mA, 10 keV H^- beam

The electric field in the constant current density case, given by (4.48), is linear with radius and therefore does not cause emittance growth, but it causes increasing divergence of the beam. A particle at the beam boundary experiences a repulsive force

$$F_r = qE_r = ma_r = \frac{qI}{2\pi\epsilon_0 r v_z}. \tag{4.50}$$

Therefore, the particle acceleration is

$$a_r = \frac{d^2r}{dt^2} = \frac{d^2r}{dz^2}\frac{dz^2}{dt^2} = v_z^2\frac{d^2r}{dz^2}. \tag{4.51}$$

The particle trajectory is given by a differential equation

$$\frac{d^2r}{dz^2} = \frac{1}{v_z^2}a_r = K\frac{1}{r}, \text{ where} \tag{4.52}$$

$$K = \frac{qI}{2\pi\epsilon_0 m v_z^3}, \tag{4.53}$$

assuming that the beam divergence is small (i.e. (4.50) is valid). The differential equation can be integrated after change of variable $\lambda = \frac{dr}{dz}$, which gives

$$\frac{dr}{dz} = \sqrt{2K \log(r/r_0)}, \tag{4.54}$$

assuming $\frac{dr}{dz} = 0$ at $z = 0$. The solution is separable and can be again integrated to achieve a final solution [99]

$$z = \frac{r_0}{\sqrt{2K}} F\left(\frac{r}{r_0}\right), \text{ where} \tag{4.55}$$

$$F\left(\frac{r}{r_0}\right) = \int_{y=1}^{r/r_0} \frac{dy}{\sqrt{\log y}}. \tag{4.56}$$

The last integral is not analytic, but can be numerically integrated for estimates of divergence. As an example, a parallel zero-emittance beam of H^- accelerated with 20 kV has initial radius of $r_0 = 5$ mm. The size of a 5 mA beam after a drift of 200 mm can be solved from $F(r/r_0) = 1.913$, which gives $r = 9.1$ mm.

The finite plasma temperature often leads to beams with roughly bi-Gaussian distributions. This kind of distribution leads to non-linear space charge forces, that cause emittance growth in addition to increase of beam divergence. Computer simulations are required to calculate these effects.

4.4.2 Space charge compensation

The potential well of the beam formed by the accelerated charged particles acts as a trap for oppositely charged particles in regions where there are no external electric fields to drain the created charges. The trapped particles compensate the charge density of the beam decreasing the depth of the potential well and therefore also decreasing the magnitude of the beam space charge effects described above. This process is called *space charge compensation*, SCC. The most abundant process for the production of compensating particles is the ionization of the background gas within the beam. In the case of positive ion beams, the electrons produced by the background gas ionization are trapped in the beam, while slow positive ions are repelled to the beam line walls. In the case of negative ion beams, the compensating particles are positive ions created in collisions of the beam particles with background gas molecules, e.g.

$$H^- + H_2 \rightarrow H^- + H_2^+ + e \tag{4.57}$$

Other process such as $H^- + H_2 \rightarrow H^+ + H_2 + 2e$ also take place, but the created positive ions have such high velocity that their contribution to SCC is negligible.

The creation rate of the compensating particles can be estimated with

$$\frac{dn_c}{dt} = \Phi n_{\text{gas}} \sigma_i, \tag{4.58}$$

where Φ is the flux of beam particles, n_{gas} is the gas density and σ_i is the corresponding ionization cross section. The final compensation degree achieved in a real system is difficult to estimate accurately because it depends on the life time of the compensating particles in the potential well. The most important processes affecting the life time are (1) longitudinal leakage of particles, which can be limited by electrostatic electrodes with correct polarity or magnetic fields for example, (2) recombinative processes and (3) scattering processes leading to ejection of particles from the potential well. Assuming that the losses are low enough, the time scale for achieving approximately full compensation is

$$\tau = \frac{\rho_{\text{beam}}}{e\frac{dn_c}{dt}} = \frac{Q}{v n_{\text{gas}} \sigma_i}, \tag{4.59}$$

where Q is the charge state of beam and v is the velocity of the beam. This equation can be used for example to estimate if compensation is possible in pulsed beams. According to experimental and computational studies, in typical H_2 pressure range of about 10^{-5}–10^{-6} mbar, full compensation of H^- beam is achieved in 10–100 μs [100, 101].

In high beam intensity LEBT systems a controlled amount of background gas is often added to the vacuum chamber to increase the amount of compensation. Small beam losses in the increased ionization processes can lead to increase in total beam transmission due to decreased divergence and emittance growth. The magnitude of the compensation in beam transport can be estimated for example with measurement of the energy distribution of the charged particles ejected from the beam as a function of background gas pressure [102]. There are also computer codes for self-consistent modelling of the relevant processes affecting the SCC [103, 104]. With other beam transport programs a typical solution is to scale the beam current locally with the SCC factor estimated by the user.

4.5 Computational methods

As mentioned already, modelling and analysis of ion source plasma, beam extraction and transport systems is so complicated that most of the work is done using specialized computer codes capable of simulating the relevant physical processes. For this purpose there are a vast number of codes, all with somewhat different capabilities and methods. Many of the codes are, or have been, developed in academic institutions for research purposes, but there are also commercial codes available. These codes can be

categorized into three groups: (1) codes including modelling of the creation and destruction of charged particle in plasma, (2) trajectory codes without plasma modelling capabilities and (3) codes with a simplified plasma model for simulating the particle extraction. The code developed in this work belongs in the third group.

4.5.1 Plasma codes

The plasma codes for ion sources are generally based on modelling the dynamics of particles using so-called *particle in cell* (PIC), *fluid* or hybrid models [105]. The PIC algorithm is based on tracking an ensemble of charged particles using fundamental equations in a system where the particle-particle forces are not calculated explicitly, but the electric (and possibly magnetic) field generated collectively by the particles inside a computational cell affects other particles [106]. The fluid model is based on solving equations governing macroscopic quantities such as densities and fluxes of particles in a discretized system. Hybrid codes combine these two methods, for example by using fluid description for neutrals and PIC for charged particles. The evolution of the system from the starting conditions is done by time stepping until a quasi-steady-state situation is reached. These codes often use Monte Carlo methods for modelling the particle collisional processes, including the generation and destruction of different particle species and excited states in plasma volume and on surfaces. Some of the codes model generation of electrons from hot filaments [107] or electron heating by RF from first principles [108] and some simulations are driven by a plasma boundary conditions with user-given properties [109]. The codes are capable of predicting plasma processes leading to extraction of ions with reasonable accuracy without making too many assumptions on the plasma processes. The running times of these codes in 3D are generally measured in days or weeks on high-performance parallel computers, which can be prohibitive for some work, for example optimization of extraction systems. The codes are also often customized for a specific problem and are therefore not easily adapted for modelling other systems. Recently the most impressive modelling efforts with this type of codes have been made for understanding and optimization of negative ion sources for fusion neutral beam heating systems [110, 111, 112]. Unfortunately these codes are still far from being tools which could be used for developing ions sources and extraction systems.

4.5.2 Trajectory codes

The so-called trajectory codes have a capability of tracking the particle trajectories from their starting points through the beam transport line. For transport lines consisting of standard ion optical elements, there is a class of codes using transfer matrix formalism, which describe the effect of ion optical elements (and drifts between them)

on trajectories using transfer matrices [92, 113]. For systems consisting of arbitrary electric and magnetic fields, i.e. extraction systems, the fields have to be calculated from the electrode and magnet geometries using field solvers. For this type of problems there are a lot of commercial codes, including SimIon [114], Cobham Vector Fields [115], and Integrated Engineering Software Lorentz [116], to name a few. Most of this type of codes have the capability of tracking particles through the fields by integrating the Lorentz force. Some of them also have models for taking into account beam generated electrostatic and magnetic forces.

4.5.3 Plasma extraction codes

The plasma extraction codes or *gun-type* codes are very much like the trajectory codes described above, but these also include capabilities for starting beams from the space charge compensated plasma and modelling the propagation of the beams to unneutralized extraction region. This is done by depositing the beam space charge on a simulation grid and using analytical models for the plasma space charge compensation for fast but sufficiently accurate modelling of the plasma sheath effects. The method also leads to a high quality modelling capability of beam space charge effects.

The plasma extraction codes have a long history starting from the pioneering work by S. A. Self and J. H. Whealton in the sixties and seventies [117, 118, 119]. More recent codes being used for modelling extraction systems include PbGuns [120] and IGun [121], which are both capable of modelling two-dimensional and cylindrically symmetric positive and negative ion plasma extraction systems, and Kobra-INP [122], which is a three-dimensional code for positive ion plasma extraction. When the author started working in the field in 2004, there were no codes available for modelling negative ion plasma extraction in three dimensions, which is required in many cases due to the effects of magnetic filter and the electron dump field on the beam even if the extraction is otherwise cylindrically symmetric. In many cases modelling of such extraction systems had been done using a combination of cylindrically symmetric simulations for modelling ion beam plasma extraction and three dimensional simulations for the effects of the magnetic fields, but coupling simulations like this in the extraction area is always difficult and induces errors in modelling. The lack of tools needed for modelling such systems has led to the development of the plasma extraction code IBSimu, which is presented in detail in the following chapter.

Chapter 5

Developed computational tools

A three-dimensional electrostatic code for simulating extraction of electrons and positive and negative ion beams from plasmas has been developed with a capability of also modelling systems with lower dimensionality. An overall description of the code is given in this chapter with detailed description of the main numerical methods used. The code has been published as IBSimu — Ion Beam Simulator, under the GNU General Public License (GPL) and made publicly available for the community [7, 123].

The simulation code is not distributed as a pre-compiled binary as most commercial software. It is made as a C++ computer library, which contains the modules (or classes) capable of performing the computational work. The simulations are done by user-made programs utilizing the computational methods through a programming interface of the library. This choice makes the code very versatile, which enables a wide range of problem types to be solved. The built-in modules can be replaced if customization is required and the modules can be integrated into other codes. The programming interface also enables easy batch processing and automation of simulations for systematic studies. The code also contains an interactive easy-to-use graphical user interface for plotting geometries, fields and particle trajectories.

5.1 General description

The time-independent plasma extraction systems can be modelled with Poisson equation

$$\nabla^2 \phi = -\frac{\rho}{\epsilon_0} \tag{5.1}$$

describing the relation between the electric potential and the space charge and time-independent Vlasov equation

$$\vec{v} \cdot \nabla f - \frac{q}{m} \left(\vec{E} + \vec{v} \times \vec{B} \right) \cdot \frac{\partial f}{\partial \vec{v}} = 0 \tag{5.2}$$

describing the behavior of the particle distribution $f(\vec{r}, \vec{v})$ in the electric field $\vec{E} = \nabla\phi$ and independent magnetic field $\vec{B}$. The space charge density in (5.1) is given by

$$\rho = q \int f \, d\vec{v} + \rho_{\mathrm{pl}}(\phi), \tag{5.3}$$

where $\rho_{\mathrm{pl}}(\phi)$ is the space charge density from the plasma model, which is a non-linear function of the potential as described in the next section 5.2. The solution of the coupled system (5.1)–(5.3) is sought in a bound geometry with sufficient boundary conditions to make the problem well-defined.

Many of the plasma extraction problems require three-dimensional modelling as is the case with all of the negative ion extraction systems discussed in this thesis. Still, there are a large number of ion optics problems, which can be modelled by taking advantage of the system symmetry and, therefore, lowering the dimensionality of the problem. Two types of such systems are often encountered: slit beam systems and cylindrically symmetric systems. Cylindrically symmetric systems can be modelled in the cylindrical coordinates (z, r, θ), where the system has no variation as a function of θ making it effectively two-dimensional. Slit beam systems are modelled assuming that the slit length is infinite and it is sufficient to model the system in two dimensions (x, y). In practice this is a good approximation in the center of a slit beam ($z = 0$) in systems with beam length-to-width ratio of 10 or higher. Because the requirements for computational resources are much less demanding for the two-dimensional problems even many of the systems requiring three-dimensional modelling are initially designed with some approximations using two-dimensional modelling. This allows the designer to make tens of simulations optimizing the system in the same time that would be spent making only one simulation in 3D. To enable this type of design workflow the simulation code was made with capability of simulating 2D and cylindrically symmetric systems in addition to 3D. This chapter mainly concentrates on the 3D modelling, while the 2D specific formulation is presented in appendix C.

To solve the problem (5.1)–(5.3) with computational methods, the fields including ϕ, ρ and $\vec{E}$ are represented in the calculation domain using a grid of computation points. The solution of the resulting discrete problem is sought with an iterative process sometimes called the Vlasov-Poisson iteration (see figure 5.1 for a flow chart describing simulation code, including the iteration cycle). The easiest way to start the iterative process is by providing an initial guess for the electric potential ϕ by solving the Laplacian $\nabla^2\phi = 0$ in the geometry and assuming that the potential inside the assumed plasma region is the plasma potential ϕ_P in the case of positive ion plasma extraction and 0 in the case of negative ion plasma extraction problems. For positive ion extraction there exists analytical methods for estimating the plasma sheath location [124], but with negative ion extraction the user has to manually enter the initial location. With good enough starting point a convergent iteration is achieved. If no plasma exists in the simulation (a beam transport problem for example), the

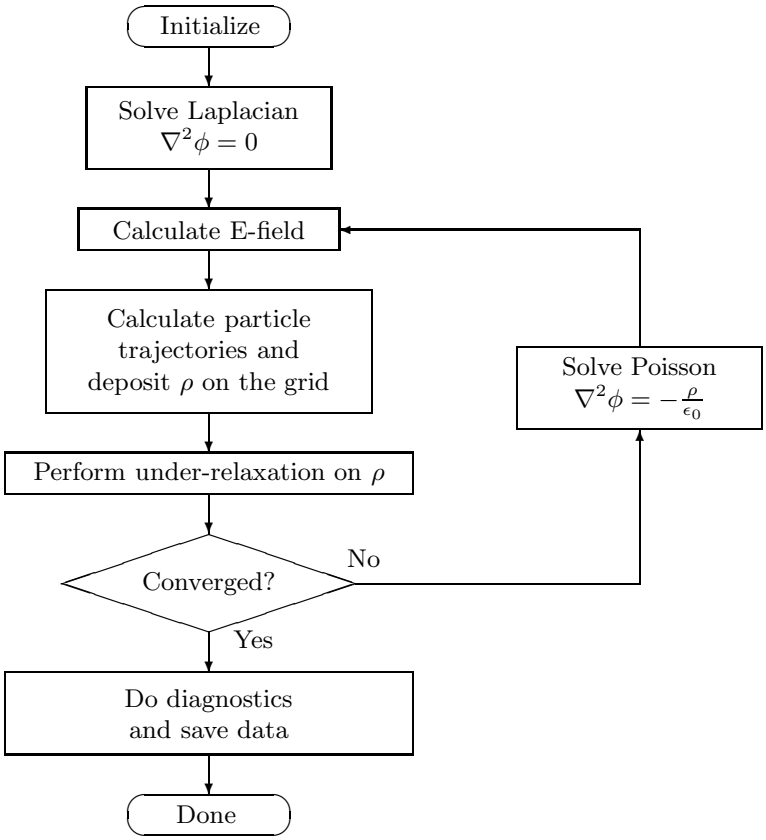

Figure 5.1: General flow chart of the simulations.

Laplacian is solved without the fixed potential plasma volume to provide a starting point for the iteration. The resulting ϕ will then be used to calculate the electric field, which is used to calculate the particle trajectories starting from the plasma (or any other defined starting point). The continuity equation (5.2) is not used to calculate the particle dynamics even though it was used to introduce the problem and it gives the name to the iterative method. A more practical method known as ray-tracing is employed, which integrates the equations of motion of the particles in the calculated $\vec{E}$ and imported $\vec{B}$-fields. Next the space charge density ρ_{rt} is calculated on the grid based on the ray-traced trajectories. This space charge density is then used together with the analytic space charge density from the plasma model $\phi_{\mathrm{pl}}(\phi)$ in the non-linear Poisson equation to provide the electric potential ϕ for the next iteration round. Quite often in the iterative process, the change in ϕ overshoots preventing convergence. This can be avoided by damping the correction step taken at each iteration round. In this work this is done by performing under-relaxation on the space charge density from ray-tracing. After achieving convergence the simulation data is saved and/or diagnostics is made before stopping the calculation. Different parts of the simulation code are discussed in greater detail in the following sections.

5.2 Plasma models

In the case of ion plasma extraction, the beam formation is dependent on complicated interactions of plasma particles, geometry and electric and magnetic fields. In this work modelling of the beam formation is restricted to the sheath region, into which the extracted particles arrive with an initial velocity due to acceleration in the pre-sheath and where the charge density of the compensating charges is assumed to be dependent only on the potential.

5.2.1 Positive ion plasma extraction model

The standard non-collisional model for the positive ion plasma sheath was presented in section 2.4.1. The same equations are used in the case of extraction modelling, but in higher dimensions as the particle dynamics of the system is highly dependent on the boundary conditions (geometry), which do not exist in the one dimensional system (see figure 5.2). The compensating electron charge density in plasma modelling is given by

$$\rho_{\mathrm{e}} = \rho_{\mathrm{e0}} \exp\left(\frac{e(\phi - \phi_P)}{kT_e}\right), \tag{5.4}$$

which is a function of the potential. The electron density is equal to the ion density at plasma potential (or more exactly the potential at the sheath edge) and decays

exponentially towards the extraction. Far enough in the extraction, the compensation becomes (essentially) zero. The ray-traced positive ions are injected to the simulation on the boundary of the computational domain, which is assumed to be the sheath-presheath boundary (at ϕ_P) with velocity not less than the Bohm velocity v_B to achieve convergence.

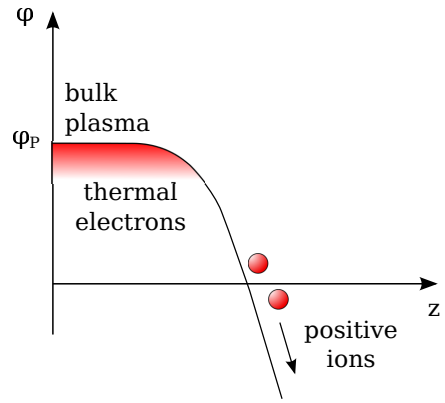

Figure 5.2: Schematic presentation of the positive ion extraction model with thermal electrons populating the bulk plasma and positive ions accelerated by the extraction field through the plasma sheath.

5.2.2 Negative ion plasma extraction model

The negative ion plasma extraction model used in this work is implemented according to the guidelines of references [125] and [126]. The bulk plasma is assumed to have a positive plasma potential ϕ_P and it is separated from the plasma electrode at $\phi = \phi_{\text{wall}} = 0$ V by a plasma sheath. It is assumed that the extractable negative ions, which are either volume or surface produced, are born close to the wall potential and are extracted from a uniform plasma. These charges together with the plasma electrons form a potential well and counteract the formation of a saddle point. The saddle shaped potential distribution would form at the plasma electrode aperture between positive bulk plasma and extraction regions without excess of negative charges. According to reference [125], the non-existence of the saddle point is supported by the observed low beam emittances from H^- ion sources, while most more refined plasma simulations [110, 111] show saddle shaped potentials. In the plasma model described here, the potential deviates from zero going into the bulk plasma due to the plasma potential and towards the extraction due to the acceleration voltage. This potential structure causes positive ions from the bulk plasma to be accelerated towards the extraction, having energy $e\phi_P$ at the zero potential. These ions propagate until they are reflected back to the plasma by the increasing potential in the extraction. The potential well acts as a trap for thermal positive ions. The negative ions and electrons

are accelerated from the wall potential towards the bulk plasma and more importantly towards the extraction. Schematic view of the negative ion extraction model is shown in figure 5.3. [8]

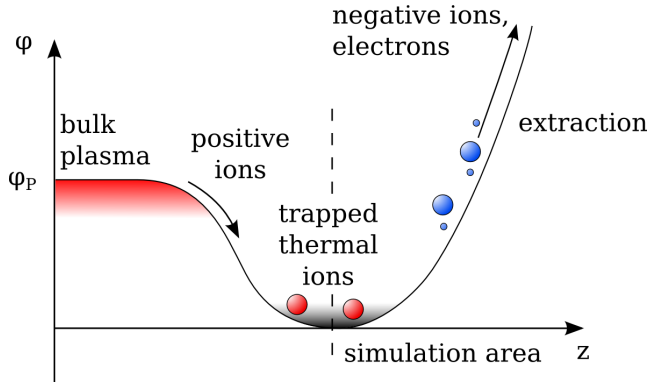

Figure 5.3: Schematic presentation of negative ion plasma extraction model with fast positive ions flowing from bulk plasma towards the extraction, thermal positive ions populating the potential well at the plasma electrode potential and negative charged particles accelerated by the extraction field.

The negative ion plasma sheath from the zero potential towards the extraction, which is the region included in the simulation, can be described by the Poisson equation, where total charge density $\rho = \rho_{\mathrm{neg}} + \rho_{\mathrm{f}} + \rho_{\mathrm{th}}$. Here ρ_{neg} is the space charge density of negative ray-traced particles, ρ_{f} is the space charge of fast positive ions and ρ_{th} is the space charge of trapped positive thermal ions. The model allows several negative ion species to be extracted from the ion source and also many positive ion species to be used as compensating plasma particles. Each of the thermal ion species is assumed to have a separate Maxwellian velocity distribution with the associated space charge distribution

$$\rho_{\mathrm{th}} = \rho_{\mathrm{th0}} \exp\left(\frac{-e\phi}{kT_p}\right), \tag{5.5}$$

where ρ_{th0} is the space charge density of the thermal ion species at the wall potential and T_p is the corresponding thermal positive ion temperature. In all cases presented in this work only one thermal species has been defined. Therefore it is sufficient to use only one symbol T_p. This is done because in most cases no information about the temperatures of different positive ion species is available.

The fast ions are decelerated and turned back to plasma by the extraction voltage. The space charge distribution of the fast ions is assumed to be given by

$$\rho_{\mathrm{f}} = \rho_{\mathrm{f0}} \left(1 - \mathrm{erf}\left(\frac{\phi}{\phi_p}\right)\right), \tag{5.6}$$

where ρ_{f0} is the space charge density of fast ions at the wall potential. In the original work [126] the fast ion space charge ρ_{f} has a linear dependence on potential. That formulation was changed to the one presented here to achieve continuous differentiability

required by the numerical methods, while preserving the main trend of the original function. The slight change in the decay of ρ_{f0} is not expected to cause significant deviation in the results. The quasi-neutrality of the plasma requires $\rho = 0$ at $\phi = 0$ V resulting in $\rho_{\mathrm{neg0}} + \rho_{\mathrm{f0}} + \rho_{\mathrm{th0}} = 0$, where ρ_{neg0} is the total negative beam space charge density at the definition plane, which is typically the boundary of the computational domain, which is at zero potential. The beam space charge density at the definition plane

$$\rho_{\mathrm{neg0}} = \sum_j \frac{J_j}{v_{0,j}}, \tag{5.7}$$

where J_j is the current density and $v_{0,j} = \sqrt{2E_{0,j}/m_j}$ is the initial drift velocity of the extracted species j. For a typical case where negative ions and electrons are extracted the ion current density J_{H^-} is defined explicitly and the electron current density $J_{e^-} = R_{ei}J_{H^-}$ is defined using electron to ion beam current ratio R_{ei}. The initial drift energies for both species are defined equally as E_0. The relative densities of the compensating distributions in the plasma are defined by the ratio of fast compensating positive ions to total negative charge density

$$R_f = \frac{\rho_{\mathrm{f0}}}{\rho_{\mathrm{neg0}}}. \tag{5.8}$$

The negative ions and electrons are ray-traced from the definition plane along artificial straight trajectories until they are accelerated by electric field at the self-consistently calculated plasma sheath. In reality the plasma particles are collisional and obey the magnetic field, which in typical negative ion sources is quite significant at the extraction aperture, especially for the electrons. The real particle dynamics is difficult to model in this type of code and therefore the magnetic field is suppressed inside the plasma to provide an even flux of particles to the sheath. The magnetic field suppression is cancelled after the extracted particles have propagated to potential higher than some threshold value ϕ_{Bsup}. In most cases the threshold value should be around 1–20 V as this corresponds to the energy range where collisional properties become negligible and particles start (mostly) following paths defined by Lorentz force. The physically correct threshold value is hard to estimate accurately, but it is not relevant in this context because the ion optics has been observed not to be very sensitive to the threshold value in most cases.

According to the simplified modelling of the electrons in the sheath region the current density of the extracted electron beam in the simulation model is directly proportional to the space charge density of the electrons in the proximity of the sheath with $J = \rho/v$. In reality the magnetic field plays a role in the extraction process by confining part of the electrons inside the plasma, which would be extracted without the magnetic field. Because of this the electron space charge density in the plasma sheath region is too low for a given extracted electron beam current density in the model. To compensate for this deficiency of the model a simple semi-empirical correction factor

has been included in the model: the electron space charge density in the plasma sheath region is corrected by multiplying it with the electron density coefficient R_{ec}. This correction is applied in a region, where the potential is less than the threshold value ϕ_{ec} similarly to the magnetic field suppression described above. In this work $\phi_{ec} = 2\phi_p$ has been used as the threshold. The greatest challenge with the R_{ec} parameter is that its prediction is almost impossible without making systematic measurements of the beam formation as its value depends on the magnetic field distribution, geometry, neutral pressure, etc. at the sheath region.

All the input parameters of the negative ion plasma extraction model are listed in appendix B for reference purposes together with other computational parameters of the IBSimu code.

5.3 Discretization of electrostatics problem

The partial differential equations, which arise from electromagnetics require some kind of discretization to be solvable by numerical methods in arbitrary geometries. Several methods have been developed for formulating such systems. The most used ones in electromagnetics are finite difference method (FDM) [127], finite element method (FEM) [128], boundary element method (BEM) [129], and their variants. The most straightforward method is the standard FDM, where the solution domain is divided into a regular grid of points, in which the fields are bound by differential equations in discrete form. This method has been used in this work and is therefore discussed below in greater detail.

In FEM the calculation domain is usually partitioned with a polyhedral mesh conforming to the geometry. Continuous field interpolation functions are used inside the mesh elements and the discrete formulation is constructed by using the integral form of the governing equations. Superior solution accuracy is available from FEM formulation compared to FDM, but there are disadvantages: The finite element formulation is more complex, the generation of high-quality polyhedral meshes in three dimensions is very difficult and the random access evaluation of electric field needed for particle trajectory calculation is slow compared to FDM, where a regular grid is used. In practice if FEM was used for making extraction simulations an external computer library would be needed for mesh generation because constructing a robust meshing tool can take years and is worth a Ph.D. thesis on its own [130, 131]. Unfortunately no adequate freely available computer libraries were available for this task at the time when development of the extraction code was initiated, which was the main reason for choosing FDM instead of FEM.

The boundary element method formulates the problem as an equivalent source problem. In case of electrostatics, this means that the distribution of charge on electrode

surfaces is sought, which satisfies the fundamental boundary conditions, i.e. no electric field inside conductors. Therefore BEM does not need discretization of the volume — only surface meshing is needed. The BEM provides the highest field accuracy of the methods presented here but the evaluation of electric field is very slow because the field at any location is dependent on all the charges in the computation.

Comparisons of programs using these methods for electrostatic charged particle problems have been made [132], but these results should not be used as an indication of the efficiency or accuracy of the fundamental methods in general because the implementations used in the programs and the selection of problems may have an effect on the results. For example the poor accuracy of the FDM in the comparison is mainly due to the crude surface approximation used in the SimIon code. Also the efficiency of BEM is over-estimated in the low-particle-count problems selected for the study.

5.3.1 Computation domain

In this work, the three-dimensional computation domain is defined as a Cartesian grid with regular step size h. The grid is defined by *planes*

$$x_i = x_{\min} + h \cdot i \tag{5.9}$$
$$y_j = y_{\min} + h \cdot j \tag{5.10}$$
$$z_k = z_{\min} + h \cdot k, \tag{5.11}$$

where $i = 0, \ldots, I-1$, $j = 0, \ldots, J-1$ and $k = 0, \ldots, K-1$. The grid planes divide the computation domain into grid *cells*

$$C_{i,j,k} = \{(x, y, z) \mid x \in [x_i, x_{i+1}],\, y \in [y_j, y_{j+1}],\, z \in [z_k, z_{k+1}]\} \tag{5.12}$$

and define the computation *nodes*

$$(x_i, y_j, z_k) = (x_{\min} + h \cdot i,\, y_{\min} + h \cdot j,\, z_{\min} + h \cdot k), \tag{5.13}$$

at which the space charge density and electric potential fields are defined. The same node indices are used also for the field values at the node locations to simplify the notation, for example $\phi_{i,j,k} = \phi(x_i, y_j, z_k)$. The computation domain spans from $x_{\min}$ to $x_{\max} = x_{\min} + h(I-1)$ in x-direction, from $y_{\min}$ to $y_{\max} = y_{\min} + h(J-1)$ in y-direction and from $z_{\min}$ to $z_{\max} = z_{\min} + h(K-1)$ in z-direction. The computation domain may have electrodes or *solids* in it, where the electrostatic potential has a constant, predefined value. The potential outside the solids is defined by the boundary conditions on the solid surfaces and the boundary of the computation domain (planes $x = x_{\min}$, $x = x_{\max}$, …, $z = z_{\max}$) and has to be solved using the Poisson equation.

In 2D the computation grid is defined equally in (x, y) coordinates just by omitting the z-dimension. An example of a 2D grid is shown in figure 5.4. Cylindrically symmetric systems are discretized into computation nodes

$$(z_i, r_j) = (z_{\min} + h \cdot i,\ h \cdot j), \tag{5.14}$$

which gives the first $j = 0$ line of nodes on the symmetry axis.

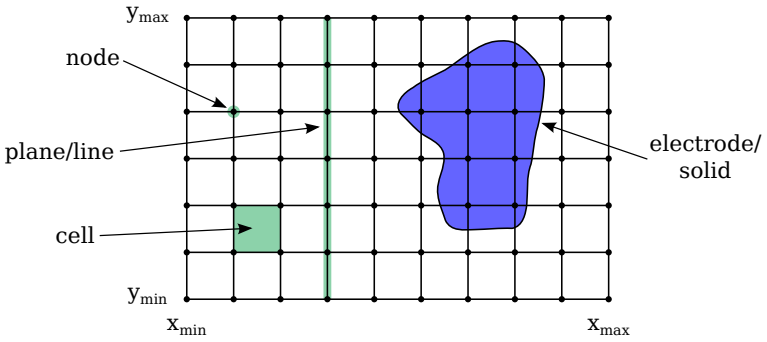

Figure 5.4: Two-dimensional computation grid with examples of node, cell and grid line identified and part of the geometry covered by a solid.

5.3.2 Finite difference formulation of Poisson equation

In FDM the derivatives in the governing differential equations are replaced by finite differences using field values at node locations. The finite difference formulas used can be derived using Taylor's theorem, which states that a sufficiently smooth function $f(x)$ can be approximated close to x_0 with a polynomial

$$f(x_0 + h) = f(x_0) + \frac{f'(x_0)}{1!}h + \frac{f''(x_0)}{2!}h^2 + \cdots + \frac{f^{(n)}(x_0)}{n!}h^n + R_n(x_0 + h), \tag{5.15}$$

where $R_n(x_0 + h)$ is a remainder term. It can be shown that there exists a number $\xi \in [x_0, x_0 + h]$ such that the remainder

$$R_n(x_0 + h) = \frac{f^{(n+1)}(\xi)}{(n+1)!}h^{n+1}. \tag{5.16}$$

The second derivative of function for example is derived by using Taylor's theorem at $x_0 + h$ and $x_0 - h$ with third order precision:

$$f(x_0 + h) = f(x_0) + \frac{f'(x_0)}{1!}h + \frac{f''(x_0)}{2!}h^2 + \frac{f'''(x_0)}{3!}h^3 + R_3(x_0 + h) \tag{5.17}$$

$$f(x_0 - h) = f(x_0) - \frac{f'(x_0)}{1!}h + \frac{f''(x_0)}{2!}h^2 - \frac{f'''(x_0)}{3!}h^3 + R_3(x_0 - h). \tag{5.18}$$

The first and third derivatives cancel when summing the equations and therefore

$$f''(x_0) = \frac{f(x_0 - h) - 2f(x_0) + f(x_0 + h)}{h^2} + O(h^2). \tag{5.19}$$

where $(R_3(x_0+h)+R_3(x_0-h))/h^2$ has been replaced with $O(h^2)$ describing the error term in big-O notation. Similarly other derivatives can be derived from the Taylor polynomial.

The three-dimensional Poisson equation in Cartesian coordinates

$$\nabla^2\phi = \frac{\partial^2\phi}{\partial x^2} + \frac{\partial^2\phi}{\partial y^2} + \frac{\partial^2\phi}{\partial z^2} = -\frac{\rho}{\epsilon_0} \tag{5.20}$$

becomes

$$\phi_{i-1,j,k} + \phi_{i+1,j,k} + \phi_{i,j-1,k} + \phi_{i,j+1,k} + \phi_{i,j,k-1} + \phi_{i,j,k+1} - 6\phi_{i,j,k} = -h^2\frac{\rho_{i,j,k}}{\epsilon_0} \tag{5.21}$$

by approximating the derivatives with finite difference formula (5.19). The Poisson equation therefore gives a dependency of the potential on the node from its six nearest neighbors and from the space charge density at the node itself. This is the simplest and most common formulation for the Poisson equation in a regular grid. It is also possible to use higher order approximations for the second derivative, but this was not done in this work due to added complexity of the algorithm and because it is argued that the increase in accuracy is not worth the additional computation time in this case.

Due to the finite size of the computation domain, there are boundary nodes which need restraints for the problem to be well posed. The simplest restraint is known as the *Dirichlet boundary condition*, which specifies the potential

$$\phi(x, y, z) = f_D(x, y, z) \tag{5.22}$$

on the boundary. Another boundary condition commonly used in electrostatics is the *Neumann boundary condition*, which specifies the derivative of the potential with respect to the boundary normal pointing away from the solid

$$\frac{\partial\phi}{\partial\vec{n}}(x, y, z) = f_N(x, y, z) \tag{5.23}$$

on the boundary. Other boundary conditions exist but are seldom used in electrostatics. The finite difference formulation for the Dirichlet boundary condition is simply the value of the boundary potential at the node location $\phi_{i,j,k} = f_{D,i,j,k}$. The Neumann boundary condition is discretized by replacing the derivative with the central finite difference, for example

$$\frac{\partial\phi}{\partial x}(x_i, y_j, z_k) = \frac{\phi_{i+1,j,k} - \phi_{i-1,j,k}}{2h} + O(h^2) \tag{5.24}$$

for the $x_{\min}$ boundary if the simplest central difference formula for derivative is used. This can be combined with the discretized Poisson equation at (i, j, k) to eliminate the references outside the grid. Thus, the Neumann boundary condition becomes

$$2\phi_{i+1,j,k} + \phi_{i,j-1,k} + \phi_{i,j+1,k} + \phi_{i,j,k-1} + \phi_{i,j,k+1} - 6\phi_{i,j,k} = -h^2 \frac{\rho_{i,j,k}}{\epsilon_0} + 2hf_{N,i,j,k} \quad (5.25)$$

and similarly for other boundaries.

The discrete Poisson equation (5.21) could be used together with the boundary conditions described above on the computation domain boundaries and the nodes inside the solids having fixed potential values. This kind of solution is the simplest Dirichlet boundary condition for arbitrarily shaped solids and gives a low-quality estimate of the potential close to the solid surfaces due to the difference of the location of the solid surface and the nodes inside the solid, closest to the surface, which are representing the surface in the calculation. See figure 5.5a for an example. A better approximation can be achieved by using a formulation of the Poisson equation, that takes into account the distance of the surface at the nodes neighboring the solids, a.k.a *near-solid nodes*.

The finite difference formula for the second derivative with uneven spacing can be derived by using Taylor's theorem at $x_0 - \alpha h$ and $x_0 + \beta h$, where $0 < \alpha, \beta \leq 1$:

$$f(x_0 - \alpha h) = f(x_0) - \frac{f'(x_0)}{1!}\alpha h + \frac{f''(x_0)}{2!}(\alpha h)^2 - \frac{f'''(x_0)}{3!}(\alpha h)^3 + \cdots \quad (5.26)$$

$$f(x_0 + \beta h) = f(x_0) + \frac{f'(x_0)}{1!}\beta h + \frac{f''(x_0)}{2!}(\beta h)^2 + \frac{f'''(x_0)}{3!}(\beta h)^3 + \cdots . \quad (5.27)$$

By multiplying the first equation by β and second by α and adding together, the first derivatives cancel and the second derivative becomes

$$f''(x_0) = \frac{\beta f(x_0 + \alpha h) - (\alpha + \beta) f(x_0) + \alpha f(x_0 + \beta h)}{\frac{1}{2}(\alpha + \beta)\alpha\beta h^2} + O(h). \quad (5.28)$$

The third derivative terms do not cancel, which makes this finite difference formula only $O(h)$ approximation for the second derivative. Using this formula for approximating the second derivative in the Poisson equation at the near-solid nodes, where αh and βh are the distances to the neighboring nodes or surfaces, a much better surface approximation is achieved compared to the case of standard finite difference discretization of Poisson. A comparison of potential distributions acquired with these two methods is shown in figure 5.5.

The use of the Poisson with uneven spacing is not the only solution for better potential distribution close to surfaces. Another possibility is the use of virtual potential on the nodes inside the solid to adjust the interpolated potential on the surface location. In one dimension, the potential of the node inside the solid ϕ_i is given by

$$\phi_{\text{electrode}} = \alpha\phi_i + (1 - \alpha)\phi_{i+1}, \quad (5.29)$$

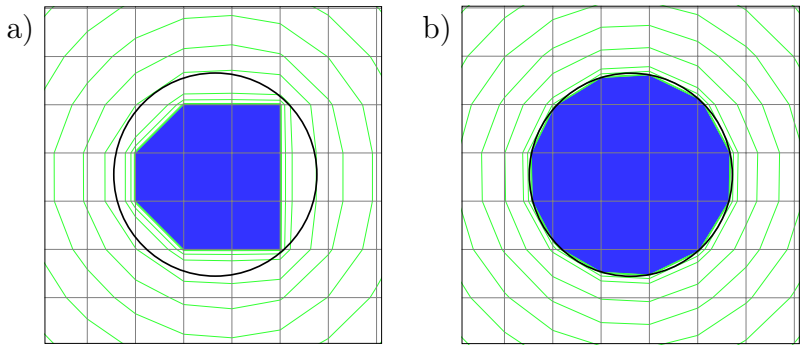

Figure 5.5: Distribution of potential (represented by green equipotential lines) around the circular central solid in a coaxial electrode system calculated with a) the simple Dirichlet boundary condition fixing the potential of the nodes inside the solid and b) Poisson equation taking in account the node distance from the surface at the near-solid nodes. The center of the coaxial system is intentionally chosen not to coincide with the grid. The surface of the intended central solid is drawn as a black circle.

where $\phi_{\text{electrode}}$ is the potential of the electrode, ϕ_{i+1} is the potential of the node outside the solid, and αh is the distance of the node from the surface. This formulation gives similar results to (5.28) in one dimension, but difficulties arise in higher dimensions. Because the adjustment of the potential of the inside node is dependent on the distance and the potential of the outside node, the dependence can only be fulfilled for one pair of nodes. In 2D and 3D geometries the inside node may have closest neighbours in several directions. Therefore only a partial improvement may be achieved compared to what can be done with the use of eq. (5.28). It is also possible to construct finite difference formulas for completely irregular grids, which would enable high quality potential distribution close to the surfaces if the grid is made conformal as is done in reference [133] for example, but such formulation would not have the advantages of the structured grid and as with FEM the grid generation becomes an issue.

5.3.3 Geometry definition

The geometry definition in the developed code is based on an interface for querying inclusion of arbitrary points. First, inclusion is tested at each grid node to classify the node either as a *solid node* or *vacuum node*. Then at the near-solid nodes the distance of the solid surface is found with bisection algorithm. A triangulated surface representation of the solids is built based on this data using the marching cubes algorithm [134, 135] for particle collision detection and visualisation purposes. This geometry data is stored as it is needed by the field solver and other parts of the code.

The code presently contains three different implementations for representing geometric solids. The most simple one is based on use of user defined C-functions, which provide

the inclusion information. Typically mathematical formulation is used in the functions to define the solids. Then there are two implementations, which are based on CAD file formats. One uses 2D DXF files, which can be extruded or rotated to make 3D solids and the other uses stereo lithography (STL) CAD files for three-dimensional geometries. The 3D inclusion algorithm is from reference [136].

5.4 Field solver

The computation domain consists of $I \times J \times K$ nodes. Some of these, for example the Dirichlet nodes, have a constant, prescribed potential. The potential in the remaining N_{dof} nodes is dependent on other nodes through the finite difference formulas (e.g. (5.21) and (5.25)) and therefore have to be solved together as a system of N_{dof} equations, where N_{dof} is the number of the degrees of freedom. In the linear cases (no-plasma problems and Laplace solution for initial potential guess in plasma problems) the N_{dof} equations can be arranged as a matrix equation

$$A\phi = b, \tag{5.30}$$

where A is the problem matrix and b is the right-hand-side vector. For a small 1D Poisson problem for example with Neumann boundary condition on the $i = 0$ boundary and Dirichlet boundary condition on the $i = 6$ boundary, the matrix equation becomes

$$\begin{pmatrix} -2 & 2 & 0 & 0 & 0 & 0 \\ 1 & -2 & 1 & 0 & 0 & 0 \\ 0 & 1 & -2 & 1 & 0 & 0 \\ 0 & 0 & 1 & -2 & 1 & 0 \\ 0 & 0 & 0 & 1 & -2 & 1 \\ 0 & 0 & 0 & 0 & 1 & -2 \end{pmatrix} \cdot \begin{pmatrix} \phi_0 \\ \phi_1 \\ \phi_2 \\ \phi_3 \\ \phi_4 \\ \phi_5 \end{pmatrix} = \begin{pmatrix} -h^2 \frac{\rho_0}{\epsilon_0} + 2hf_N \\ -h^2 \frac{\rho_1}{\epsilon_0} \\ -h^2 \frac{\rho_2}{\epsilon_0} \\ -h^2 \frac{\rho_3}{\epsilon_0} \\ -h^2 \frac{\rho_4}{\epsilon_0} \\ -h^2 \frac{\rho_5}{\epsilon_0} - \phi_6 \end{pmatrix}. \tag{5.31}$$

In the case of plasma modelling, where the space charge density at each node is a sum of space charge from the particle ray tracing ρ_{rt} and the space charge of the compensating plasma particles $\rho_{\mathrm{pl}}(\phi)$, which is a non-linear function of potential. In these cases the problem has to be formulated differently. Typically non-linear systems of equations are written as

$$F(\phi) = 0, \tag{5.32}$$

where F is a vector of functions. For a vacuum node in a 1D system, for example,

$$F_i(\phi) = \phi_{i-1} - 2\phi_i + \phi_{i+1} + \frac{h^2}{\epsilon_0}\big(\rho_{\mathrm{rt}} + \rho_{\mathrm{pl}}(\phi_i)\big) = 0. \tag{5.33}$$

For typical 3D extraction systems, the N_{dof} is between 10^5 and 10^8, which places limits on the applicable methods, which can be used for solving the electric potential.

Also many of the solution methods have limitations on what type of problem matrices they can work on. Therefore it is relevant to point out certain characteristics of the matrix. First, the problem matrix resulting from the formulation used here is not symmetric (and therefore not symmetric positive definite) due to the edge smoothing and Neumann boundaries, i.e. (5.28) and (5.25). Secondly, the matrix A is diagonally dominant, which means that

$$|A_{ii}| \geq \sum_{j \neq i} |A_{ij}|. \tag{5.34}$$

These characteristics have been used to select the applicable solution methods for the problem. Because no information was available on the efficiency of the different solution methods for this type of problem, some research was necessary in form of testing different solvers. The following sections introduce the methods, which have been implemented for solving the potential.

5.4.1 Jacobi, Gauss-Seidel and successive over-relaxation

The simplest method for solving the linear Poisson equation is the *Jacobi method* in which the potential of each node i is iteratively updated according to the equation i from (5.30):

$$\phi_i^k = (b_i - \sum_{j \neq i} A_{ij}\, \phi_j^{k-1})/A_{ii}, \tag{5.35}$$

where iteration round is indicated with index k. The nodes are sequentially updated, or *relaxed* from node 0 to N_{dof} until convergence is reached. In this method the potentials for iteration round k depend only on the potentials from the previous round. Therefore both ϕ^k and ϕ^{k-1} need to be stored simultaneously. The *Gauss-Seidel method* is similar, but it uses the updated potential values as soon as they are available

$$\phi_i^k = (b_i - \sum_{j<i} A_{ij}\, \phi_j^k - \sum_{j>i} A_{ij}\, \phi_j^{k-1})/A_{ii} \tag{5.36}$$

and therefore there is no need for additional storage. The Gauss-Seidel also converges faster than Jacobi method with standard (sequential) ordering of nodes. The *successive over-relaxation* or SOR method applies extrapolation to the Gauss-Seidel method to accelerate convergence. This extrapolation uses the previous potential value ϕ_i^{k-1} and the newly computed potential $\bar{\phi}_i^k$ from (5.36) and sets the node potential

$$\phi_i^k = \omega \bar{\phi}_i^k + (1-\omega)\phi_o^{k-1}, \tag{5.37}$$

where ω is the relaxation factor, between 0 and 2. The values $\omega > 1$ result in over-relaxation (acceleration) and values $\omega < 1$ in under-relaxation (damping). The case $\omega = 1$ is the Gauss-Seidel method. With $\omega \leq 0$ and $\omega \geq 2$ the method generally fails to converge. The relaxation factor used is typically chosen experimentally for the

type of problem as no general methods exist for computing the optimal factor. In the formulation used in this work it has been found that the optimal ω gets closer to 2 as the problem discretization becomes finer. [137, 138]

These methods are known as stationary iterative methods, as the solution ϕ is a stationary (or fixed) point of the iteration function g: $g(\phi) = \phi$. The stationary methods generally converge for symmetric positive definite or diagonally dominant matrices. The formulation used is therefore convergent. The solid smoothing algorithm based on equation (5.29) does not generally fulfill either of the convergence criterion and convergence problems were experienced in some cases when this smoothing method was tried.

The nonlinear case can be solved similarly, by reformulating the equations (5.32) in the fixed-point form. The most common formulation is the Newton-Raphson method, which for a 1D problem is $x_{n+1} = x_n - g(x_n)/g'(x_n)$. Here the Newton-Raphson method is applied for one node at time and the fixed-point iteration formula for (5.33) becomes

$$\phi_i = \phi_i + \left(\phi_{i-1} - 2\phi_i + \phi_{i+1} + h^2 \frac{\rho_{\mathrm{rt}} + \rho_{\mathrm{pl}}(\phi_i)}{\epsilon_0}\right) / \left(2 - \frac{h^2}{\epsilon_0} \frac{\partial \rho_{\mathrm{pl}}}{\partial \phi}(\phi_i)\right). \qquad (5.38)$$

The global iteration is still made as in Gauss-Seidel, by sequentially updating the nodes. The convergence criterion given above does not hold for this system of coupled one-dimensional non-linear iterations. Generally for the Newton-Raphson it is said that the iteration converges if the initial guess is sufficiently close to the solution. This seems to hold in this case and care must be taken to give a sufficiently good initial guess. A thorough analysis of the convergence of such systems is given, for example, in [139].

In this work the stationary solver methods are implemented as highly integrated module in the solver code. The matrix form of the problem as shown in eq. (5.31) is never constructed, but the solution is done using the iterative formulae above and the information of the computation domain and geometry. This keeps the memory consumption of the methods low. The problem with the stationary methods is that, in general, they are not very fast to converge.

5.4.2 Direct matrix solvers

The linear matrix problem can also be solved using a direct, non-iterative approach. The most commonly used such approach for asymmetric systems is the LU factorization, where the matrix is factored as a product of lower and upper triangular matrices. The main difficulty in this approach is the large amount of added non-zero elements or *fill-in* in the LU matrix compared to A, which leads to high memory consumption and long computation times. The amount of fill-in elements is usually minimized by

these solvers by permutation of A. These solvers are very fast as long as the factorized matrix fits in the computer memory. Unfortunately this is not the case in most 3D simulations. For 2D systems the amount of fill-in is lower due to lower number of connections per node and therefore the direct approach is often applicable.

A direct LU factorization solver UMFPACK [140] has been integrated in the simulation code. The electrostatics problem is first formulated as right-hand-side vector and sparse matrix of coefficients in the Compressed Column Storage (CCS) form, where only the non-zero elements of the matrix are stored. The matrix form problem is solved by an external computer library. The nonlinear case, eq. (5.32), is solved using globally convergent N-dimensional Newton-Raphson iteration, where the proposed potential step $\Delta\phi$ is solved with UMFPACK from the linear problem

$$J(\phi^{k-1})\Delta\phi = -F(\phi^{k-1}), \tag{5.39}$$

where the Jacobian matrix J consists of elements $J_{ij} = \partial F_i/\partial\phi_j$. The potential in the iteration is updated with

$$\phi^k = \phi^{k-1} + \alpha\Delta\phi, \tag{5.40}$$

where $\alpha \leq 1$ is chosen such that norm of the new residual $||F(\phi^k)||$ is smaller than the previous $||F(\phi^{k-1})||$. This modification of the regular Newton-Raphson iteration avoids the overshoot, which causes convergence problems due to the exponential form of ρ_{pl}.

5.4.3 Preconditioned biconjugate gradient stabilized method

Another family of iterative methods is the *nonstationary methods*, which differ from stationary methods in that the computations involve variables, that change at each iteration. Of these methods, the preconditioned biconjugate gradient stabilized method (BiCGSTAB) [141] is one of the most robust and efficient solvers for nonsymmetric linear problems. The BiCGSTAB method, like all conjugate gradient methods, is based only on basic vector and matrix algebra operations. The BiCGSTAB method has been implemented in this work from [138]. The BiCGSTAB solves the problem in Compressed Row Storage (CRS) sparse matrix form.

The convergence rate of the nonstationary methods depend heavily on the spectral properties of the matrix. Therefore it is often beneficial to transform the linear system into a system with more favorable properties. The preconditioner matrix M, which approximates the coefficient matrix A can be used to transform the system to

$$M^{-1}A\phi = M^{-1}b, \tag{5.41}$$

which has the same solution as the original system, but the spectral properties of $M^{-1}A$ are often better. The use of preconditioner matrix is computationally efficient

if calculation of M^{-1} is easy. Typical preconditioner matrices include diagonal matrix, where M consists of the diagonal of A and has zero elements off-diagonal. Another category of preconditioners are the incomplete factorizations. These are for example incomplete LU factorizations, where the standard LU factorization is somehow altered to limit the number of non-zeros in the matrix M. Two such methods were implemented in this work: ILU(0) and ILU(1) factorizations, which are constructed like regular LU-factorization, but in ILU(0) the sparsity pattern of M is limited to the pattern of A and in ILU(1) only the first level fill-in is allowed in M (non-zero elements produced by direct products of non-zero elements from matrix A). Choosing a preconditioner to use with a conjugate gradient method is an important part of the optimization: While the computational complexity of preparing the preconditioner becomes higher and the memory consumption increases with more accurate preconditioner matrices, the number of BiCGSTAB iterations needed for convergence decreases. The optimal preconditioner can be found experimentally. Results for testing of different preconditioners by solving spherical capacitor problem is presented in table 5.1. Due to the small speed advantage and higher memory consumption, the ILU(0) is chosen as the standard preconditioner for BiCGSTAB in this work.

Table 5.1: The iteration count, CPU time use and memory consumption for BiCGSTAB solver using no preconditioner, diagonal, ILU(0) and ILU(1) preconditioners when solving spherical capacitor problem with 10^5, 10^6 or 10^7 degrees-of-freedom until relative error norm is less than 10^{-4}. The timing includes the construction of the preconditioner matrix.

N_{dof}	10^5			10^6			10^7		
Precond.	Iter	Time (s)	Mem. (MB)	Iter	Time (s)	Mem. (MB)	Iter	Time (s)	Mem. (MB)
–	439	1.51	30	1733	59.3	250	4170	1568.28	2404
Diag	74	0.29	31	174	6.30	258	365	160.19	2467
ILU(0)	26	0.20	39	59	4.15	337	121	105.78	3256
ILU(1)	23	0.22	46	41	3.57	407	83	92.23	3941

The BiCGSTAB method can also be used to solve nonlinear problems using N-dimensional Newton-Raphson iteration identically to what was described for the UMFPACK solver above.

5.4.4 Multigrid method

The stationary iterative methods have different convergence rates for long wavelength and short wavelength components. The relaxation smooths out the short wavelength errors quickly, but the global convergence of the problem is slow. The *multigrid* (MG) method uses stationary methods to smoothen the error and a hierar-

chy of discretization levels to make corrections in the finest level problem by solving coarser problems [142]. In this work the MG method has been implemented for solving the linear Poisson according to the following scheme: A hierarchy of M grids with geometry information is generated with grid on level l having size $(I_l, J_l, K_l) = (2I_{l+1} - 1,\ 2J_{l+1} - 1,\ 2K_{l+1} - 1)$, where level $l = 0$ is the finest level (see figure 5.6 for a 1D example). The problem $A\phi = b$ is relaxed with N_{pre} iterations on the finest level, which smoothes the residual $r = A\phi - b$. The residual is restricted to the next coarser level, where a correction is calculated from $A\Delta\phi = r$ by recursion (by using even coarser grid levels). On the coarsest level the correction equation is solved exactly with SOR. After having an estimate of a correction at each level, it is prolonged to the next finer level and applied there with $\phi^{k+1} = \phi^k + \Delta\phi$. The new estimate is then relaxed again with N_{post} iterations to remove the short wavelength errors induced by the coarser grid. The corrections are propagated this way back to the finest level, which finishes the MG cycle. The cycles are repeated until convergence is achieved with the finest level solution.

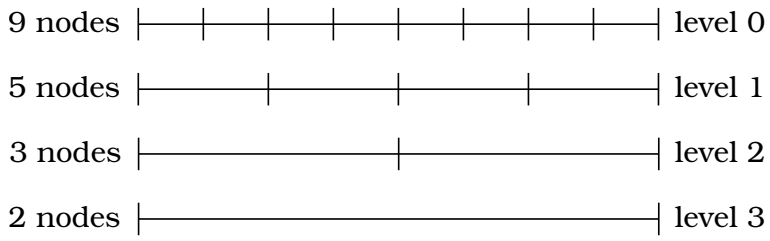

Figure 5.6: Four levels deep hierarchy of 1D grids for multigrid.

The simplest MG cycling strategy is to start with the finest level and proceed by restriction to the coarsest level and after exact solution return the correction with prolongation to the finest level. This type of cycles are known as V-cycles (see figure 5.7). The accuracy of the correction $\Delta\phi$ provided by each MG cycle can be improved by making an additional refining cycle on each level between the coarsest and finest levels. These W-cycles provide higher accuracy corrections than V-cycles with only minor additional computation.

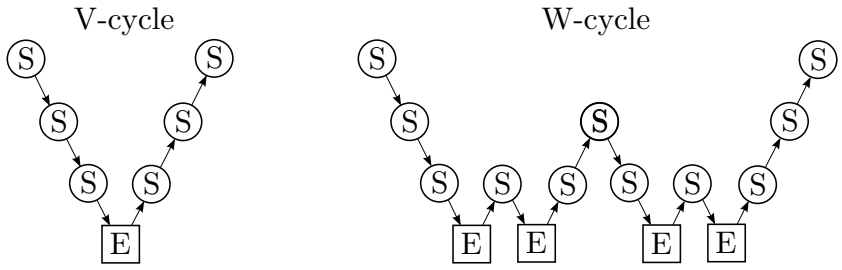

Figure 5.7: Structure of V and W-cycles in a four level hierarchy. The smoothing operation is presented by S and exact solution at the coarsest level by E.

The implementation made here uses Red-Black Gauss-Seidel [137] as a smoothening method. The Red-Black Gauss-Seidel relaxes the potential like Gauss-Seidel, but the cycle is divided into two subcycles: on the first subcycle the nodes for which $i+j+k$ is even are relaxed and on the second subcycle the nodes for which $i+j+k$ is odd are relaxed. In this way every node is equal and the ordering of the nodes has no effect on the result. As a stand-alone solver, the Red-Black Gauss-Seidel is slower than Gauss-Seidel, but as a MG smoother it is the most efficient choice [137]. The number of relaxation cycles made in the MG have been found optimal at $N_{\text{pre}} = N_{\text{post}} = 5$ for the systems solved. For the non-linear Poisson equation a Full Approximation Scheme (FAS) version of the multigrid method is used, where the solution ϕ is restricted to the coarser levels with the residual to enable the nonlinear relaxation. The problem formulation is embedded in the MG solver. Therefore, the matrix form of the problem is not constructed which help to keep the memory consumption low.

5.4.5 Convergence and benchmarking

The iterative methods need a way for estimating the deviation of the iterate ϕ from the exact solution ϕ^* for deciding when the solution is close enough to justify stopping the iteration. The standard way of doing this is by using the residual $r = A\phi - b$ to estimate the error. The relation of r to the error can be derived eliminating b from the residual equation, which gives $\phi - \phi^* = A^{-1}r$. The relative error norm can therefore be estimated as

$$\frac{||\phi - \phi^*||}{||\phi^*||} \leq \frac{||A^{-1}||\ ||r||}{||\phi^*||}, \tag{5.42}$$

which is somewhat inconvenient to evaluate due to the dependency on $||\phi^*||$. That is eliminated with $||b|| = ||A\phi^*|| \leq ||A||\ ||\phi^*||$, which gives

$$\frac{||\phi - \phi^*||}{||\phi^*||} \leq ||A^{-1}||\ ||A||\ \frac{||r||}{||b||}. \tag{5.43}$$

Here, the condition number of a matrix is defined as $\kappa(A) = ||A^{-1}||\ ||A||$. Many iterators use $||r||/||b|| < \epsilon_{\text{Poisson}}$ as a convergence criterion, which is not recommendable due to the possible dependence of $\kappa(A)$ on h, which according to [143] may be highly dependent on the type of formulation used. Therefore, a numerical experiment approach has been taken to form an error estimator.

Three test problems have been used in this chapter. Two of the problems are linear electrostatic problems with known analytic solutions: spherical and cylindrical capacitors. The positive octant of a spherical capacitor centered at the origin has been used in 3D with Neumann boundary conditions on the $x_{\min}$, $y_{\min}$ and $z_{\min}$ boundaries. Similarly the positive quadrant of the cylindrical capacitor has been used in 2D with Neumann boundary conditions on the $x_{\min}$ and $y_{\min}$ boundaries (see figure 5.8). The

third test problem is a 3D plasma extraction geometry developed for the JYFL RF H^- ion source RADIS (presented in detail in section 6.4).

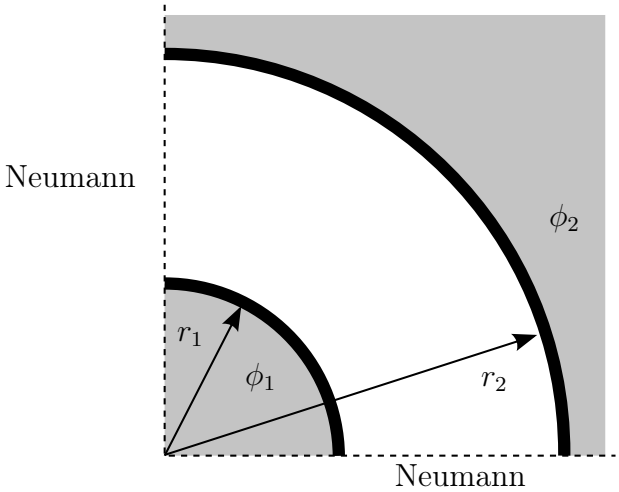

Figure 5.8: The spherical and cylindrical capacitor test problems with $\phi_1 = 0$ V, $\phi_2 = 10$ V, $r_1 = 2$ cm, $r_2 = 7$ cm.

In the numerical experiments the test problems have first been solved with sufficient accuracy that the use of the solution as ϕ^* is justified. Then the problem is solved again, while evaluating the residual norm divided by the right-hand-side $||r||/||b||$, the relative error norm $||\phi - \phi^*||/||\phi^*||$ and relative error norm calculated relative to the analytical solution of the problem at each iteration round. The data for the spherical capacitor problem with BiCGSTAB-ILU(0) method is shown in figure 5.9 as an example. From this kind of data using the problems, it has been observed that the error estimation of the conjugate gradient methods can be done with (5.43), by using $\kappa(A) = \max(I, J, K)^{-2}$. In the tested cases this gives a good approximation of the error. The condition number scaling is approximate as the geometry of the problem of course affects the scaling (vacuum might not cover the full volume of the problem for example).

With Gauss-Seidel, SOR and MG methods, the use of residual vector for error estimation is not computationally effective, because it is not readily available as in the conjugate gradient methods. What is easily available is the potential change $\Delta\phi$ at each node. According to the numerical experiments, the relative error norm $||\phi - \phi^*||/||\phi^*||$ in Gauss-Seidel and SOR can be estimated with $G_{2\mathrm{D}}(\omega)\ ||\Delta\phi|| \max(I, J, K)$ in 2D and with $G_{3\mathrm{D}}(\omega)\ ||\Delta\phi|| \max(I, J, K)^{1/2}$ in 3D, where the $G_i(\omega)$ are third order polynomial fits to data from test problems. With MG, the error estimator is $||\Delta\phi|| A \max(I, J, K)^B$, where A and B are fitted coefficients for 2D and 3D separately. As with the conjugate gradient error estimator, these error estimators give too large estimates during the first iterations, but this does not prevent the use as a stopping criterion.

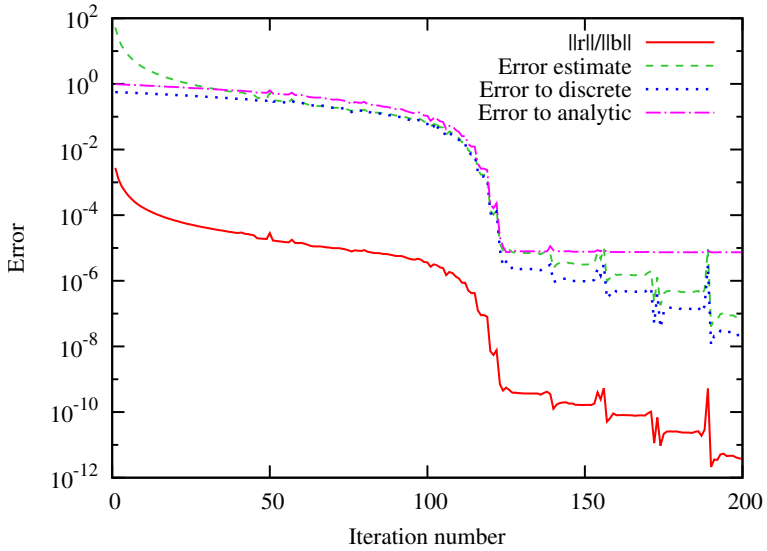

Figure 5.9: The convergence of the BiCGSTAB-ILU(0) method with $308 \times 308 \times 308$ node spherical capacitor problem. After about iteration number 120 the error of the solution compared to the analytic solution is limited by the discretization error.

The ultimate accuracy of the solution relative to the physical (analytic) solution is limited by the approximations made in the discretization of the Poisson equation. The approximation quality improves as mesh density increases. The relative error norm of the spherical capacitor problem is shown in figure 5.10 as a function of resolution for the cases where edge smoothing has been used and for the case with no edge smoothing.

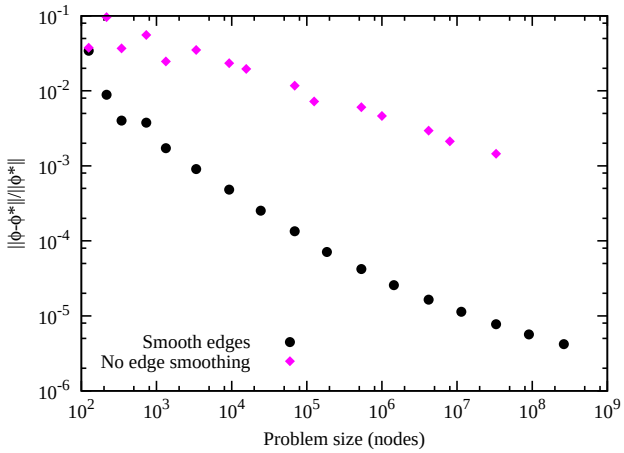

Figure 5.10: The error norm of the calculated potential relative to the analytic potential in the spherical capacitor as a function of resolution for both smooth and jagged edges.

The different solvers have been benchmarked by solving linear test problems, cylindrical capacitor in 2D and spherical capacitor in 3D, until an accuracy of 10^{-4} is reached according to the error estimator, while the use of computational resources has been observed. The tests have been done on a Intel Core i7–3770 3.40 GHz computer with 16 GB of memory. The results are shown in figures 5.11 and 5.12.

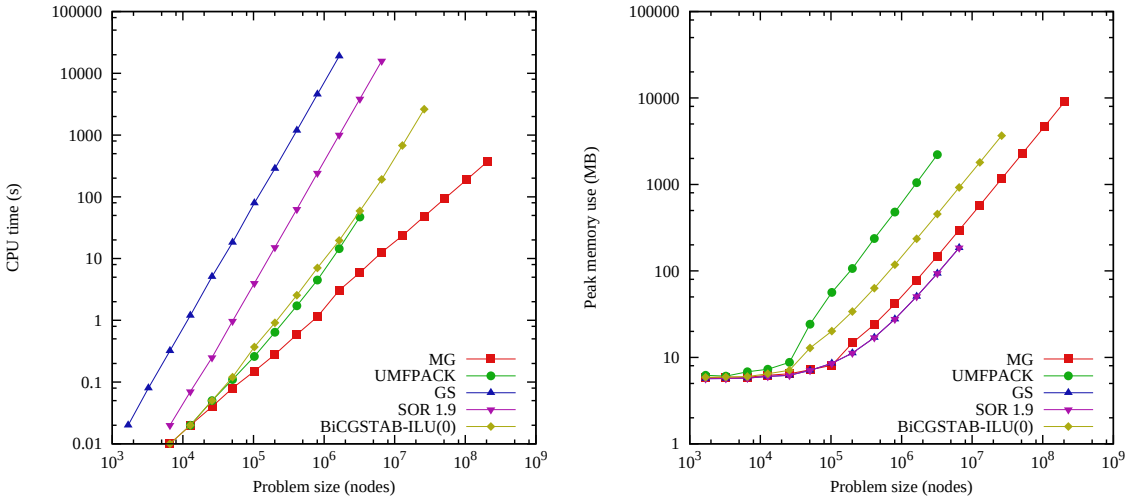

Figure 5.11: The use of CPU time and memory when solving a 2D test problem with different solvers.

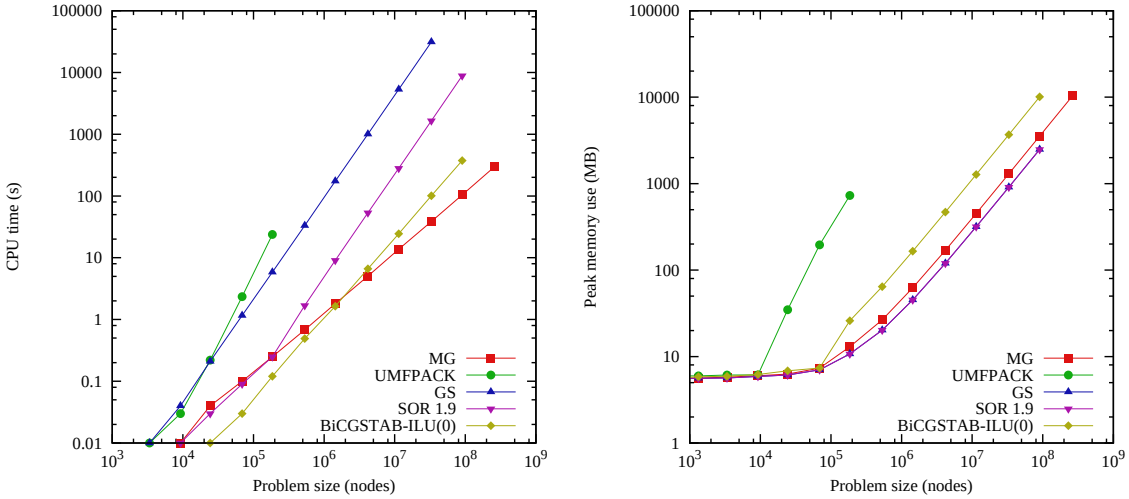

Figure 5.12: The use of CPU time and memory when solving a 3D test problem with different solvers.

In 2D the typical problem sizes are between 10^4 and 10^7, which means that the Poisson solution is achieved in less than 10 seconds with the fastest methods. In 3D the typical problem size used is between 10^6 and 10^8 and is often limited by available memory. The solution in 3D can often take hundreds of seconds.

The convergence of the iterative non-linear solvers is evaluated exactly as with the linear counterparts in case of Gauss-Seidel, SOR and MG methods. In case of BiCGSTAB-ILU(0) and UMFPACK methods, it has been observed that a good error estimate is achieved with $||r||$ A $\max(I, J, K)$, where $r = -F(\phi^k)$ is the residual vector from the last iteration round (see eq. (5.39)) and A is a fitted coefficient. The nonlinear solvers have been benchmarked using the third test problem, the plasma-electrode puller-electrode region of the JYFL RADIS H^- extraction system. The test problem was prepared by first solving the potential using a linear solver (of the same type) with an initial guess of the plasma sheath location. Using the electric field calculated from the potential map, trajectories of the particles extracted from the plasma were calculated and space charge density map ρ was formed. The nonlinear solver was then used to calculate the potential of the nonlinear plasma system, until an accuracy of 10^{-4} is reached according to the error estimator, while the use of computational resources was observed. The electric potential from the linear problem was given to the solvers as an initial guess. The results are shown in figure 5.13.

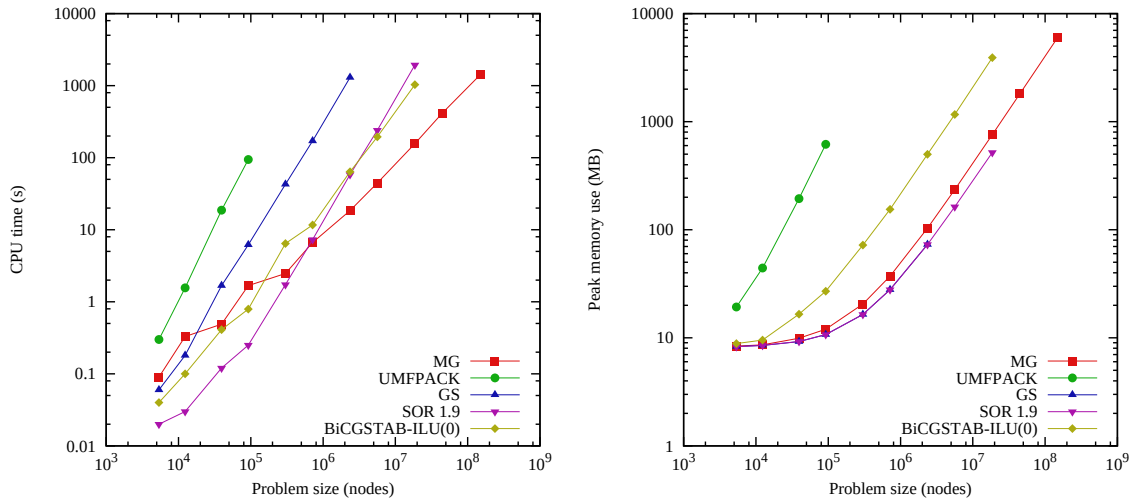

Figure 5.13: The use of CPU time and memory when solving a nonlinear 3D test problem with different solvers.

The MG solver is obviously the method of choice in 2D and 3D geometries both with linear and nonlinear problems: the convergence with large systems is fastest and memory consumption is low. Only Gauss-Seidel and SOR solvers have lower memory consumption, but they are too slow for any practical work with large systems. The MG solver is not unconditionally the best as it requires a mesh size, which can be divided into a hierarchy of grid levels. In the linear test cases above the geometry had size ratios of 1:1 in 2D and 1:1:1 in 3D, which allow freely selectable grid size, but in systems where exactly a certain size ratio is required the efficiency of the MG solver may deteriorate. With practical work this is almost never encountered. With the nonlinear test problem the grids were based on two bases: $21 \times 16 \times 16$ and $28 \times 21 \times 21$.

The first basis produces grids $21 \times 16 \times 16$ (1 level MG), $41 \times 31 \times 31$ (2 level MG), $81 \times 61 \times 61$ (3 level MG), etc. and the second one produces grids $28 \times 21 \times 21$ (1 level MG), $55 \times 41 \times 41$ (2 level MG), $109 \times 81 \times 81$ (3 level MG), etc. The same grids were used for all solvers.

5.5 Electric field evaluation

In the electrostatic case, the electric field is completely defined by the electrostatic potential:

$$\vec{E} = -\vec{\nabla}\phi \tag{5.44}$$

The central finite difference formula gives the following expressions for the electric field components:

$$E^x_{i+\frac{1}{2},j,k} = \frac{\phi_{i,j,k} - \phi_{i+1,j,k}}{h} + O(h^2) \tag{5.45}$$

$$E^y_{i,j+\frac{1}{2},k} = \frac{\phi_{i,j,k} - \phi_{i,j+1,k}}{h} + O(h^2) \tag{5.46}$$

$$E^z_{i,j,k+\frac{1}{2}} = \frac{\phi_{i,j,k} - \phi_{i,j,k+1}}{h} + O(h^2), \tag{5.47}$$

where the electric field is given on the grid line halfway between the grid nodes at which the electrostatic potential is defined. This is done in such a way to minimize the amount of error induced in the electric field, even though it induces further complication as the electric field components are defined on grids offset by $\frac{h}{2}$ from the primary grid.

Another complication in evaluating the electric field results from the solid surfaces. To fully take advantage of the knowledge of the surface distance from the near-solid nodes, the electric field between the near-solid node (i, j, k) and the solid node $(i + 1, j, k)$ for example, is calculated with

$$E^x_{i+\frac{1}{2},j,k} = \frac{\phi_{i,j,k} - \phi_{i+1,j,k}}{\alpha h} + O(h), \tag{5.48}$$

where αh is the distance from the near-solid node to the surface. This computation makes an error in the location of the field: the solid potential is defined at the surface location $(i+\alpha, j, k)$ and therefore, if the central difference formula was used correctly, the electric field would be defined at $(i + \frac{\alpha}{2}, j, k)$ and not at $(i + \frac{1}{2}, j, k)$. Using this location information would cause further difficulties in interpolating the electric field between the nodes and therefore it is chosen not to use the central difference near the solids. Instead the eq. (5.48) is used, which makes the evaluation only $O(h)$ accurate.

The electric field value $\vec{E}(x, y, z)$ needed by the particle trajectory calculation at arbitrary locations in the simulation domain is calculated by (bi/tri)linear interpolation

from the electric field values at the offset grid nodes. Because of the interpolation, an electric field value on the offset grid, which is calculated from two potential nodes inside a solid, may have an influence on the interpolated electric field value outside the solid. To prevent this the field evaluator is made to use the electric field on the near-by surface at these grid points (see figure 5.14).

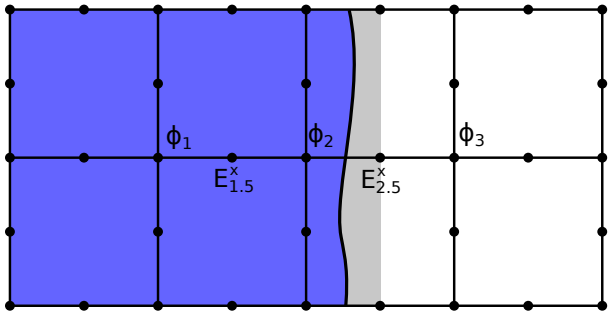

Figure 5.14: The electric field interpolation uses the $E^x_{1.5}$ value for evaluating $\vec{E}$ between $i = 1.5$ and $i = 2.5$ nodes (the light gray area). For this reason the $E^x_{1.5}$ is not calculated from ϕ_1 and ϕ_2 (would be zero), but it is made to have the same value as $E^x_{2.5}$ for achieving constant E_x in this area. This surface electric field correction is not done if it can not be made unambiguously as is the case with thin solids.

5.6 Particle trajectory calculation

The particle trajectories in the code are calculated with the particle iterator using electric field data described above and magnetic field defined on an independent mesh. The magnetic field can be defined using data from external software on a regular grid independent of the electric potential grid.

Each *macro particle* in the code represents an ensemble of several real particles. Each calculated particle has a charge q (C) and mass m (kg) equal to the real particle it represents, but in addition it has a current I (A). At each iteration point the particle has a location $\vec{r}$ (m) and velocity $\vec{v}$ (m/s).

5.6.1 Beam definition

The particle beams in the simulations can be defined using several methods. The particles may be defined (1) as beams with given α, β and ϵ in the transverse directions and Gaussian or KV distributions or (2) as uniform beams with cylindrical or rectangular cross sections and given parallel and transverse Gaussian distributions or (3) as individual particles with given properties for each of them. The particle location and

velocity distributions of the defined beams are based on quasi-random numbers from the Sobol sequence [144]. The quasi-random numbers are distributed quite evenly in N-dimensional space, whereas regular random numbers typically have more roughness in the distribution. Another possibility to define the particle distributions is the use of ordered definition, for example for Gaussian distribution by having particles emitted to fixed angles from each point of emission [106, 145]. This type of definition is used in several codes, but it was not chosen here because it poses an artificial maximum angle on the Gaussian distribution, for example. By using the random-number based distributions the quality of the distribution depends only on the number of particle trajectories per grid cell n_p. For beams with well-defined cross-sectional area A, the current of each computational particle trajectory is calculated as $I = J\,A/N$, where J is the beam current density and N is the total number of macro particles in the beam. For other beams the total current of the beam is specified. For a typical plasma extraction problem the beams are defined on a plane inside the ion source plasma with a uniform current density J, constant initial drift energy E_0 and transverse temperature T_t.

5.6.2 Particle iteration

The particle propagation is defined by the Lorentz force, which is used as a system of ordinary differential equations (ODE). For 3D the ODE are

$$\frac{d\vec{r}}{dt} = \vec{v} \tag{5.49}$$

$$\frac{d\vec{v}}{dt} = \vec{a} = \frac{q}{m}(\vec{E} + \vec{v} \times \vec{B}) \tag{5.50}$$

in the non-relativistic approximation, which is used for most of the simulations in this work. In cases where relativistic effects are relevant (typically about $v > c/10$) the relativistic algorithm can be enabled. The relativistic equations of motion of a particle as observed in the laboratory coordinates (where $\vec{E}$ and $\vec{B}$ are defined) arise from

$$\vec{F} = \frac{d\vec{p}}{dt} = \frac{d}{dt}\left(\frac{m\vec{v}}{\sqrt{1 - v^2/c^2}}\right) = q(\vec{E} + \vec{v} \times \vec{B}) \tag{5.51}$$

by dividing with mass and calculating the derivative. This gives

$$\gamma\frac{d\vec{v}}{dt} + \gamma^3\frac{\vec{v}}{c^2}\left(\vec{v} \cdot \frac{d\vec{v}}{dt}\right) = \frac{q}{m}(\vec{E} + \vec{v} \times \vec{B}), \tag{5.52}$$

where $\gamma = 1/\sqrt{1 - v^2/c^2}$ is the relativistic gamma factor. The particle acceleration $d\vec{v}/dt$ is solved from (5.52) and it is used in the system of ODE.

The particles are propagated iteratively by integrating the equations of motion with an embedded Runge-Kutta Cash-Karp method featuring an automatic step-size adjustment to limit the error in the particle trajectories under a prescribed value ϵ_{part}. The implementation of the integrator is from the GNU Scientific Library [146]. Fixed step-size iterators, such as classic leapfrog algorithm [106] were used in early versions of the code, but the development led to adaptive iterators, which are efficient with typical problems where the particle velocities can span over 3 orders of magnitude.

Between successive calculation points, the particle is checked for collisions with solids and computation domain boundaries. This is done by constructing an up to 3rd order polynomial representation of the trajectory as a function of time between the calculation points and checking for intersections between the grid planes and the trajectory. These intersection points are then used to create a piecewise linear representation of the trajectory, where the trajectory consists of a single straight line segment inside each grid cell. This method provides relatively good interpolation of highly non-linear trajectories in cases where calculation points are several mesh cells apart, while enabling the use of simple algorithms requiring (locally) straight trajectories. The collisions with solids, for example, are detected by checking for intersections between the line segment and the surface triangulation of the solids in the grid cell.

5.7 Space charge deposition

The space charge density of the ray-traced particles ρ_{rt} is needed by the Poisson solver at vacuum grid nodes. There are many methods which can be used for assigning the charge on the grid based on the particle trajectories. In this work the charge deposition is based on the method used in the more established PIC codes, where the space charge is assigned to the grid from particles at each time step (in PIC the charge density of a particle is needed, while in Vlasov-Poisson-iteration codes the charge density of a trajectory is of interest). In PIC codes the assignment of the particle charge Q to the grid is made using a weighting function $S(\vec{r})$:

$$\rho_{i,j,k} = QS(\vec{r} - \vec{r}_{i,j,k}). \tag{5.53}$$

The $S(\vec{r})$ can be interpreted as a density function of the finite-size charge cloud that the calculated particle is representing. The most simple choice for the weighting is to deposit all charge to the nearest grid point, but this leads to high numerical noise. Therefore, higher order weighting functions are favored. According to [106] the weighting function having the same shape as the interpolation function used to calculate the electric field acting on the particle should be preferred. In this work the trilinear weighting function is used:

$$S(x,y,z) = \begin{cases} \frac{1}{h^3}(1-|x/h|)\,(1-|y/h|)\,(1-|z/h|) & |x|<h, |y|<h, |z|<h \\ 0 & \text{otherwise.} \end{cases} \tag{5.54}$$

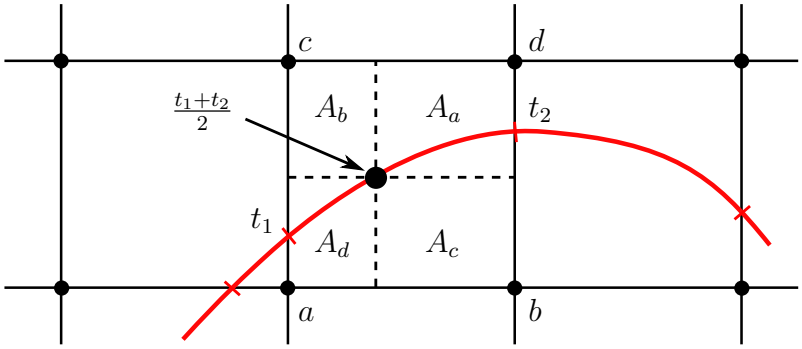

Figure 5.15: The space charge $Q = I\Delta t$ is deposited inside each grid cell assuming that the charge cloud is centered at the location, where the particle was at $t = \frac{1}{2}(t_1 + t_2)$ according to the polynomial trajectory interpolation. In 2D the charge is divided to the cell nodes from this location according to bilinear weighting: the charge to node a is $Q_a = Q\ A_a/h^2$.

The charge deposition of a trajectory in this work is made by utilizing the trajectory-grid plane intersection points constructed during the particle trajectory calculation (see figure 5.15). Inside each grid cell, the trajectory is passing through, an up to 3rd order polynomial representation of the trajectory as a function of time is constructed. Using the polynomial the location $\vec{r}$ is calculated, where the particle was at $t = \frac{1}{2}(t_1 + t_2)$, in which t_1 is the moment when particle entered the cell and t_2 is the moment the particle exited the cell. From the time $\Delta t = t_2 - t_1$ the particle has spent in the cell and the trajectory current I, the amount of charge can be calculated as

$$Q = I\Delta t. \tag{5.55}$$

This charge is deposited to the grid cell nodes according to (5.53) and (5.54) by assuming that the charge cloud Q with shape S is centered at $\vec{r}$. This method gives the correct charge in each cell, but the distribution of the charge is skewed for particles with changing velocity. The amount of error in the charge deposition can be evaluated by comparing to a problem with a known result: A beam is started on a grid plane with kinetic energy E_0 and is under a constant acceleration gaining ΔE energy per grid cell. The space charge density deposited on the next grid plane (where the beam energy has increased to $E_0 + \Delta E$) by the algorithm is compared to the known value. The same analysis is made for a modified algorithm, which deposits the charge cloud at the central location $\frac{1}{2}(\vec{r}_1+\vec{r}_2)$. This algorithm gives inferior ρ quality for accelerating beams (4 times the relative error for low $\Delta E/E_0$). The results of the comparison are shown in figure 5.16.

With low acceleration (or deceleration) the central time algorithm works well overestimating the space charge somewhat, with a maximum of about 1.7 % at $\Delta E/E_0 = 5.5$. In decelerating beams such high ratios are not encountered unless the beam is completely stopped and reflected. At stronger acceleration the relative error decreases

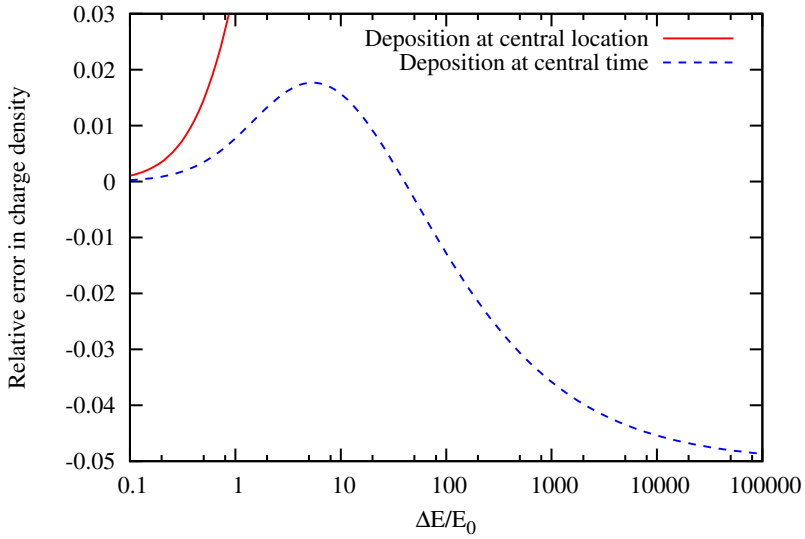

Figure 5.16: A beam is started with kinetic energy E_0 on a grid plane and it is accelerated gaining ΔE energy per grid cell. The relative error of the space charge deposition on the on the next grid plane (where the beam energy is $E_0 + \Delta E$) is plotted as a function of $\Delta E/E_0$ for the two algorithm versions.

and turns negative reaching about -3.5 % at $\Delta E/E_0 = 1000$. In practical simulations the highest $\Delta E/E_0$ are encountered where low energy beams start to be accelerated. In plasma extraction systems the accelerating electric field gradually increases from zero when moving from plasma to extraction. Of all the extraction systems presented in this work, the highest extraction fields are in the proposed new SNS extraction system (presented in section 6.2) and there, with typical mesh size $h = 0.4$ mm the highest $\Delta E/E_0$ is about 20. Therefore it is believed that in the typical cases, with decent mesh sizes, the space charge deposition error is within ± 2 %. The effect of this error on the observables of the whole simulation depends on the significance of space charge in the problem. In the RADIS extraction case, where the highest $\Delta E/E_0$ is about 3.7 the difference in the (x, x') emittance at $z = 130$ mm is 1 % between simulations using central location and central time algorithms. Therefore it is argued that the error of a few percent is not very significant in typical simulations.

In modelling of particle field emission from surfaces for example, the $\Delta E/E_0$ ratios can be of the order of 10^4 or even higher. In these cases, different type of approach should be taken to ensure accurate space charge deposition, for example use of analytic formula for space charge close to the surface if possible.

There are also space charge deposition methods, which give the exact space charge density value also for accelerating beams. One such method calculates the charge density deposited to a grid node with $\rho \propto 1/v$ using the velocity of the particle from the polynomial interpolation at the location where the trajectory is closest to the

node. The weakness of such algorithm is that it can only calculate the space charge deposition correctly from trajectories which have a radius of curvature higher than h. This is not the case in many H^- extraction systems, where the trajectories of the co-extracted electrons may be highly curved in strong magnetic fields.

The methods used here give half of the expected charge density on the computation domain boundary nodes (half on boundary faces, quarter on edges and one-eight on corners) because there is no contribution to the boundary nodes from the outside of the domain. A beam which arrives or exits at a boundary (or goes parallel to the boundary) is expected to continue outside the calculation volume. Therefore the space charge density of the boundary nodes is corrected after contribution from all trajectories is calculated. A similar phenomenon happens at the near-solid nodes as the nodes receive lower charge contribution than a normal vacuum node from the same beam. Unfortunately this is not as easy to correct as the boundary nodes and therefore this inaccuracy is one of the mesh-based artefacts in the simulations. In practical simulations, this effect appears especially close to the plasma electrode aperture, where it might affect the plasma meniscus shape and therefore the whole extraction optics.

5.8 Convergence of the Vlasov-Poisson iteration

The Vlasov-Poisson system is iterated by successively taking the steps described above. Generally the methods tend to take the solution to the correct direction. For example, a too high local space charge causes a potential hump, which deflects trajectories decreasing the space charge on the next iteration round. Still, a proof of the existence or uniqueness of the solution to the discretized system used here is not known to the author despite reasonable effort invested in reviewing literature. Here it is just taken that if the evolution of the observables (diagnostics) becomes small enough, the system is assumed to have converged and that the result is a sufficient approximation of the solution of the Vlasov-Poisson system. The most thorough analysis of the convergence of this type of simulations so far is given in [147], where only positive ion extraction was considered.

5.8.1 Non-convergent systems and cures

With some input parameters it has been observed that the simulations do not show convergent behaviour at all. There are several phenomena causing this non-convergence. One of the requirements for convergence is that the initial guess of the plasma meniscus location has to be somewhat correct. If the initial guess is too far off, the Newton-Raphson based non-linear Poisson solvers fail to converge. Another requirement is that the initial particle velocity has to be high enough (larger than Bohm velocity

in the positive ion extraction case), otherwise the system is non-convergent. Also the simulated geometry needs to have large enough neutralized plasma volume. If the computation domain boundary is too close to the plasma meniscus, it will affect the computation because the potential can not assume its physical form. This typically results in flat equipotential surfaces in the region where meniscus is near the boundary. At least a couple of grid cells of field free plasma should be included to ensure physical solution.

A too low trajectory density in a calculation may lead to a situation where single grid nodes receive significantly higher charge than the surrounding nodes, even from a constant density beam. These peaks in the charge cause potentials, that steer beam away from these nodes on the next iteration round. This creates new locations where beam is bunched, causing the same problem again. With sufficiently large trajectory density, the variation in the space charge is low enough to suppress such strong changes in particle trajectories from iteration to iteration enabling convergence of the system. This instability may also be suppressed by damping the change between iterations. In the simulations here this is done by using under-relaxation on the space charge density from ray-tracing. The space charge used in the Poisson equation is a weighted average of the newly calculated space charge ρ_k^* and the space charge ρ_{k-1} from the last iteration round

$$\rho_k = \alpha\rho_k^* + (1-\alpha)\rho_{k-1}, \tag{5.56}$$

where α is the space charge under-relaxation factor.

Another case, where convergence problems are often encountered, are systems where the current extracted from the plasma is approaching the space charge limited regime. If the space charge density in the beam on some iteration round is over the space charge limit, the beam will be reflected at this location on the next iteration round. The reflected beam will not deposit charge in the following space, which will change the potential distribution allowing the beam to pass again on the following iteration round. The iteration will oscillate between beam passing and beam not passing situations. Also this situation can be avoided by using space charge under-relaxation if the system is not space charge limited. Simulations where beam current emitted from the plasma is higher than the space charge limit will not converge. Therefore the iterative approach used here is not capable of modelling space charge limited emission as such.

5.8.2 Convergence criterion

Several parameters can be used for estimating the convergence. An obvious choice would be to use the norm of the change of space charge or electric potential fields, but this would require storage of the field from previous iteration round for calculating the change. Another possibility is to use results of trajectory diagnostics: beam current, rms emittance, and the Twiss parameters. In this work the evolution of the transverse

rms emittance has been chosen to be used for estimating the convergence. This choice makes sense as the beam emittance is often one of the simulation results that are interesting in typical applications. In this work the simulation convergence is primarily evaluated from rms emittance on the boundary where the beam exits the computation domain. As an example of convergence, the evolution of the (x, x') rms emittance at $z = 130$ mm in the RADIS extraction (see section 6.4) has been stored using different under-relaxation factors α for hundred iteration rounds. The value $|\epsilon - \epsilon^*|/\epsilon^*$ has been plotted in figure 5.17 as a function of iteration round, where ϵ is the rms emittance on the iteration round and ϵ^* is the average rms emittance calculated from iteration rounds 90–99.

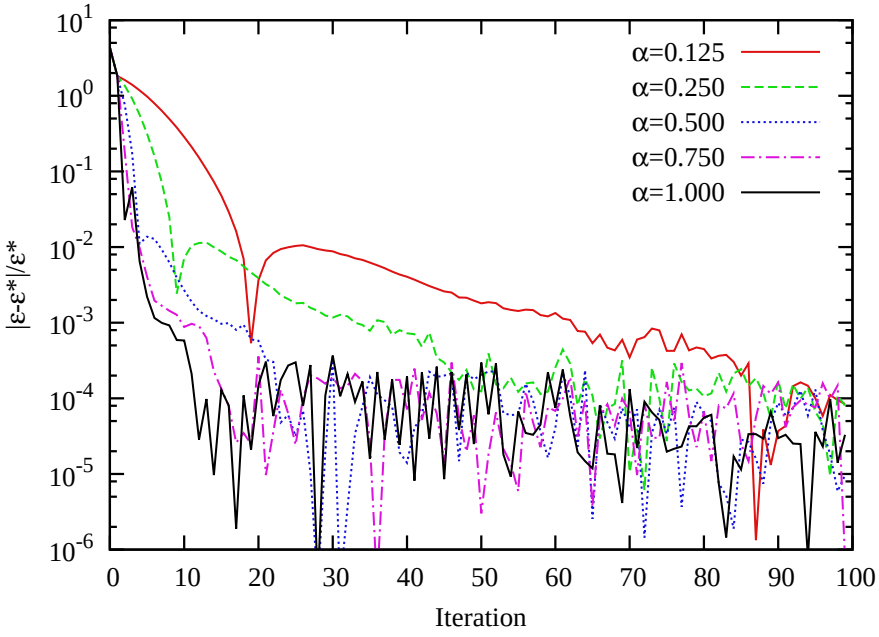

Figure 5.17: Convergence of the emittance in RADIS extraction simulations with $n_p = 200$ trajectories launched per grid cell and grid size $h = 0.5$ mm for different space charge under-relaxation factors α.

The example case presented here is convergent for all $\alpha \leq 1$. For each case, the emittance value evolves and the distance from the final value decreases on average (not necessarily on each iteration) until a residual variation level of about 10^{-4} is reached. The iteration with $\alpha = 0.25$ has converged after about 50 iteration rounds, while the $\alpha = 1$ case has reached the residual variation level after 10 iterations. The number of iterations needed for convergence may depend on the physical parameters of the system such as geometry, electrode potentials and the plasma model parameters, and on technical parameters of the simulation such as trajectory grid density n_p, grid size h and accuracy requirements for Poisson and trajectory solvers in addition to the space charge under-relaxation factor α.

Because the convergence pattern and the residual variation level of the system are dependent on the simulation input parameters the convergence criterion used in the Vlasov-Poisson iteration does not even try to estimate the relative deviation of the emittance from the final value. The stopping criterion for the iteration simply requires that the absolute value of the average of last N emittance change values $\frac{1}{N}\sum_{i=k-N}^{k-1}(\epsilon_{i+1} - \epsilon_i)$ is less than some prescribed ϵ_{Vlasov} for two consecutive iterations. The same convergence criterion parameters N and ϵ_{Vlasov} can be used for all simulations where the convergence rate and residual variation level are roughly constant.

5.9 Validity of simulations

When convergence has been achieved the results of the simulation can be studied. An obvious question of interest, of course, would be the absolute accuracy of the simulation or more specifically the deviation from experiment. Unfortunately this is a very complicated comparison to make as it depends not only on the validity of the approximations made in the plasma model, the correctness of the input parameters, the errors from the discretization, numerical inaccuracies, etc, but also from the approximations and practical limitations of the experiment.

An optimal benchmark for the code would be a comparison to a theoretical solution of a Vlasov-Poisson problem. Unfortunately problems with known theoretical solutions, for example the cases presented in references [148, 149, 88, 150], are based on charged particle beams emitted from a fixed cathode at space charge limited regime, i.e. at zero initial velocity. The developed code does not currently have the specialized functionalities needed for modelling space charge limited emission. Therefore these problems can not be used for benchmarking at this stage. For now, the examination of the validity of simulations is concentrated only on estimating the magnitude of error resulting from computational inaccuracies and artefacts in the discrete Vlasov-Poisson system by varying the computation parameters in problems for which a known solution does not exist.

As has been already seen the Vlasov-Poisson iteration does not converge without limit. Therefore the residual variation level poses a limitation on the accuracy of the results. Another limitation arises from the discretization of the geometry: the discretization of the Poisson equation, deposition of the beam space charge to the grid and evaluation of electric field all have their approximations and therefore impact the accuracy of the results.

5.9.1 Effects of discretization

The most obvious simulation artefacts arise from the discrete nature of the computation domain. In plasma extraction simulations the most important location where mesh-based artefacts affect the beam is at the plasma electrode aperture, especially in grid cells where beam passes within one cell of the plasma electrode surface. There the combined effects of the lower accuracy form of Poisson (based on eq. (5.28)), approximations of the electric field evaluation and the lower space charge density near the surface cause errors in the particle trajectories. In 2D (and cylindrical symmetry) it is possible to have the mesh lines coincide with the solid surface. In that case the errors made by the algorithms are minimal. In the general case, this is not possible because the geometry of interest may contain slanted surfaces for example. In 3D with circular plasma aperture, this inaccuracy always exists. Another important limitation at the plasma extraction is that the discrete potential must be able to represent the smooth transition from the field-free plasma to the extraction taking place in the plasma sheath region. This transition zone has a thickness of some Debye lengths.

The magnitude of the plasma extraction artefacts is studied using the RADIS extraction case in 3D, where the plasma electrode aperture radius r_0 is 3.0 mm and the Debye length $\lambda_D < 0.1$ mm. The number of grid cells in the plasma electrode aperture radius r_0/h was varied from 5 to 25 in 0.1 steps. In figure 5.18 the beam (x, x') rms emittance at $z = 25$ mm has been plotted as a function of h. In this case variations smaller than 10 % are observed with r_0/h smaller than 10 ($h > 0.3$ mm). The variations can be taken as a lower limit of the error estimate for the result. Because the grid induced simulation artefacts cause mainly local errors in the electric field, the effect to particle trajectories is nonlinear. This most probably leads to emittance growth and therefore it can be expected that the emittance value given by simulations with small h (discrete problem approaching continuous) is lower than what the larger h simulations give. This is also seen in the example case, where a second order polynomial was fitted to the data to get an estimate of the asymptotic emittance value at $h \to 0$ (see figure 5.18). By comparing the potentials on the optical axis (far from plasma electrode surfaces) in simulations with different h it can be seen that the potential shape is well modelled even in cases where $h \sim 10\lambda_D$. Therefore it is believed that the effects in the proximity of the surfaces are much more important artefact in the parameter range used here.

Another important artefact is the grid-induced transverse emittance growth in free space. This happens due to several reasons [151]: First, the numerical noise in the space charge field causes small local deviations in the potential, which creates non-linear forces affecting the beam. These non-linear forces cause artificial emittance growth. Second, the beam space charge is deposited to the grid nodes of each cell. This behaviour averages out sharp features in the beam. For example the space charge field generated by a uniform beam does not have sharp boundaries (example in figure

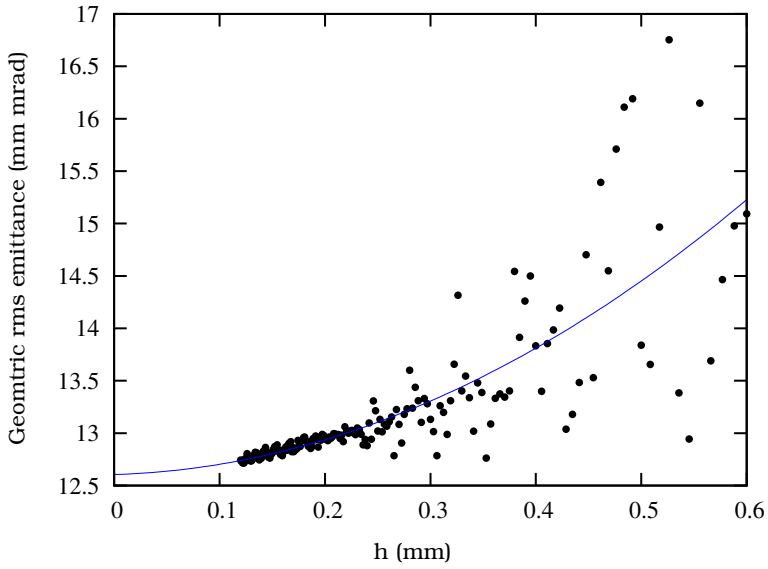

Figure 5.18: The beam transverse rms emittance at $z = 25$ mm as a function of h. The variation of emittance decreases as h decreases.

5.19). Even if the space charge data was ideal, the electric field calculation from the potential and the interpolation of the electric field for the particle iterator cause further averaging to the forces affecting the trajectories. In practice this effect is strongest on the beam boundaries: inside a constant density beam the space charge forces are modelled well, but close to the beam boundary, the smoothing effect causes deviation from the ideal increasing the beam emittance.

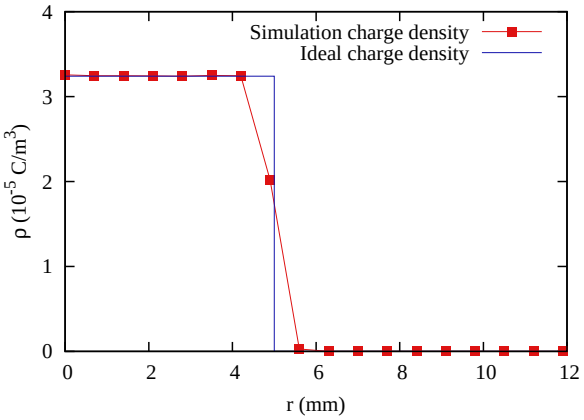

Figure 5.19: The space charge density given by a simulation with $h = 0.7$ mm grid cell size for a uniform 10 mm diameter beam. The space charge deviates from the ideal in grid nodes within h from the beam boundary.

The magnitude of the effect in practical systems has been tested by observing the space charge effects of a parallel zero-emittance 20 keV, 5 mA H^- beam with initial

radius $r_0 = 5$ mm propagating through 200 mm of space in a 15 mm radius beam tube. The beam radius and emittance at the end of the drift space has been measured and is plotted as a function of the simulation resolution (as grid cells in the original beam radius) in figure 5.20. It can be seen that the beam space charge induced divergence is within 2 % of the apparent asymptotic value when r_0/h is over 10 (The beam radius should be 9.1 mm according to the paraxial approximation, see section 4.4.1). The emittance growth of the beam is not very significant as geometric rms emittance of 0.3 mm mrad corresponds to about $1 \cdot 10^{-3}$ eV transverse temperature in this case, which is orders of magnitude lower than beams extracted from plasma typically have.

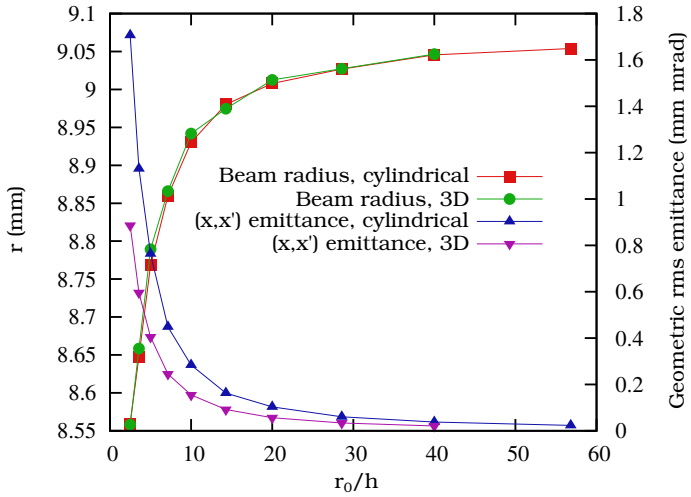

Figure 5.20: The radius and rms (x, x') emittance of beam at the end of the 200 mm drift space using different grid cell sizes h in cylindrically symmetric simulations and in 3D.

5.9.2 Effects of other computational parameters

In addition to the grid cell size h, the simulation has other purely computational parameters which have no physical meaning. These are the space charge under-relaxation factor α, the accuracy requirement for the Poisson solver $\epsilon_{\text{Poisson}}$, the accuracy requirement for the particle iterator ϵ_{part} and the number of particle trajectories per grid cell n_p. The effect of the computational parameters to the transverse rms emittance at $z = 130$ mm was studied using the RADIS extraction while keeping the physical parameters and the grid size $h = 0.5$ mm constant. The Vlasov-Poisson system was iterated for 100 rounds and the standard deviation of the emittance at the end of the geometry was computed from the last 40 rounds to evaluate the level of residual variation.

By adjusting the space charge under-relaxation factor α it was observed that it has no effect on the resulting emittance or the residual variation level as long as the residual

variation level is reached before iteration round 60 (where residual variation evaluation starts). Therefore the under-relaxation factor should be kept as close to 1 as possible while convergence is achieved for efficient use of CPU time.

By using the BiCGSTAB-ILU(0) Poisson solver and adjusting the accuracy requirement from 10^{-2} to 10^{-9} it was seen that the final emittance values are within ± 2 standard deviations of the residual fluctuation from each other after 30 iteration rounds (with $\alpha = 0.50$). This is due to the fact that, even if the Poisson solver makes only one iteration per Vlasov-Poisson iteration round, the system develops towards the solution (the electric potential from the last iteration round is used as a starting point with iterative solvers). With allowed error larger than 10^{-2} the difference in the electric potential causes large enough variation in the trajectories, compared to more accurate calculations, that the convergence is not reached even after the 100 iteration rounds. It is possible that the system does not converge at all with allowed error being this high. When the system converges, the accuracy requirement of the Poisson has no effect on the result or the magnitude of residual variation.

The particle iterator accuracy requirement was varied from 1 to 10^{-8} with particle densities n_p of 50, 500 and 5000 particles per grid cell and it was seen that the accuracy requirement has a strong effect on both the solution and the magnitude of the residual variation. The system converges with particle iterator accuracy requirement of 10^{-1} or lower. The standard deviation of the residual emittance variation relative to the average emittance from last 40 iteration rounds and the relative emittance deviation from the most accurate, $\epsilon_{\text{part}} = 10^{-8}$ result are presented in figure 5.21. The overall trend is as expected: both decrease as the accuracy requirement is tightened until

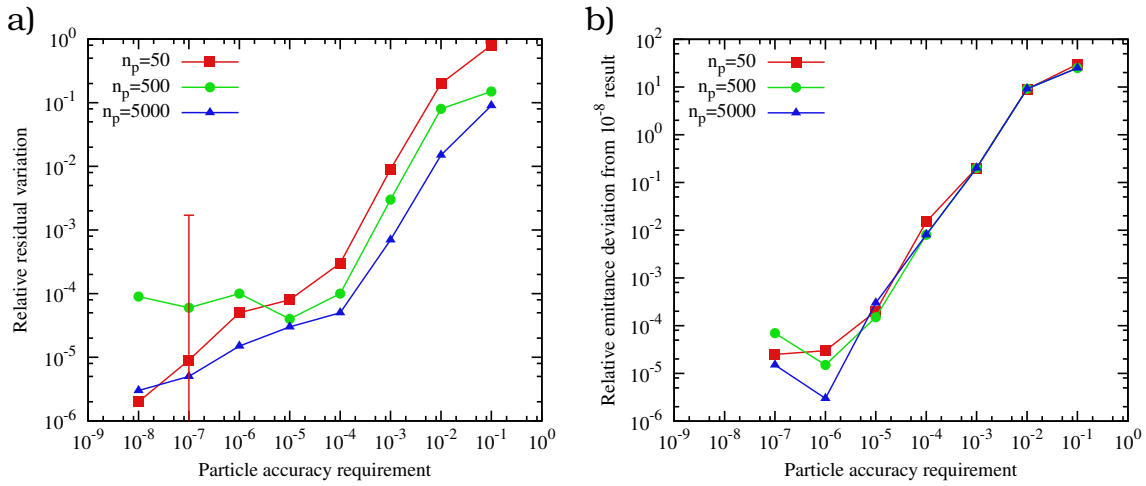

Figure 5.21: The effect of the particle accuracy requirement. a) The relative value of the standard deviation of the emittance. The error bar shows the magnitude of the contribution of a single particle trajectory passing close to the plasma electrode aperture. b) Relative deviation of the emittance from the $\epsilon_{\text{part}} = 10^{-8}$ result.

at $\epsilon_{\text{part}} \leq 10^{-5}$ the trend is broken. There the relative variation and deviation values saturate to about 10^{-5} level. By analyzing the results it can be seen that in the $n_p = 50$ case the number of particles contributing to the emittance is constant during the last 40 iteration rounds. This enables the low residual variation in that case. If only one particle which was hitting the plasma electrode would change its trajectory enough that it would be extracted close to the plasma electrode circumference, the emittance would change by about one thousandth (shown as the error bar in figure 5.21a). As the particle density increases this effect becomes more probable, but on the other hand the weight of each particle decreases. In the $n_p = 500$ case the residual variation is higher than in the $n_p = 50$ case because the particle count on the emittance plane fluctuates. In the $n_p = 5000$ case the residual variation decreases again as the particle count fluctuation becomes more statistical.

5.9.3 Error estimate

Overall, in the RADIS extraction used in these tests the grid density has the highest impact on the accuracy of the results. The relative variation of the emittance is a few percent with grid density higher than 15 grid cells in the plasma electrode aperture radius and about 10 % with 10 grid cells in the radius. In a fixed geometry a repeatability and accuracy (deviation from high precision calculation) of about 10^{-3} is easily achieved and higher 10^{-5} accuracies are achievable by investing tens of times of more CPU time on the problem.

Based on these tests a standard set of computational parameters has been established, which have been used in the simulations presented in the following chapter: The accuracy requirement for the Poisson solver $\epsilon_{\text{Poisson}} < 10^{-4}$. The under-relaxation factor α is taken as close to 1 as possible while convergence is achieved. The accuracy requirement for the particle iterator $\epsilon_{\text{part}} < 10^{-5}$ and the particle density $n_p > 100$. A grid cell size is selected to achieve density of higher than 15 grid cells in the plasma electrode aperture radius.

It is believed that in all simulation cases presented in the next chapter the error in the emittance value due to the computational effects shown here is on the order of a few percent. The overall accuracy of the simulations depends also on the validity of the plasma model and on the correctness of the input parameters. The magnitude of these effects can only be estimated by comparison to experiments, which is presented in chapter 6.

5.10 Diagnostics

Due to the openness of the simulation code architecture, it is possible to implement various kinds of diagnostics on the simulation results (or intermediate data) in the user program. In addition, the code includes several pre-made methods for common diagnostics of fields and particle trajectories. There are methods for obtaining properties of particles crossing a plane in space, which can be used to calculate distributions of location, divergence, energy, emittance, etc. There are also methods for plotting one and two-dimensional histograms of data, particle distributions, emittance ellipses, two-dimensional cross section views of the computation domain with solids, particle trajectories, equipotential lines and colourmap representations of fields, etc and three-dimensional perspective views of the geometry and beams. Many of these methods can be accessed using a graphical user interface of the code. Most of the algorithms behind the diagnostic and visualization methods are quite straightforward so they are not discussed here in greater detail. Examples of the graphical output can be seen throughout this thesis, especially in the next chapter.

Chapter 6

Extraction system design and experiments

The computational tools developed in this work have been used in analyzing and developing several existing and new ion source extraction systems. The code development was started in 2004 in Lawrence Berkeley National Laboratory for designing a pulsed D^+/T^+ slit-beam extraction system for a neutron generator [152]. In 2007 at the University of Jyväskylä the code was used to design an extraction system for a H^+ 2.45 GHz microwave ion source after which the focus of the work shifted towards negative ion extraction systems. In 2009–2010 an extraction system was designed for the Texas A&M University Cyclotron Institute H^- ion source, the negative ion plasma model was implemented in the code and the extraction was used for testing the model [7, 8]. In 2010–2011 the existing H^- extraction system of the Spallation Neutron Source (SNS) at Oak Ridge National Laboratory was modelled and a new high-current extraction system was designed [9]. A new filament-driven multicusp H^- ion source and extraction was designed and built for the JYFL electrostatic Pelletron accelerator during 2011–2012 [10]. An RF-driven H^- ion source for the MCC30/15 cyclotron is under development at JYFL and the ion source extraction was designed with the code in 2012 [10]. The ion source and the extraction system are being tested as this thesis is being written. The author has been the principal researcher of the aforementioned design and modelling work. The work conducted is described in the following sections in detail in the chronological order. The author has also participated as a collaborator in other projects, where extraction modelling has been done using IBSimu. Such projects include CERN Linac4 extraction designs for RF and magnetron ion sources [90, 153], ISIS Penning ion source extraction modelling [154], ESS-Bilbao Penning ion source extraction modelling [155] and the development of the new extraction for the JYFL 14 GHz ECR ion source [97].

6.1 Texas A&M University H^-/D^- ion source

The on-going facility upgrade for the Texas A&M University (TAMU) Cyclotron Institute aims at extending the research possibilities with stable beams and adding rare ion beam capabilities. This is done by re-activating the K150 cyclotron, which was decommissioned in 1985, to deliver high intensity light particle and heavy ion beams. These beams are used for production of rare isotopes in the targets of light and heavy ion guides for reacceleration with the K500 cyclotron. As a part of the upgrade project, a filament-driven multicusp ion source was installed in 2010 for injecting H^- and D^- beams into the K150 cyclotron using a stripping extraction for production of high energy H^+ and D^+ beams. [156, 157]

6.1.1 Ion source

A spare filament-driven multicusp ion source [158] at JYFL was found adequate for the TAMU K150 application. The ion source included a permanent magnet filter suitable for production of negative ions but it did not have an extraction system for negative ion beams. The procurement of the ion source including a design of a new extraction system was judged to be the most economical way for TAMU to gain the light ion capabilities needed for the upgrade.

6.1.2 Design of negative ion extraction

A design of an extraction system capable of extracting up to 1 mA of H^- ion beam and transporting it to the next focusing element of the beam line with low emittance growth was needed. The energy of the ion beam had to be variable from 5 to 15 keV because the injection energy of the cyclotron changes with the energy of the accelerated beam. The extraction system also had to be able to deflect tens of milliamps of co-extracted electron beam into an electron dump.

A dominant feature of a negative ion extraction system is the dumping of the co-extracted electrons, as has been discussed already before. There are several ways of dealing with the electrons. In this case, the filter field of the ion source protrudes to the extraction region, which will cause bending of the ion beam regardless of the dumping method. Therefore the tilted ion source method was chosen. The dumping magnetic field is oriented anti-parallel to the filter field of the ion source to minimize the magnetic field strength at the extraction aperture for minimal interference to the slow particles accelerated from the plasma. The dipole field was constructed using 10 6.35 mm cubical SmCo magnets as shown in figure 6.1 for maintaining field uniformity of ± 3 percent within the beam to minimize emittance growth. The resulting transverse

magnetic field in longitudinal direction on the symmetry axis of the permanent magnet array is presented in figure 6.2. The magnets were integrated in the water cooled puller electrode, engineered to handle the anticipated electron beam power of over 100 W.

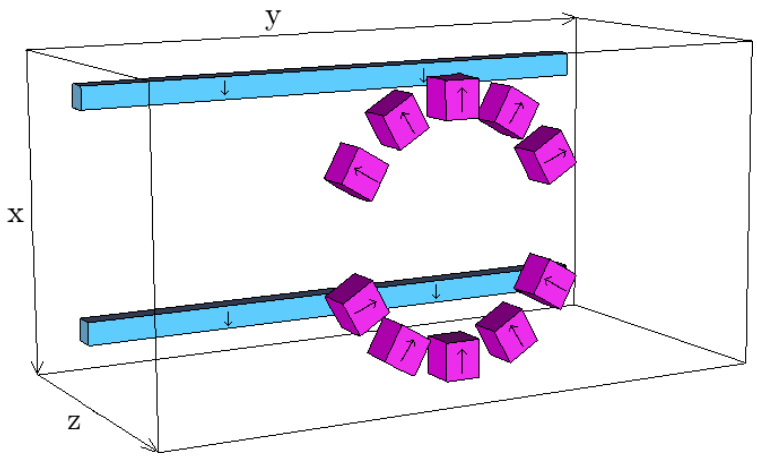

Figure 6.1: The magnet geometry with filter magnets shown in cyan and electron dump magnets shown in magenta. The magnetization directions of the magnets are shown with arrows. The electron dump magnets are located inside the puller electrode.

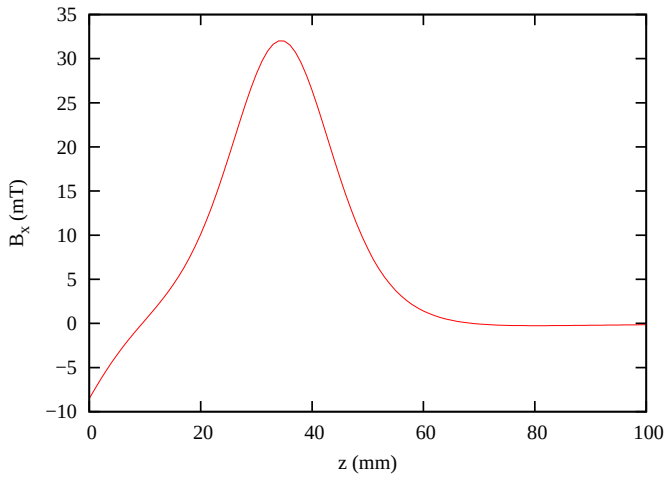

Figure 6.2: The transverse magnetic field strength in longitudinal direction on the symmetry axis of the geometry. The $z = 0$ is the inner surface of the plasma electrode as shown in figure 6.3.

Cylindrically symmetric simulations

For the ion beam to tilt to the same angle in the magnetic field regardless of the final energy, the beam energy at the puller electrode has to be fixed. In this case

a puller to plasma electrode voltage difference of 6 kV was chosen. After the puller electrode the beam is accelerated to the final energy while the focusing is adjusted using a decelerating electrode between the puller and the ground electrode in a zoom-lens configuration (einzel #1). A series of simulations was made in 2D (cylindrically symmetric) without the magnetic field to design the extraction electrode geometry and potentials for achieving a nearly parallel beam at the end of the extraction system. The 2D simulations were done using IBSimu and with a more established code PBGuns [120], which enables comparison of the results.

The nominal plasma parameters used in the simulations were plasma potential $\phi_P = 5$ V, electron to ion beam current ratio $R_{ei} = 20$, electron density coefficient $R_{ec} = 1$, electron temperature $T_e = 0.5$ eV (only in PBGuns), negative ion transverse temperature $T_t = 0.5$ eV, positive ion temperature $T_p = 0.5$ eV, ratio of fast compensating positive ions to total negative charges $R_f = 0.5$, extracted negative ion beam current density $J_{H^-} = 35.4$ A/m^2 and initial drift energy of extracted particles $E_0 = 3$ eV. Of these values plasma potential and the temperatures are rather well-known for this type of ion sources [75] and the electron to ion beam ratio was measured during initial tests. The ion current density (about 1 mA of H^- current from ⌀6 mm aperture) used in the simulations is an estimate of the ion source performance using the selected filament geometry and power supplies (maximum discharge power of about 1 kW). IBSimu and PBGuns do not use the same plasma model for negative ion extraction. PBGuns, for example, has electron space charge included as an analytic formula dependent only on the potential, while in IBSimu the extracted electrons are ray-traced like ions. PBGuns includes only thermal plasma species, while IBSimu has both thermal and fast compensating positive ion species (see chapter 5.2.2). Therefore the R_f parameter is not used in PBGuns. The analytic formula for the thermal compensating species (equation (5.5)) is the same in both codes.

The extraction system producing 1 mA H^- beam at 15 keV final beam energy has been simulated with IBSimu (figure 6.3) and PBGuns (figure 6.4) using the nominal plasma parameters. Obviously the beam behaviour predicted by the two codes differ. This is due to different plasma sheath forms, which can be seen in figure 6.5. In PBGuns the plasma sheath is more concave, which causes stronger focusing in the plasma electrode to puller electrode gap, when compared to the result given by IBSimu. This difference affects the beam behaviour also in the rest of the extraction.

Because there is some uncertainty of the plasma parameters, the source performance and the accuracy of the plasma models, the gap between the plasma and puller electrodes was decided to be made adjustable. A sensitivity analysis was made with IBSimu to see how much the gap would have to be adjusted relative to the nominal case to achieve the same plasma sheath location (location of $\phi = 2$ V on the axis) in cases where plasma parameters are modified. See table 6.1 for results. The electrode construction was made such that it allows ±6 mm gap adjustment around the design value.

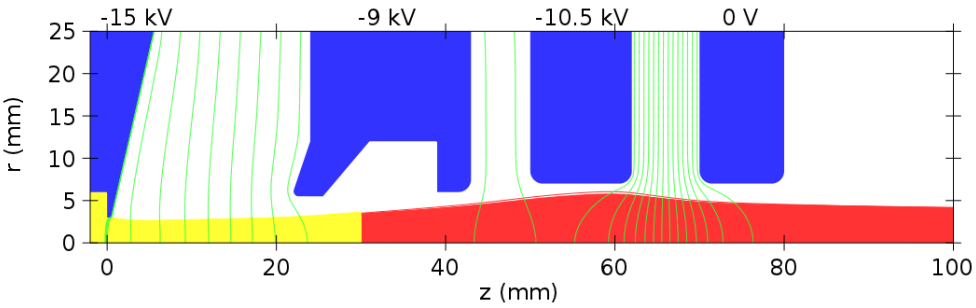

Figure 6.3: Cylindrically symmetric simulation of the extraction system with nominal plasma parameters and 15 keV final beam energy made with IBSimu. The electron beam (yellow) is artificially stopped at the dump location.

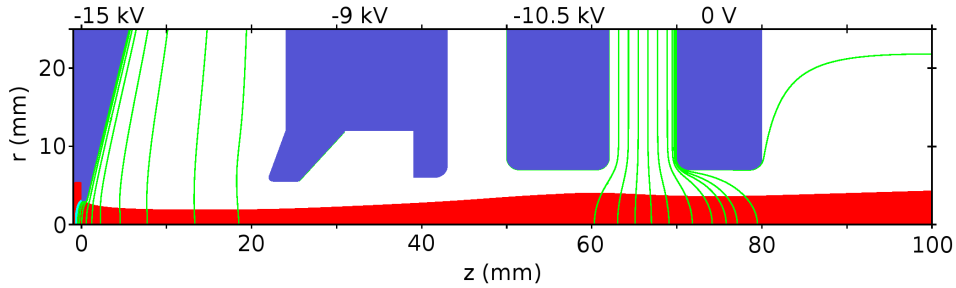

Figure 6.4: Cylindrically symmetric simulation of the extraction system with nominal plasma parameters and 15 keV final beam energy made with PBGuns.

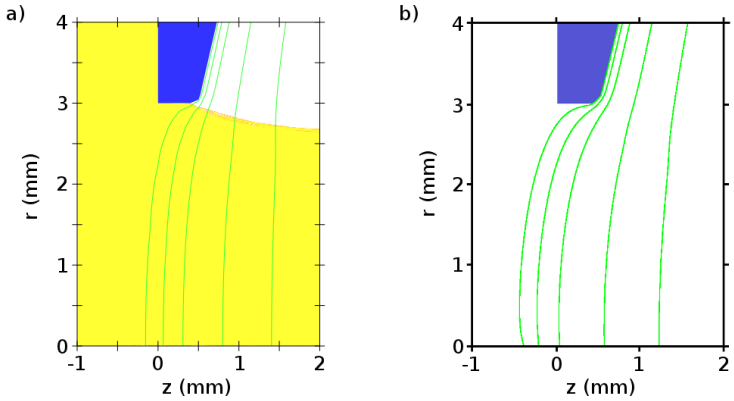

Figure 6.5: Close-up views of plasma sheath region from a) IBSimu and b) PBGuns simulations. The 2.5, 10, 25, 70 and 145 V equipotential lines are drawn for comparison purposes. In PBGuns the plasma sheath is more concave and there exists a slight but unphysical curvature in the eqipotential lines close to the axis.

Table 6.1: Sensitivity analysis results. The plasma parameters were modified from their reference values one at the time. The gap length between plasma and puller electrodes was adjusted in each case to achieve the same plasma sheath location as with the reference plasma parameters.

Parameter	Reference value	Range	Gap adjustment
E_0	3 eV	3 – 7 eV	$0 \rightarrow 2$ mm
ϕ_P	5 V	2 – 10 V	$-1 \rightarrow 1$ mm
R_{ei}	20	10 – 50	$-5 \rightarrow 3$ mm
R_{ec}	1	1 – 3	$-2 \rightarrow 0$ mm
R_f	0.5	0 – 1	$-1 \rightarrow 1$ mm
T_p	0.5 eV	0.1 – 2 eV	$-0.1 \rightarrow 3$ mm
T_t	0.5 eV	0.1 – 2 eV	$-0.1 \rightarrow 0.1$ mm

The geometry was tested with lower final energies of 12 keV, 8 keV and 5 keV. With these energies, nearly parallel beams at $z = 100$ mm can be achieved with einzel #1 voltages of -8.2 kV, -5.8 kV and -3.2 kV, correspondingly. It seems that at least with energies ranging from 15 keV to 5 keV the extraction system is adequate for accelerating up to 1 mA of H^- beam for further transport.

Three dimensional simulations

Three dimensional simulations were made for finding the optimal tilt angle and the center of rotation. The 3D magnetic field was modelled using Radia3D [159] and the field data was imported into IBSimu. The same plasma model parameters were used as in 2D with the exception of the magnetic field suppression added for regions, where the potential $\phi < \phi_W + 10$ V. In these regions the plasma is assumed to be collisional and uniform. The beam was observed to propagate to the correct angle with 12 keV final energy when the last two electrodes are rotated 74 mrad around $x = 0$, $z = 38$ mm. With this geometry, the angle of the beam at the end of the simulation was observed to vary from 70 mrad to 86 mrad when the final beam energy was varied from 15 keV to 5 keV respectively, because the magnetic dipole field is still nonzero at the einzel lens. The variation of the beam angle is so small that the tilt was made fixed. The small beam deflection can be corrected by an xy steering magnet after the extraction. A simulation of the three dimensional extraction is shown in figure 6.6. The normalized transverse rms emittance of the H^- beam at the end of the simulation is 0.044 mm mrad, while the emittance from the ion temperature (0.5 eV) is 0.035 mm mrad according to equation (4.43). The extraction therefore increases the emittance by 25 %, which is acceptable in this case.

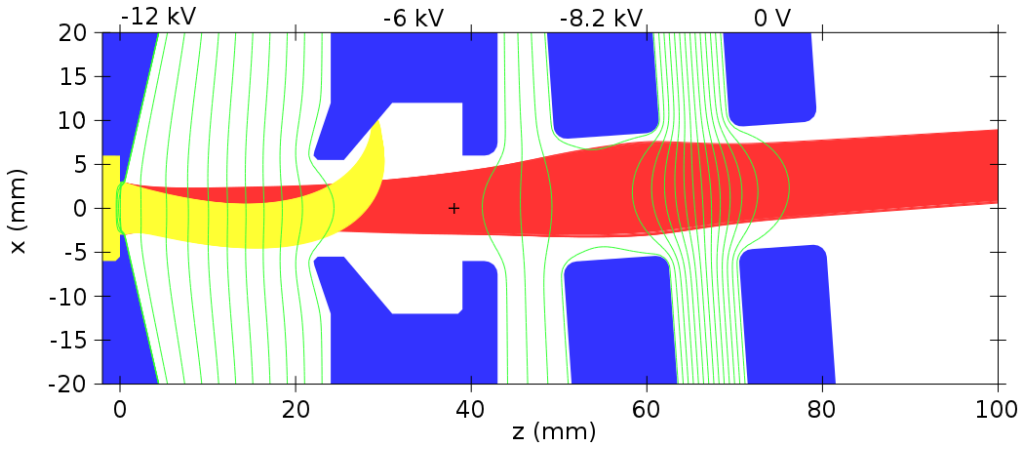

Figure 6.6: Three dimensional simulation of the extraction system with 1 mA H^- beam accelerated to 12 keV final energy. Co-extracted 20 mA electron beam is dumped to the inner surface of the puller electrode. The ion beam exits the extraction at 74 mrad angle. The center of rotation is marked with a cross.

Operation with D^-

Texas A&M Cyclotron Institute regularly operates with D^- as well as H^- beams. It is important that the same extraction system is capable of handling D^- beam as well to avoid extra work when changing from one isotope to the other. The designed extraction provides D^- beam to the LEBT using the same electrode voltages as with H^-. This is possible because the difference in beam deflection in the extraction is not proportional to $1/\sqrt{2}$ when comparing D^- to H^- as it is in a purely magnetic system (e.g. equation (4.19)). Three phenomena have been identified contributing to this effect. One of the reasons is the more concave shape of the plasma sheath due to the lower plasma density achieved with deuterium, which cause the ion beam to deflect more towards $-x$ direction in the first millimeters after of the extraction due to the residual filter field of the ion source. The second reason is the higher electron to ion ratio in the deuterium case (87 was measured), which creates a higher local negative space charge in the first gap deflecting the ion beam towards $+x$ direction. This effect is also amplified by the plasma sheath shape difference causing the electron beam to be more focused and deflected more towards $-x$ direction. The third effect contributing to the D^- beam deflection is the einzel lens, which deflects the beams because they are not centered on the axis of the lens. Overall, the D^- beam has only 4 mrad angular deviation and 0.7 mm offset from the axis of the beam line at the end of the simulation in the 12 keV case (see figure 6.7). This feature makes it possible to change between H^- and D^- beams easily, minimizing the downtime of the facility. It is also a good example of features that are very difficult to model without three dimensional ion optical codes with plasma modelling capabilities.

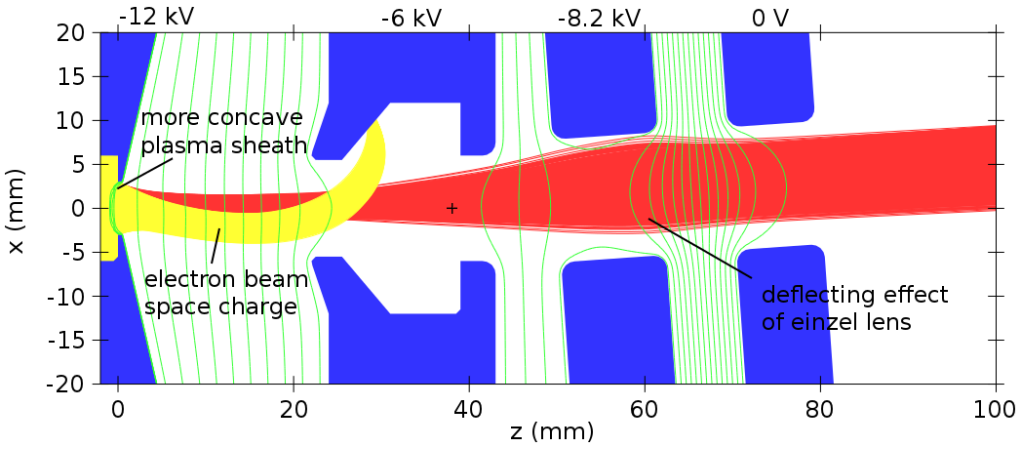

Figure 6.7: Three dimensional simulation of the extraction system with 285 μA D^- beam accelerated to 12 keV final energy. Co-extracted 27 mA electron beam is dumped inside the puller electrode. The ion beam exits the simulation at 70 mrad angle, only 4 mrad off-angle from the axis of the beam line.

6.1.3 Experiments

The ion source was installed at the injection line of the K150 cyclotron at Texas A&M, which is shared with an ECR ion source (see figure 6.8). The beam line was equipped with a vacuum chamber with three 1000 l/s turbo pumps, einzel lenses #2 and #3 and an electron suppressed Faraday cup for measuring the ion current. The ion source and the extraction were first mounted directly on the vacuum chamber, but soon it was discovered that the evaporated tantalum from the ion source filament falls onto the cyclotron inflector causing short circuits. Later a 20° tilt and an xy steering magnet was added between the extraction and the vacuum chamber to prevent this. The xy steering magnet also provides a possibility for fine tuning the beam angle.

The extraction was designed to operate at fixed 6 kV potential difference between the plasma electrode and the puller electrode. The optics were designed to produce 1 mA parallel H^- beam at different final beam energies by adjusting the einzel #1 voltage. During the experiments the puller and einzel electrode voltages were adjusted to optimize the beam transmission to the first Faraday cup at different beam energies and plasma densities. The optimal transmission was found close to the design value electrode voltages. A comparison of the experimentally optimized and simulated voltages is shown in table 6.2.

The H^- current of 1 mA on the first Faraday cup was reached with discharge current of 12.7 A at the arc discharge voltage of 100 V. The e^-/H^- ratio was approximately 25. For D^- 285 μA was measured on the first Faraday cup with plasma driven by 10 A, 100 V arc. The e^-/D^- ratio was approximately 87. Beam currents of up to

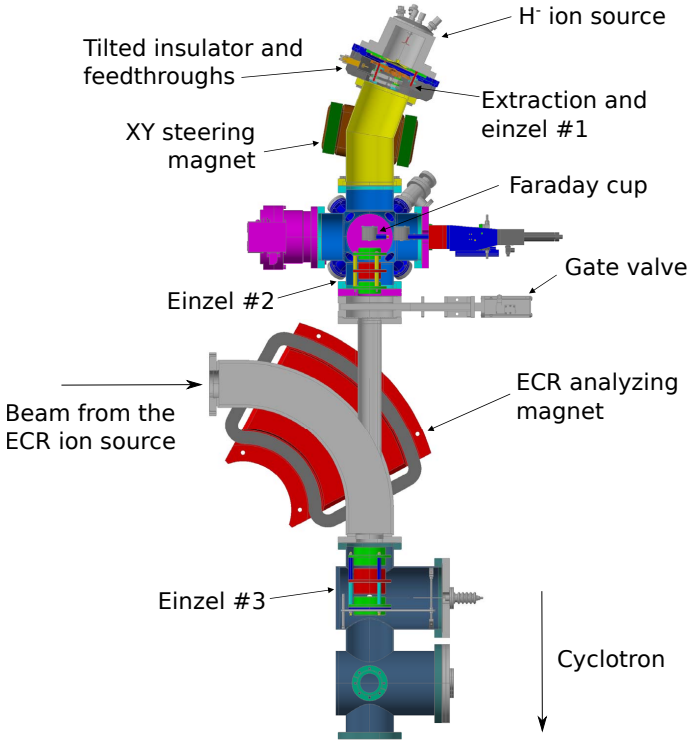

Figure 6.8: CAD visualization of the ion source, extraction system, pumps, diagnostics and the first beam focusing elements. The cyclotron inflector is located roughly 6 meters from the ion source.

Table 6.2: Comparison of (1) electrode voltages providing optimal transmission to the first Faradap cup to (2) voltages, which provide 1 mA parallel H^- beam at $z = 100$ mm in simulations. The beam current measured with the Faraday cup is not equivalent to the extracted H^- current because of unknown beam losses in the transport.

Simulation	Experiment	FC (μA)
V_{source} / V_{puller} / V_{einzel}	V_{source} / V_{puller} / V_{einzel}	
-5 kV / $+1$ kV / -3.2 kV	-5 kV / 0.5 kV / -3.1 kV	360
-8 kV / -2 kV / -5.8 kV	-8 kV / 0.7 kV / -5.7 kV	365
-10 kV / -4 kV / -7.0 kV	-10 kV / -2.9 kV / -7.4 kV	369
	-10 kV / -2.3 kV / -7.4 kV	962

25 μA of H^+ and 15 μA of D^+ have been extracted at energies up to 30 MeV and 20 MeV respectively from the cyclotron with stripping extraction and measured from the first Faraday cup outside the cyclotron.

Overall, the experimental work done with the ion source extraction shows that the extraction design process has been successful.

6.2 SNS RF ion source extraction

The US Spallation Neutron Source at Oak Ridge National Laboratory uses an RF-driven internal antenna multicusp ion source for producing $\sim$ 1 ms long pulses H^- beam at 60 Hz to the radio frequency quadrupole (RFQ) accelerator, which injects the beam at 2.5 MeV into the SNS linac. The source and RFQ are currently coupled by an electrostatic, six-electrode *baseline* extraction system that forms, accelerates, focuses, steers and chops the 65 keV H^- beam forming the pulse structure required by the accelerator complex. The co-extracted electron beam is dumped at low energy with a strong transverse magnetic field near the plasma electrode aperture causing also the H^- beam to deflect to an angle. The ion source is mounted at an angle with respect to the beam line to compensate for the deflection. See figure 6.9 for a schematic of the ion source and extraction system. [160, 161]

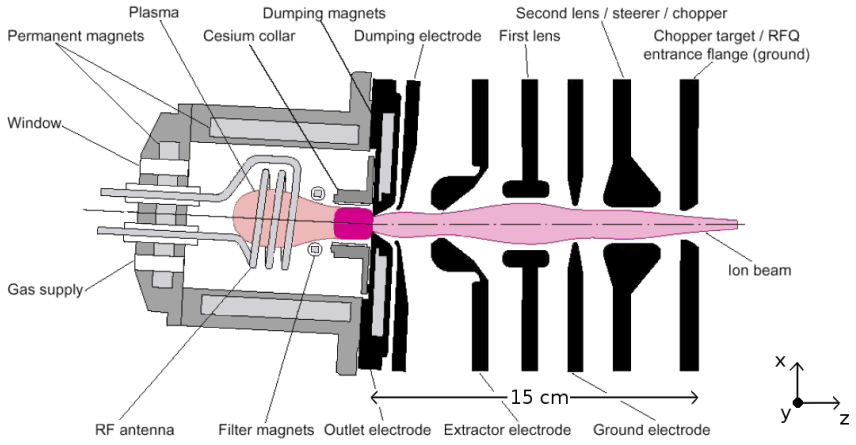

Figure 6.9: Schematic of the ion source and extraction systems. The width of the ion beam is exaggerated to emphasize the focusing action of the lenses. [162]

The front-end routinely provides beam currents of 35–40 mA into the SNS linac, which corresponds to about 50 mA of H^- out of the ion source [163]. Future SNS power upgrade plans will require linac beam currents of $\sim$ 60 mA with about the same duty factor. To support this goal and to increase reliability of the current system,

the existing system and a proposed high-current extraction system have been studied using IBSimu. [86, 9]

In this simulation study, a set of plasma parameters has been chosen, which are believed to be close to reality and give a good match between simulations and experiments. These are the plasma potential $\phi_P = 15$ V, electron to ion beam current ratio $R_{ei} = 10$, electron density coefficient $R_{ec} = 1$, negative ion and electron transverse temperature $T_t = 2.0$ eV, positive ion temperature $T_p = 0.5$ eV, ratio of fast compensating positive ions to total negative charges $R_f = 0.5$ and initial drift energy of extracted particles $E_0 = 2$ eV. These parameters have been kept constant in all the simulations shown here unless otherwise mentioned. The electrode voltages used in the simulations are $V_{\text{source}} = -65$ kV on the ion source plasma electrode, $V_{\text{dump}} = -58.8$ kV on the dump electrode, $V_{\text{E1}} = -48$ kV on the first einzel lens and $V_{\text{E2}} = -46$ kV on the second einzel lens. Other electrodes are at ground potential.

6.2.1 The baseline extraction system

Angle and offset

The angle of the SNS ion source with respect to the beam line axis can be adjusted to compensate for the deflection caused by the permanent magnet electron dumping field. The ion source can also be translated in x-direction to provide a total of two degrees of freedom (angle and offset) for adjusting the beam angle and spatial coordinate at the RFQ entrance. Originally the system was designed to operate with about 3° angle (52 mrad), but more recently it has been observed that the optimum angle and offset vary when extraction system and ion source are replaced during maintenance [164]. It seems that the system is very sensitive to alignment of assembled parts and/or that there are differences in critical parts of sources and extraction systems. There are several sources and extractions used for beam production. It is known that there are 10 % differences in the dumping magnetic field intensities of the ion sources but that is not the cause of all observed variations. Therefore a simulation study has been performed with 45 mA of extracted H^- current to gain understanding to the correlations between the ion source angle and offset and the beam current accelerated by the RFQ close to the typical operational parameters.

It was noticed that the emittance and Twiss parameters of the beam at the RFQ entrance are quite insensitive to the ion source angle and offset as long as the beam does not intercept the electrodes. The beam angle x_{ave} and offset x'_{ave} in the direction transverse to y and the RFQ axis at the RFQ entrance plane are more sensitive to these parameters. The effect of the ion source tilt and offset to the mean beam location in phase space is shown in figure 6.10. In this simulation study it is assumed that the optimum transmission through the RFQ is achieved when the H^- beam is

focused to the RFQ entrance centered and at 0 mrad angle within an acceptance ellipse characterized by the Twiss parameters $\alpha = 1.7$ and $\beta = 0.06$ m/rad and $\epsilon = 4 \times 0.2$ mm mrad normalized [161]. Under this assumption the optimum was found at 56.3 mrad (3.2°) source tilt angle and −0.28 mm offset (see figure 6.11). Although, these parameters have not been used for source operation at SNS, they are used in the simulations shown in this work as an ideal reference point. Recent studies at SNS have shown that the alignment of the LEBT may not be the only reason why the optimum angle and offset have changed. The RFQ has degraded over time which makes the assumption of the ideal RFQ injection questionable [165]. Because of these reasons comparison to measured angles and offsets is difficult and not very meaningful.

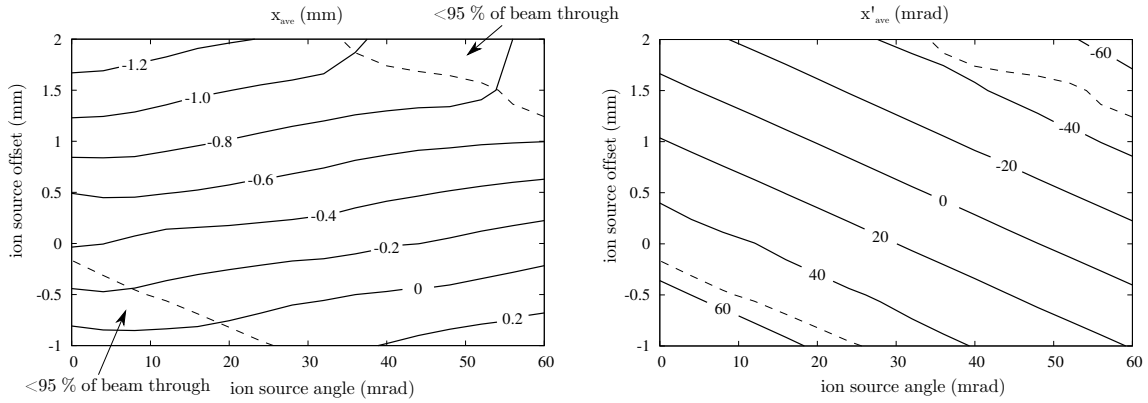

Figure 6.10: The average beam location x_{ave} and angle x'_{ave} in the direction transverse to y and the RFQ axis at the RFQ entrance plane as a function of ion source angle and offset. The area where beam is significantly intercepted by the electrodes is indicated by dashed line.

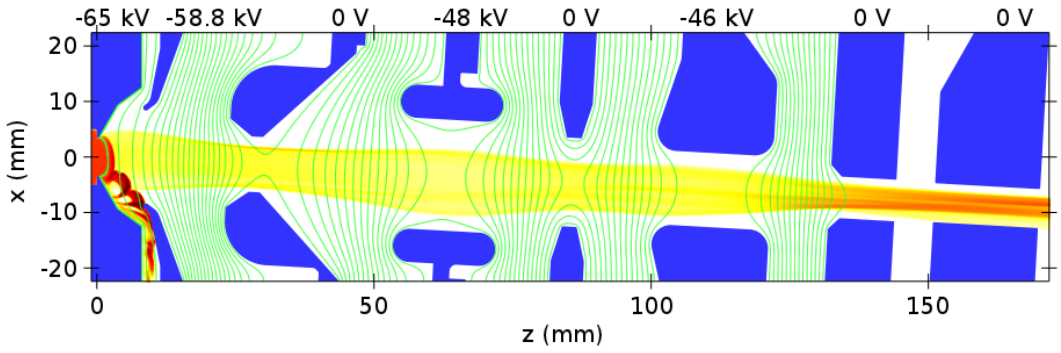

Figure 6.11: Simulation of the reference case with ion source at 56.3 mrad angle and −0.28 mm offset.

The sensitivity of the system can be seen by studying a deviation from the reference point. It has been estimated that the angle of the ion source can be reset within ±0.2°

of the intended and the offset within ±0.2 mm. Therefore these values were used as the size of perturbation in this simulation study. The beam at the RFQ entrance was observed to vary by ±10 mrad and ±0.1 mm with this perturbation. Especially the beam angle variations at the RFQ entrance plane are significant (roughly 30 % of the RFQ acceptance ellipse size in x'-direction). It seems therefore likely that small unintentional variations of the ion source angle and offset during maintenance may result in the observed large differences in accelerated beam current.

The optimum case presented here is found using the recent version of the code described in this thesis. It is different from the optimal solution (24.4 mrad angle and 0.8 mm offset) which was found in 2010–2011 when the original study [9] was conducted with the code version of the day. The difference in the results is caused by the method used for electrode edge smoothing. In the original study the virtual potential method described by equation (5.29) was used. Currently the code uses the modified Poisson equation in the near-solid nodes, which produces a higher quality approximation of the potential near the solids compared to the virtual potential method. Therefore it is believed that the newer result is more likely to be correct. This is also a good indication that the SNS extraction system is highly sensitive to small variations at the proximity of the plasma sheath.

The beam angle and offset at the RFQ entrance may be fine tuned by deflecting with the chopper electrode and by adjusting the Einzel lenses. This is quite difficult in practice because of the high number of parameters which are affecting not only the beam angle and offset, but also the Twiss parameters, which affect the beam transmission through the RFQ.

Emittance

The future SNS power upgrade plans may require higher H^- currents than what have been accelerated so far. From emittance measurements made at the SNS [166], it can be seen that the transverse emittance increases strongly with increasing beam current. Difficulties are expected as the transmission coefficient of the RFQ is expected to decrease with increasing emittance and with increasing beam current. The nominal acceptance limit for the RFQ is about 0.2 mm mrad at 60 mA input current, which should result in 95 % beam transmission [161]. The extraction system was simulated with the ion source producing H^- beam currents of 10–60 mA. The transverse emittance at the RFQ reference plane was recorded in the direction of the source tilt (x, x') and in the perpendicular direction (y, y'). The ratio $\epsilon_{xx'}/\epsilon_{yy'}$ varies between 0.9 and 1.1 in these cases. Therefore it is sufficient to analyze only the (y, y') direction for which experimental data is available from reference [166]. The simulation emittance data is shown in figure 6.12 together with experimental data. It can be seen that the trend is well reproduced. There exists an optimum current in simulations at roughly

20–30 mA. According to experimental data, the optimum is roughly at 25–35 mA. The difference in the optimum location may be due to inaccuracy in the electron current. In the electron dump design used in the SNS ion source only part of the electrons are measured as the electron dump power supply current. The e^-/H^- ratio of 10 used in the simulation is based on an estimate. Beam currents lower or higher than the optimum lead to increasing emittance values. The reason for the emittance increase at high currents is the low electric field at the first gap, which leads to highly convex plasma sheath. The rest of the LEBT contributes only slightly to the emittance with the exception of the very lowest beam intensities.

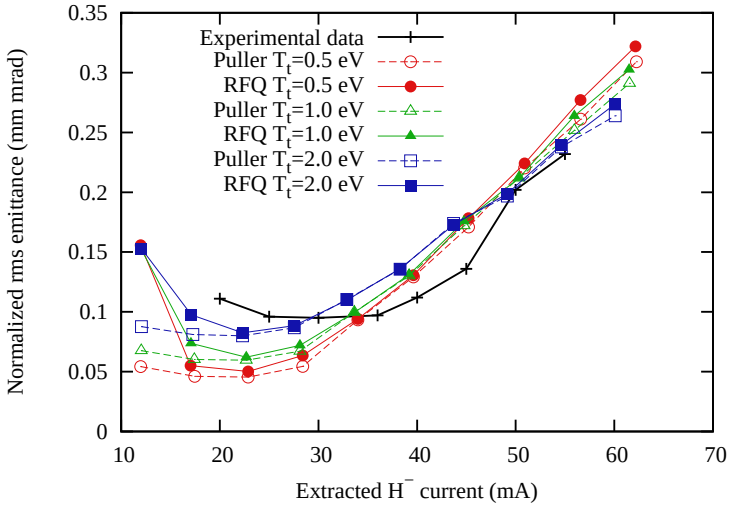

Figure 6.12: The normalized (y, y') rms emittance at the puller electrode and at the RFQ entrance for three initial ion transverse temperatures of 0.5 eV, 1 eV and 2 eV as a function of extracted ion current. The experimental data is from reference [166].

6.2.2 Proposed new injection system

The baseline extraction system has suffered from alignment issues discussed above and high voltage sparking problems. To mitigate these weaknesses a 2-solenoid magnetic LEBT has been under development at SNS [167, 168]. The existing electrostatic plasma, electron dump and puller electrodes have not been changed in the magnetic LEBT study [168]. Therefore the problem of emittance growth at higher currents and possible extraction inefficiencies due to the low voltage between the plasma and electron dump electrodes persist in that design. To find a better solution for the whole low energy beam transport a new electrostatic extraction has been studied [169, 9].

Electrostatic extraction

The new plasma and puller electrode geometry has been designed to achieve a flat plasma sheath with 65 kV gap voltage and 100 mA H^- beam to minimize emittance growth of the beam. To achieve this the electric field in front of the plasma electrode has to be higher than what is possible in the baseline extraction system due to the electron dump electrode. In the proposed extraction the electron dumping is done at 10 keV after deceleration (see figure 6.13). The puller electrode voltage has to be adjustable between 25 kV and 0 V for optimal plasma sheath shape and minimal beam emittance at beam currents ranging from 40 mA to 100 mA respectively.

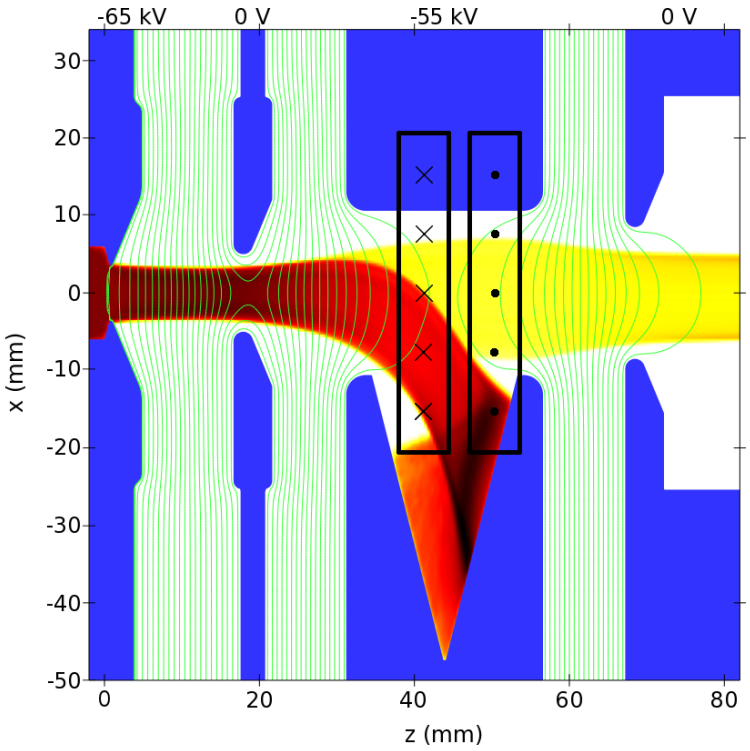

Figure 6.13: The proposed new extraction system with 100 mA of H^- extracted and 1 A of electrons dumped in the einzel lens at 10 keV.

The einzel lens following the puller electrode is at −55 kV. The electrode has an integrated SmCo magnets for creating two opposing dipole fields. The first dipole with on-axis peak field of 22 mT deflects the co-extracted electrons to a water cooled electron dump. The second dipole field corrects the H^- deflection and helps to spread the electron beam in the dump, which needs to dissipate the expected 1 A, 10 keV electron beam at 6 % duty cycle. The electron dump magnetic field and geometry are optimized to spread the electron beam to a large surface area to achieve small power densities. The surface power density of the dump is shown in figure 6.14. The peak power density value 400 W/mm^2 during the pulse is below the critical value of

1 kW/mm^2 for copper, at which the surface of the dump starts melting, but a higher safety factor would be preferred. The 1 kW/mm^2 limiting value was deduced from 1D thermodynamic simulations for a water cooled, 3 mm thick copper dump with the beam pulse pattern specific for SNS.

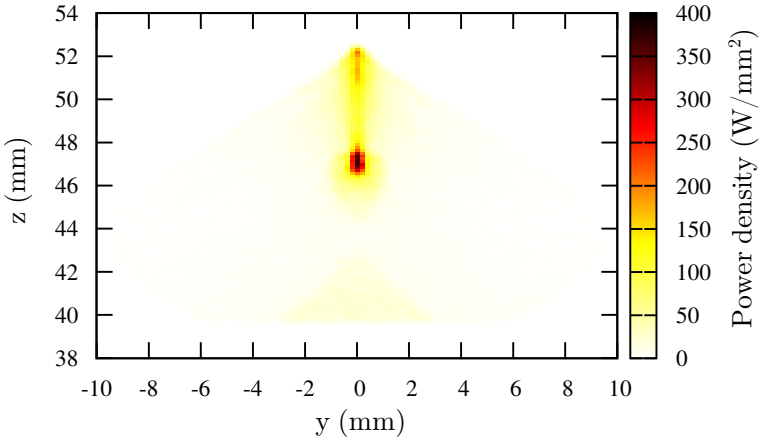

Figure 6.14: The power density on the electron dump during the beam pulse. The peak power density is below 400 W/mm^2.

The H$^-$ beam will exit the extraction with a slight angle, which depends on the voltage of the puller electrode. Therefore the extraction must be followed by a pair of electrostatic deflector plates or steering magnets to return the beam back to axis. The deflectors also allow slight adjustments to be made to the beam location and angle making the design more robust to alignment issues. The simulations of the proposed extraction show a roughly constant transverse emittance between 40 and 100 mA current as shown in figure 6.15. The emittance at 60 mA is 0.11 mm mrad, while for the baseline extraction, at the same beam current, the emittance value is 0.27 mm mrad after the puller electrode. This significant difference in emittance is a strong reason to prefer the proposed extraction and dumping method with magnetic LEBT if the high power electron dumping can be experimentally proven for the operational parameters of the SNS ion source. The same type of electron dumping scheme has also been developed at CERN for the Linac4 H$^-$ extraction system [90]. At CERN the extraction system has proven the performance extracting 17 mA, 400 μs long pulses of H$^-$ at about 1 Hz repetition rate and dumping the co-extracted 1.2 A electron beam at 9 keV energy into a tungsten dump [170].

Magnetic LEBT

The 2-solenoid magnetic LEBT design under development at SNS provides room for diagnostics between the solenoids and for deflector plates before the RFQ for high speed chopping of the beam. Deflector plates or magnetic steerers can also be fitted

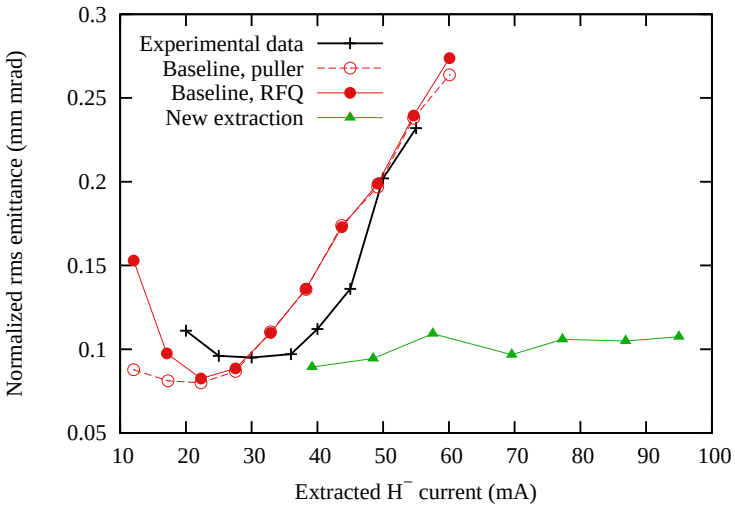

Figure 6.15: Transverse (y, y') emittance of H^- beam as a function of beam intensity according to simulations with $T_t = 2.0$ eV. New extraction emittance values are from simulations with optized puller electrode voltage.

before the first solenoid. The upgrade from the baseline system to the magnetic LEBT would therefore allow better control of the beam with independent solenoid focusing and steering elements for correcting the alignment errors.

The compatibility of the presented electrostatic extraction with the magnetic LEBT design was verified by ion optical simulations. The solenoid field used was calculated with FEMM [171] and the magnetic field data was imported to simulations. The magnetic LEBT was simulated starting with the particle data from the extraction system simulations with $T_t = 1.0$ eV. The solenoid currents and locations were fine-tuned by automatic optimizer to find a solution, which maximizes the H^- beam inside the RFQ acceptance ellipse with Twiss parameters $\alpha = 1.7$ and $\beta = 0.06$ m/rad and $\epsilon = 4 \times 0.2$ mm mrad normalized. This is just a rough model of the real acceptance of the RFQ, but it enables convenient optimization. A 90 % space charge compensation between $z = 300$ mm and $z = 1200$ mm was used, which is expected in such a system [172]. According to the simulations, the 2-solenoid LEBT delivers 84 mA of the 100 mA extracted beam within the RFQ acceptance. At 60 mA beam intensity, the beam within the acceptance is 51 mA (85 %).

The magnetic LEBT was also simulated using 60 mA particle data from an extraction consisting only of the plasma electrode, electron dump and puller electrode of the baseline system for comparison purposes. Using the same optimization procedure 43 mA (72 %) of beam is transported within the acceptance. This is lower than what is achieved by using the proposed extraction mainly due to the difference in the emittance after the extraction.

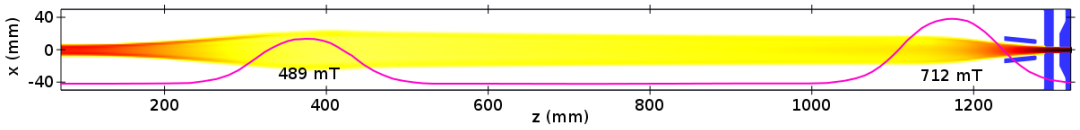

Figure 6.16: Simulation plot of the optimal configuration of the magnetic LEBT transporting 100 mA of beam. The on-axis magnetic field of the system is indicated with magenta curve.

6.3 H^- ion source for JYFL Pelletron accelerator

The 1.7 MV Pelletron accelerator was donated to the Department of Physics, University of Jyväskylä (JYFL) Accelerator Laboratory by VTT Technical Research Center of Finland in 2006 and since then, active development of the Pelletron facility has taken place. The main applications of the Pelletron facility are modification and analysis of materials using ion beam lithography, Rutherford backscattering (RBS), particle induced X-ray emission (PIXE) and time-of-flight elastic recoil detection analysis (ToF-ERDA). In the beginning of 2011 the accelerator had two ion sources, SNICS and Alphatross, for production of negative ions from H^- to Au^-. The PIXE and lithography applications in addition to the planned microbeam imaging facility [173] would benefit significantly from increased H^- beam brightness and better stability compared to the H^- beams available from the Alphatross and SNICS ion sources. Therefore a project was started to develop PELLIS, the *Pelletron Light Ion Source*, an ion source dedicated for low emittance H^- beam production.

An ion source and extraction system designed and optimized for providing low emittance beams is highly suitable for comparisons between plasma model and experiments. An extraction system which can be operated with a wide intensity range of beams, while keeping the emittance growth to minimum, is essential for making observations of the beam formation. In many cases the beam formation effects are masked by non-linear focusing in the extraction. The PELLIS system was designed not only as a tool for providing low emittance beam but also as a test bench for H^- plasma extraction modelling software.

6.3.1 Ion Source Design

The PELLIS ion source shown in figure 6.17 is a filament-driven multicusp ion source with 78 mm plasma chamber diameter. The plasma confinement is achieved with 16 $10 \times 10 \times 120$ mm NdFeB-42 magnets in a multicusp arrangement immersed in cooling water. On the ion source back plate there are 4 rows of $7 \times 7 \times 77$ mm NdFeB-42 magnets arranged to form a continuation of the cusp. Between the back plate magnets there is a single 1.5 mm diameter tantalum filament, which is heated with DC current

up to 80 A to maintain up to 11 A, 100–120 V arc discharge sustaining the plasma. The aluminum front plate of the ion source has a 18–10.1 mm diameter, 23.5 mm long conical channel leading to a plasma electrode insert with 2 mm diameter aperture. The insert can be easily changed if higher current or lower emittance beam is required. Inside the front plate there is also a pair of electromagnets creating an adjustable electron filter field which is essential for the volume production of H^-. The magnets are wound with 0.95 mm diameter copper wire around SS430 cores with 3×70 rounds each. The electromagnets are immersed in cooling water and tolerate up to 20 A of current for a maximum filter field of 67 mT. The ion source filter field is separated from the extraction area by a plasma-electrode insert made from magnetic SS430 steel. The steel insert acts as a field clamp minimizing the penetration of the filter field to the extraction, which would cause unwanted bending of the beam. The plasma meniscus is located in a volume, where $|B| < 9$ mT with all possible electromagnet settings and $|B| < 4$ mT with the typical magnet current of less than 2 A. See figure 6.18 for magnetic field on the ion source axis with different magnet currents.

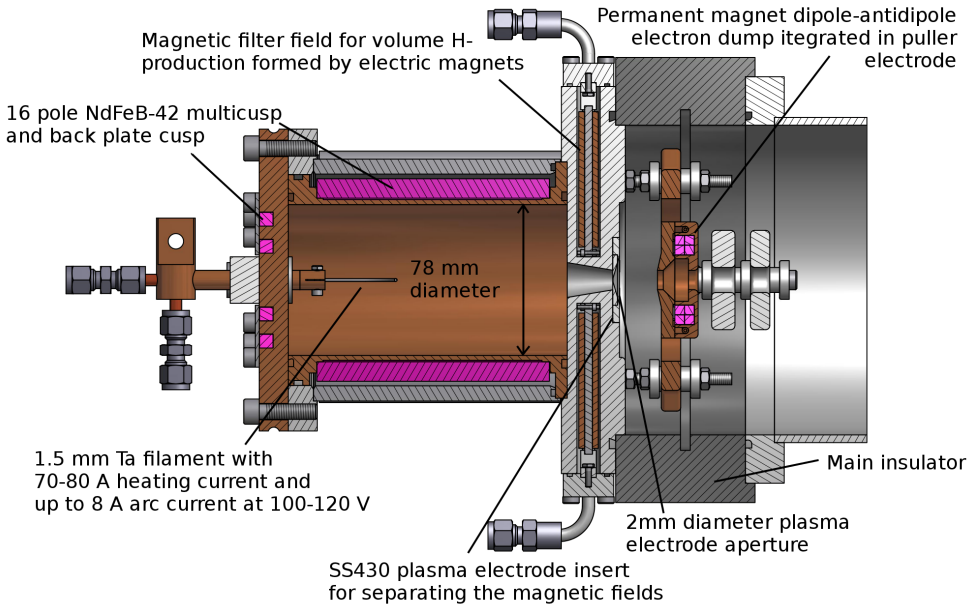

Figure 6.17: Cross-sectional view of the PELLIS ion source with main parts labelled.

The ion source extraction is quite similar to the Texas A&M Cyclotron Institute H^- ion source presented in the chapter 6.1. A typical injection energy used on the Pelletron accelerator is 10 keV. Therefore the ion source is nominally at −10 kV with respect to the laboratory ground, but voltages from −6 to −15 kV can be used. The puller electrode, which is nominally at +5 kV potential with respect to the ion source, has 40 $5 \times 5 \times 5$ mm NdFeB-42 magnets for creating two opposing dipole fields, which deflecting the co-extracted electrons into the water-cooled electron dump while the ion beam continues with roughly unaltered angle due to the second correcting dipole field.

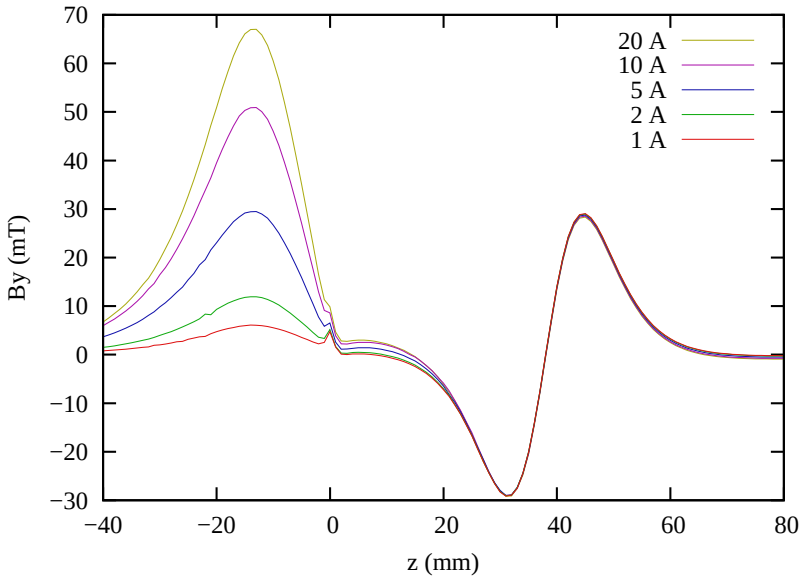

Figure 6.18: Magnetic field B_y simulated with Radia-3D [159] on the ion source axis with different currents on the electric magnet. The origin ($z = 0$) is at the plasma electrode surface facing the plasma and positive z-direction is towards the extraction. The other magnetic field components are zero on the axis.

This allows a simpler mechanical design compared to the Texas A&M case, where the ion source was tilted to compensate the ion beam deflection in the magnetic field. The magnetic puller electrode is followed by an einzel electrode with a nominal −5.5 kV potential, which is used to optimize the beam transmission to the following beam transport line. The last electrode is at ground. The ion beam suffers from a slight offset inside the puller electrode due to the electron dump magnetic field. This causes the beam to bend to a 5 mrad angle in the einzel lens according to simulations.

The ion source and the extraction vacuum chamber with a second einzel lens are installed in the middle branch of the three-way switching magnet of the accelerator injection line at a 2° angle. The angle is small enough to allow optical alignment of the accelerator through the extraction vacuum chamber. On the other hand it is large enough to prevent fast neutrals, born via beam stripping in the high background gas pressure areas of the extraction, from entering the accelerator. The switching magnet is used together with following electrostatic deflector plates to correct for 2° degree bend at the magnet and the effects of the 5 mrad angular error at the first einzel lens.

One of the main goals in designing the ion source was to build a tool for making low emittance beams. For this reason the plasma-electrode to puller-electrode gap was made adjustable by mounting the electrodes to threaded rods. The gap was optimized experimentally by making emittance scans and changing the distance according to the results. Two such iterations were made to achieve minimum emittance with puller

electrode to plasma electrode voltages of +4 to +7 kV at 20 to 60 μA beam intensities.

6.3.2 Extraction simulations

During the design of the PELLIS extraction system, the simulations were done using the same plasma parameters, which were used with the similar filament-driven Texas A&M ion source, with the exception of the lower current densities ($\phi_P = 5$ V, $R_{ei} = 20$, $R_{ec} = 1$, $T_e = 0.5$ eV, $T_t = 0.5$ eV, $T_p = 0.5$ eV, $R_f = 0.5$, $J_{H^-} = 5$–15 A/m^2 and $E_0 = 3$ eV). After the experiments, some of the plasma parameters were changed to match the simulation results to the experimental observations. Making all of these simulations of the PELLIS extraction system posed a new difficulty compared to the previous work. Due to the 2 mm diameter extraction hole it is necessary to have a relatively high mesh density to minimize the computational artefacts near the plasma electrode surfaces. In the same time, the simulated distance to the emittance scanner is almost 170 mm, which brings the number of nodes in a 3D simulation to over 10^8. The CPU time and memory requirements for such simulations are highly impractical. Therefore, the system has been modelled by coupling two simulations together. First the whole domain (DOM1) was simulated in a regular manner using $h = 0.2$ mm mesh step size to convergence. The second simulation with $h = 0.066$ mm mesh step size was made in the volume close to the plasma electrode aperture (DOM2) using Dirichlet boundary condition with boundary node potentials from the first simulation. As a third phase, the whole domain was simulated again with fixed node potentials in a volume slightly smaller (DOM3) than what was simulated with fine resolution. The smaller volume was used here to allow the potentials close to the fine calculation volume to evolve from the first simulation. The beams in the third simulation were defined as a continuation of the beams exiting DOM2 in the fine resolution simulation. Therefore, no plasma calculation was needed in third simulation making convergence

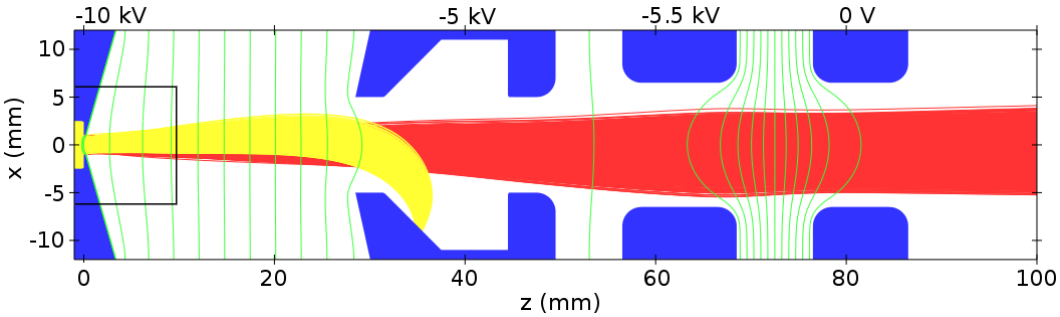

Figure 6.19: Three-dimensional simulation of the PELLIS extraction with 1.3 mA electron beam (yellow) being deflected into the electron dump and 40 μA H$^-$ beam (red) continuing through the extraction. The fine calculation volume (DOM2) close to the plasma electrode aperture is indicated with a black rectangle.

fast. Using this three-phase method, accurate simulations of the extraction system could be made with less than 10^7 nodes in each simulation, while reaching 15 grid cell resolution in the plasma electrode aperture radius. The adequacy of the resolution was verified by comparisons to higher resolution simulations in selected cases. An example of a three-dimensional simulation of the PELLIS extraction with 1.3 mA electron beam and 40 μA H^- extracted is shown in figure 6.19.

6.3.3 Measurements and comparison to simulations

H^- and electron current measurements

The extraction was characterized with current and emittance measurements with the first acceleration gap set to the optimized distance as described before. The H^- current was determined using an electron suppressed Faraday cup with 55 mm diameter entrance aperture at 120 mm from the plasma electrode and the electron current was determined from the puller high voltage power supply drain. Due to the high magnetic field and the geometry of the electron dump it is believed that the secondary electrons are contained within the dump to a high degree. The beam currents were measured as a function of the arc current and filter magnetic field at constant 0.5 Pa ion source pressure, which is the optimum pressure for H^- production at 1 A arc current and 1.8 A filter magnet current. Nominal extraction voltages were used. The measurement results are shown in figure 6.20.

The current measurements show that the optimum magnetic filter field does not change strongly with plasma density: between 0.58 and 5.6 A discharge currents the optimum filter peak field is between 8 and 11 mT (1.3 A and 1.8 A) respectively. The extracted ion current is not very sensitive to the filter field strength and therefore for future ion sources of this type the filter field could be made with permanent magnets optimized by trying different magnet grades or sizes, compromising 5–10 % of the performance. On the other hand, on state-of-the-art volume production ion sources, changing from permanent magnet filter to an electromagnet to achieve a small gain in performance may be worth the increased complexity and cost. In the rest of the presented measurements the filter magnet has been operated with a constant 1.8 A current.

In addition to the filter field, also the ion source gas pressure has a strong effect to the observed electron to negative ion ratio. The electron to negative ion ratio measured using 5 kV plasma-electrode to puller-electrode voltage is presented in figure 6.21 as a function of filament arc current for four ion source pressures. The relative amount of extracted electrons increases with decreasing pressure. The observed increase in electron to negative ion ratio with low and high arc currents may be partially caused by collimation of H^- beam to puller and/or einzel electrodes. In simulations the

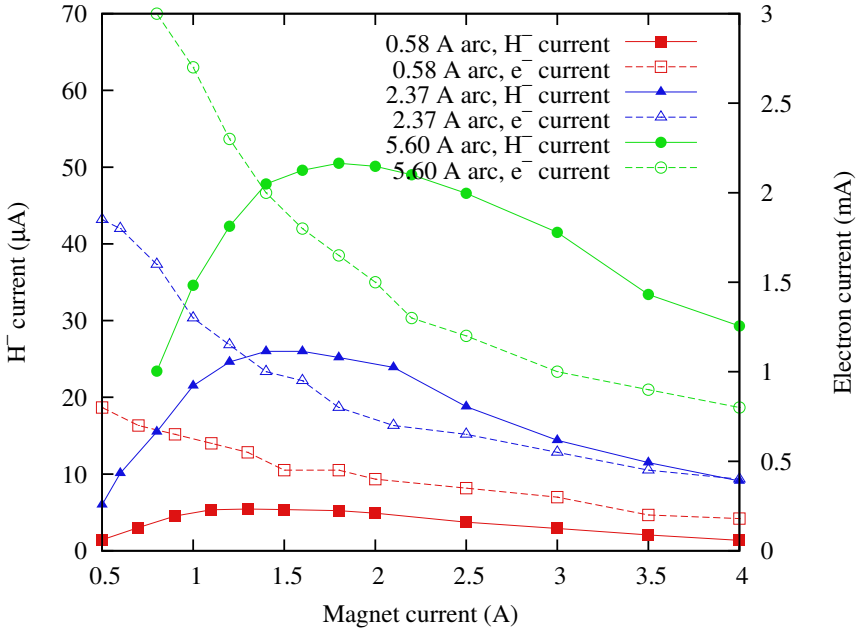

Figure 6.20: Measured H^- and electron currents as a function of the filter magnet current for different arc current levels at 0.5 Pa ion source pressure. Filter field dependence on magnet current can be seen in figure 6.18.

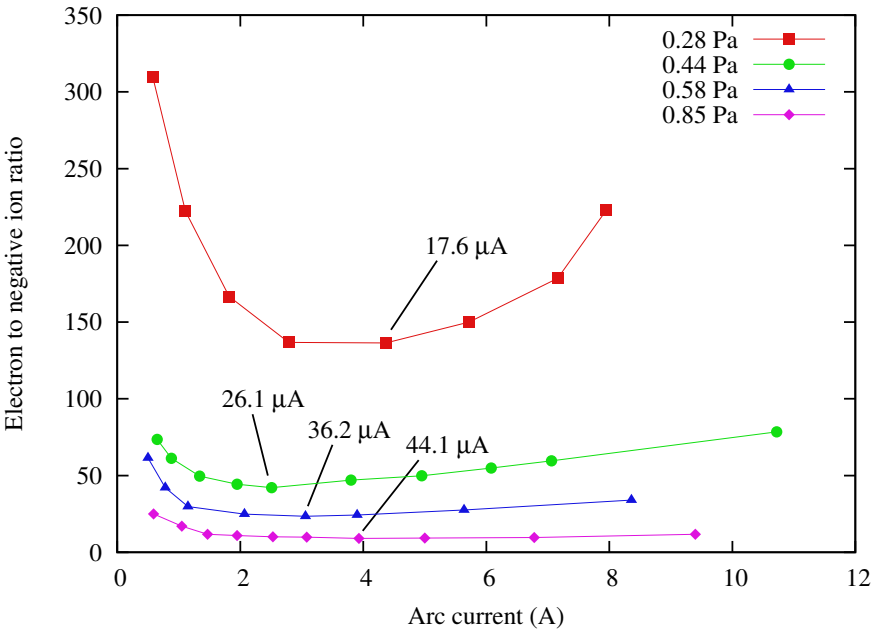

Figure 6.21: Measured electron to negative ion ratio as a function of arc current for different ion source gas pressures. The H^- beam current at the minimum e^-/H^- point for each pressure is indicated in the figure.

amount of collimation in the measured parameter range is limited to < 1 %. In the experimental conditions there was no method for estimating the amount of beam collimation.

Emittance measurements

The emittance measurements were made using an Allison-type scanner attached to the ion source main insulator. The first slit of the scanner was at 169 mm distance from the plasma electrode as shown in figure 6.22. A ⌀55 mm aperture Faraday cup was located behind the emittance scanner for measuring the extracted H^- current. The e^- and H^- currents measured during the emittance measurements were compared to values measured without the emittance scanner with the same Faraday cup at roughly 160 mm distance from the plasma electrode. At the same ion source settings the H^- currents were within ± 10 of each other. This was done to verify that most of the H^- beam is captured by the Faraday cup during the emittance measurements and that the current values are true. Emittance measurements were made in both (x, x') and (y, y') planes varying the arc current and puller electrode voltage. The negative x-coordinate is the direction in which the electrons are bent to the electron dump as is shown in figure 6.19. The rms emittance values were calculated from data processed by correcting amplifier bias and filtering by thresholding to contain 95 % of the beam. In figure 6.23a the (x, x') rms emittance values measured with four different ion source pressures with varying arc current using 5 kV plasma-electrode to puller-electrode voltage are shown as a function of measured H^- current. For each ion source pressure there is a minimum emittance at certain H^- current level. This optimum corresponds

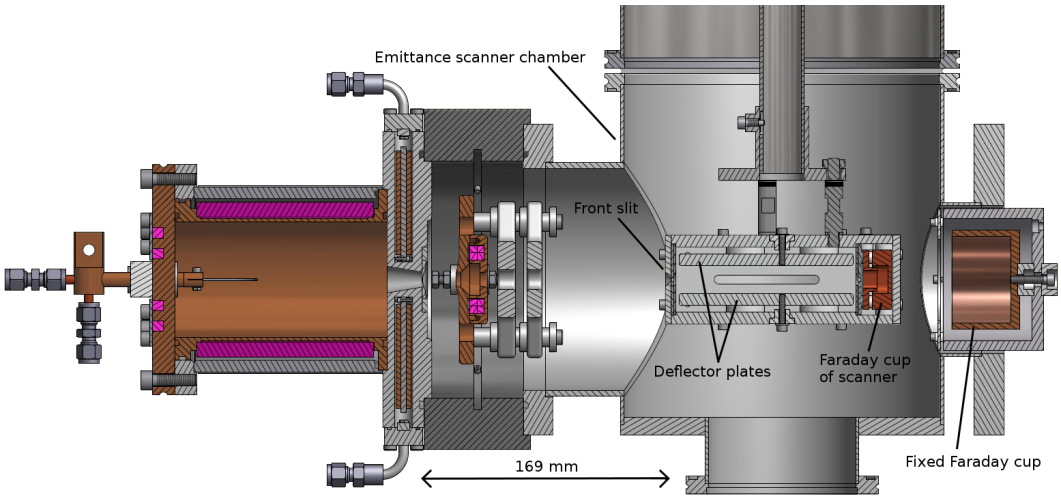

Figure 6.22: Cross-sectional view of the PELLIS ion source with the Allison-type emittance scanner attached in the orientation for (y, y') measurement.

to the optimal plasma meniscus shape. With higher or lower arc currents the plasma meniscus becomes concave and convex respectively, causing the beam emittance to grow. The location of the optimum shifts towards higher current with increasing ion source pressure. In figure 6.23b the same measured emittance data is shown as a function of the H$^-$ equivalent current $I_{H^-} + I_e\sqrt{m_e/m_{H^-}}$. There it can be seen that the beam emittance is defined by the equivalent current in these cases. If it is assumed that the plasma sheath dynamics is only dependent on the charge density near the plasma meniscus (assuming other factors to be constant), the simplest interpretation to the observation is that the ratio of electron to ion charge density near the plasma meniscus is

$$\frac{\rho_e}{\rho_{H^-}} = \frac{I_e}{I_{H^-}}\sqrt{\frac{m_e}{m_{H^-}}}. \tag{6.1}$$

The charge ratio only depends on the ratio of currents and mass ratio of the particles. This means that there are no variables that affect only electrons (or ions), i.e. the electron density coefficient R_{ec} is one. Another possibility is that R_{ec} is not unity and varies with pressure in such a way that the emittance curves in figure 6.23b coincide (such R_{ec} values are, for example, 1.8, 2.2, 3.0 and 5.0 for the 0.28 Pa, 0.44 Pa, 0.58 Pa and 0.85 Pa cases respectively). The semi-empirical R_{ec} parameter is representing physics of the electron transport from the plasma to the extracted beam. Thus, it includes the effects of electron diffusion in the magnetic filter field. Therefore it is to be expected that R_{ec} does not stay constant as pressure changes. The dependency of the emittance from the equivalent current is also observed in simulations (both for unity and non-constant R_{ec}). This happens because in the simulation model the plasma sheath dynamics is only dependent on the total charge density of the extracted beams. Also, the model does not treat the electrons differently from the ions inside the plasma as they do not experience the magnetic field.

In figure 6.24 the (x, x') rms emittance values measured with four different plasma-electrode to puller-electrode voltages with varying arc currents are shown as a function of measured H$^-$ current at 0.58 Pa source pressure. For each voltage there is a minimum emittance, which shifts towards higher H$^-$ current as the acceleration voltage is increased, which is the expected behaviour. A systematic study was made for matching the simulation results to the experimental data by adjusting the transverse ion temperature T_t and the electron density coefficient R_{ec} while other plasma model parameters were left to the values which are known to be typical for filament-driven multicusp ion sources. A good match was found with $T_t = 0.75$ eV and $R_{ec} = 3$.

For comparison purposes, the same fitting procedure was also made with PBGUNS code for the 5 kV puller case. The transverse ion temperature and stripping parameter (RHIN) were adjusted to find a match. The stripping parameter is intended for modelling H$^-$ loss in the extraction due to stripping collisions with background H_2 (reaction (3.39)), but in practice it increases the effective space charge in the plasma region. The effect is therefore equal to the IBSIMU electron density coefficient R_{ei}

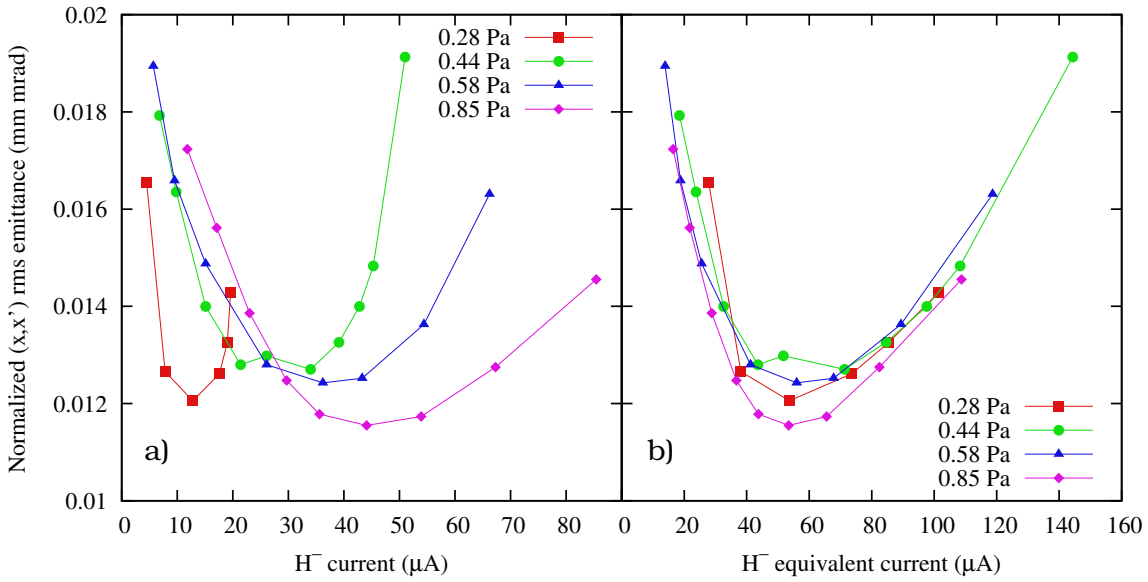

Figure 6.23: Measured beam rms emittance in the (x, x') plane a) as a function of beam current and b) as a function of H^- equivalent current (including electron beam) for different ion source gas pressures.

with the exception that PBGUNS stripping parameter changes the H^- charge density and R_{ei} modifies the electron charge density. With the e^-/H^- ratio of 20 used in these simulations the electron density coefficient $R_{ei} = 3$ gives the same effect as 48 % stripping of H^- would. This magnitude of stripping seems very improbable. A simple calculation with a linear slope of H_2 pressure from 0.5 Pa to zero in 10 mm distance from the ion source extraction aperture gives 10 % stripping. Therefore the magnetic field seems to be a more probable cause than stripping for the plasma density coefficient required for matching the simulations to the experiment. In PBGUNS the best fit was found with transverse ion temperature 2.5 eV and stripping parameter of 0.40.

The measured and simulated data are presented together in figure 6.24. The IBSIMU simulations are able to reproduce the measured beam emittances within ±10 % of each other at higher beam currents. At lower beam current levels the simulations overestimate the beam emittance especially with higher puller voltages. With PBGUNS a similar match was achieved, but the credibility of the simulations is diminished by the high value of the transverse temperature, which according to eq. (4.43) would correspond to 0.026 mm mrad rms emittance, i.e. 100 % higher than the simulation result. The transverse ion temperature of 0.75 eV used in IBSIMU fit corresponds to 0.014 mm mrad rms emittance, which is slightly larger than the simulated and observed beam emittances at the optimal current. This small difference results from the data thresholding.

Close to the optimum the beam formation is well reproduced in simulations. For

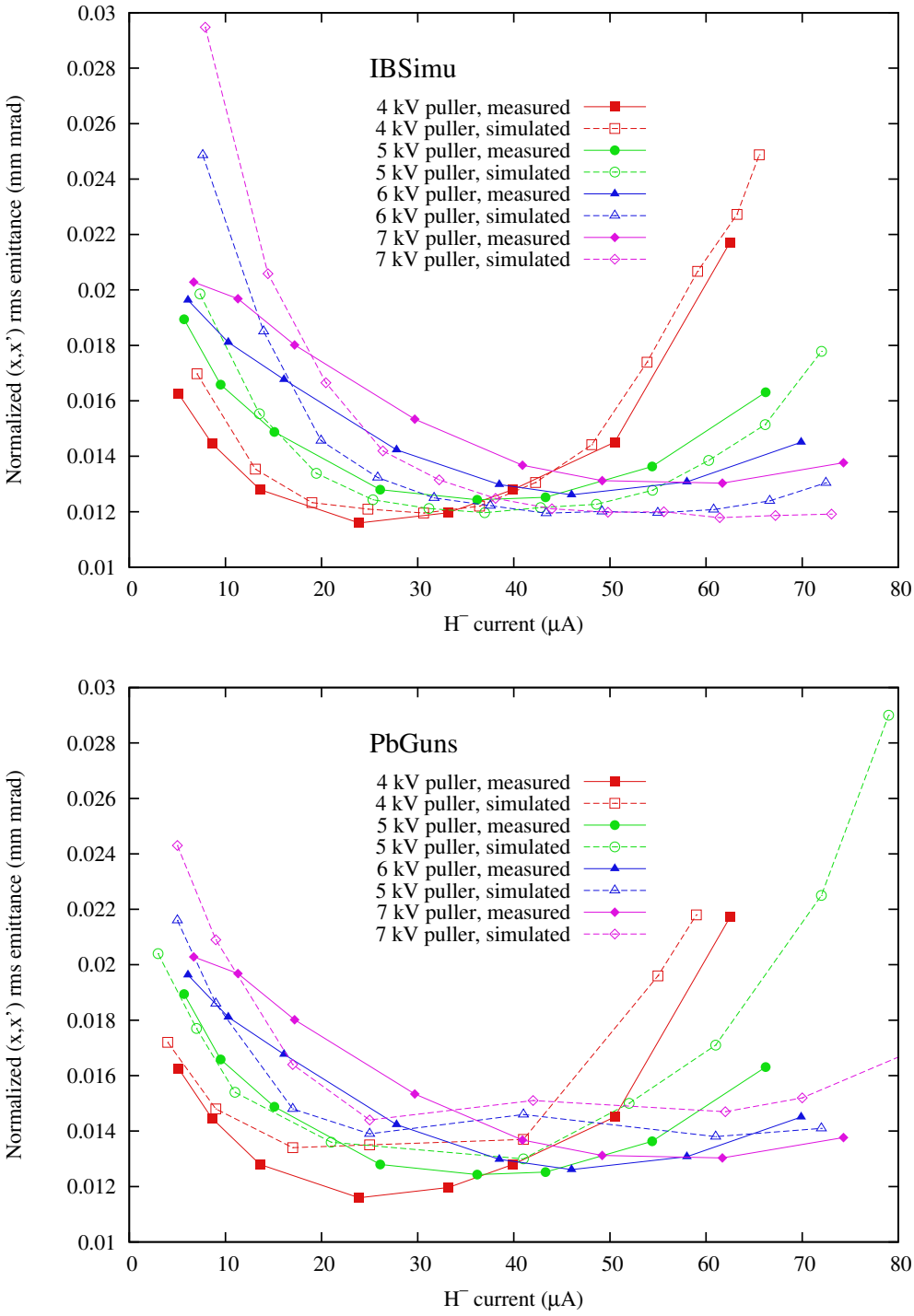

Figure 6.24: Measured and simulated beam rms emittances as a function of beam current for four different plasma-electrode to puller-electrode voltages. Measured and IBSimu-produced data are processed similarly with 95 % thresholding. Emittance data from PbGuns is presented as given by the program.

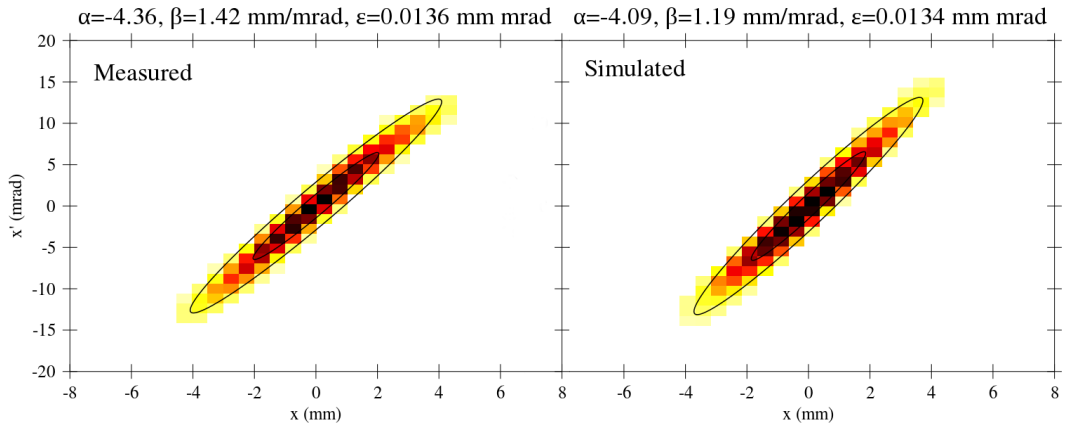

Figure 6.25: Measured and simulated (x, x') rms emittance patterns for 40 μA extracted H^- beam with 5 kV plasma-electrode to puller-electrode voltage and 1.3 mA of co-extracted electron current (corresponding to 0.58 Pa ion source pressure and 3.90 A arc current). Both data are processed similarly with 95 % thresholding.

example, similarly processed emittance patterns measured and simulated for the case with 5 kV plasma-electrode to puller-electrode voltage and 40 μA H^- and 1.3 mA electrons extracted (case for which simulation plot was presented figure 6.19) are presented in figure 6.25. In the cases close to the optimum and at higher currents not only the rms emittance value, but also the Twiss parameters of the emittance pattern are well reproduced, with the mismatch factor being 0.03–0.2. The average of mismatch factors at all measured data points shown in figure 6.24 is 0.26.

The measured (y, y') emittance values were smaller than (x, x') emittances by less than 4 %. The electron filter and electron dump magnetic fields do not seem to cause significant asymmetry to the beam. The slightly higher emittance in the electron dump bending direction is most likely caused by non-linear focusing forces as the beam passes the einzel lens slightly off-axis due to the electron dump magnetic field configuration.

According to the measurements the developed ion source can be used as a high brightness H^- injector over a wide range of required ion beam intensitity levels. The intensity at which the optimal emittance is achieved can be adjusted with ion source pressure and puller voltage. It is expected that smaller emittance values can be reached at low beam intensities by changing the plasma electrode aperture to a smaller one or by collimating the extracted beam if necessary. The presented system has been used successfully in several experiments at the JYFL Pelletron accelerator.

6.4 Design of the JYFL RF H$^-$ ion source

An agreement was made in 2006 between Finland and Russia to settle the former debt of USSR to Finland by goods and services. The two countries negotiated that as part of the debt, a MCC30/15 cyclotron was to be manufactured and installed at JYFL by the D. V. Efremov Institute, St. Petersburg, Russia. The device was delivered in August 2009 and approved for use in April 2010. The cyclotron accelerates up to 200 μA of 18–30 MeV H$^+$ and up to 60 μA of 9–15 MeV D$^+$ from negative ions with high-efficiency stripping extraction. The beams will be used for medical isotope production and nuclear physics experiments at the IGISOL facility. [174]

The cyclotron was delivered with a conventional filament-driven multicusp ion source for production of H$^-$ and D$^-$. The ion source is capable of continuous operation at 1 mA H$^-$ output for about 130 hours before filament failure. The ion source is located at 2.1 m from the accelerator within the cyclotron vault. The filament renewal can take about 12 hours because of the radiation safety limitations before access to ion source is possible. This kind of operation is not acceptable as 350 h and longer continuous experiments are expected once the facility is fully operational. Therefore a project for developing a CW 13.56 MHz *Radiofrequency Ion Source*, RADIS, for the cyclotron was initiated in March 2011. The goal of the RADIS project is to develop a new ion source to produce at least 1 mA of continuous H$^-$ beam or 500 μA of D$^-$ beam at the cyclotron injection energy of 19 keV, with a maintenance interval of at least one month.

The approach being studied for the RADIS uses a multicusp chamber with an external planar spiral RF antenna behind a flat AlN RF window on the back of the ion source. A similar approach has been studied at Seoul National University (SNU) with promising results [175] and it also allows initial tests to be made using existing TRIUMF-type, filament-driven multicusp H$^-$ ion source LIISA by replacing the back plate.

6.4.1 Initial testing with existing multicusp ion source

The studies have been started by using the LIISA ion source as a retrofitted test stand. Normally the source is used to inject H$^-$ at 5.9 keV injection energy to the laboratory K130 cyclotron [74]. The test stand beam energy is much lower than the design goal of RADIS, but it is sufficient for initial testing. The ion source filament back plate was replaced with a new RF back plate for the tests as shown in figure 6.26. The water-cooled flat RF antenna of the source is made from 6.35 mm diameter copper tubing and the antenna rounds are insulated from each other with 0.2 mm thick shrink tubing. The 5 kW CW RF power supply is coupled to the antenna using a capacitive

T network matching circuit. The RF power supply, matching network and the antenna are all at high voltage.

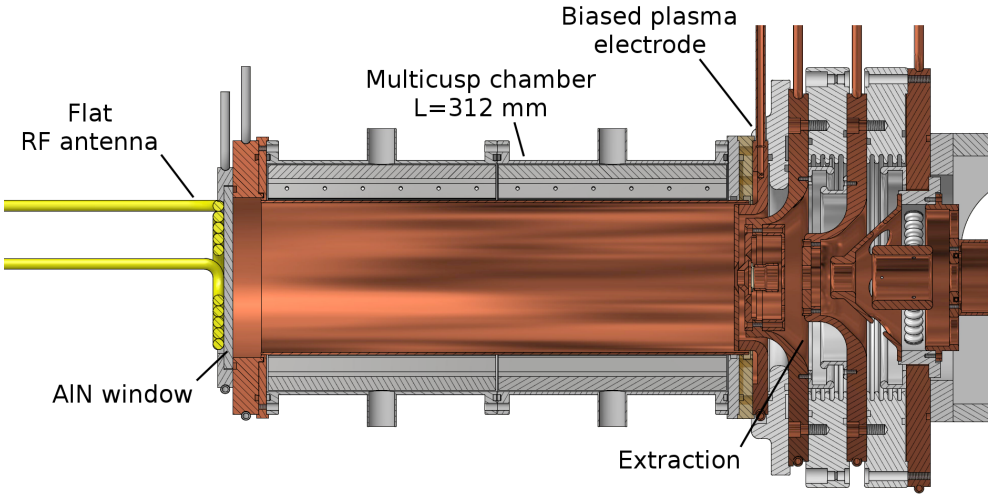

Figure 6.26: Cross-sectional view of the setup used for RF ion source testing.

Simulations of filament ion source extraction

The extraction of the LIISA ion source was simulated to gain understanding of the behaviour of the ion and electron beams to aid in interpretation of the experimental results. Simulations were first made for the extraction using the standard parameters for LIISA operation to verify the validity of the simulations. The following plasma parameters were used: plasma potential $\phi_P = 5$ V, electron to ion beam current ratio $R_{ei} = 3$–12, negative ion and electron transverse temperature $T_t = 0.5$ eV, positive ion temperature $T_p = 0.5$ eV, ratio of fast compensating positive ions to total negative charges $R_f = 0.5$, extracted negative ion beam current densities $J_{H^-} = 10$–20 A/m^2 and initial drift energy of extracted particles $E_0 = 3$ eV. These values are based on experimental data from operating the LIISA ion source and on published plasma parameters with similar ion sources [75]. With the typical electrode voltages the simulations show that the electron beam is dumped on the front surface of the puller electrode and not on the electron dump inside the puller electrode structure (see figure 6.27). This happens due to the highly concave plasma sheath and the magnetic filter field of the ion source. It seems likely that the electron dumping does not happen as the designer of the extraction has intended. The observations in the simulations were verified by investigating the marks left by the electron beam on the puller electrode during the years of beam production with these parameters (see figure 6.28). No marks were seen on the intended electron dump location. The observations made with the LIISA extraction have given confidence to the results given by the simulations with this extraction.

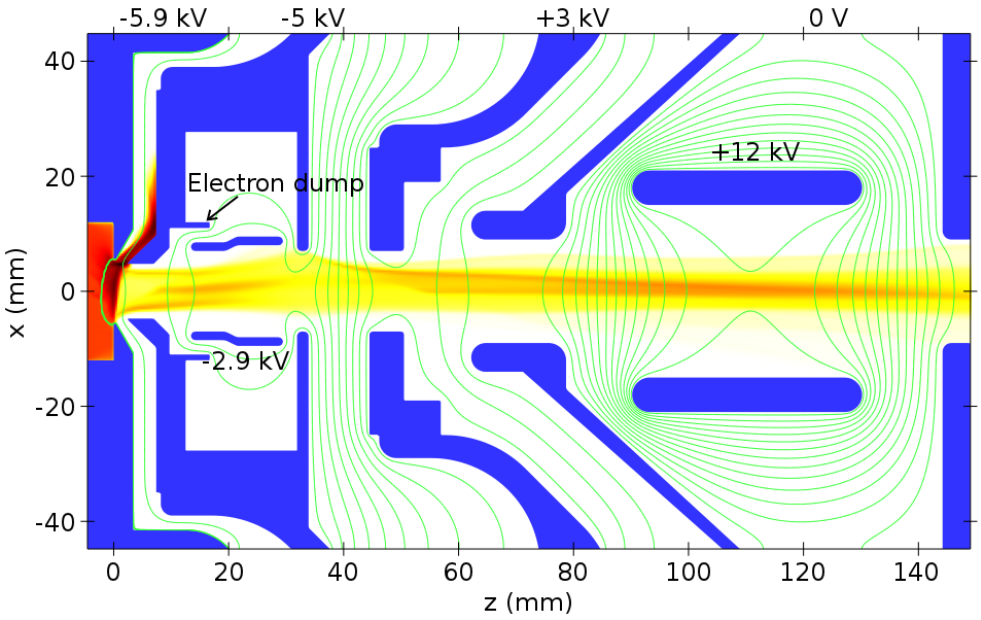

Figure 6.27: Simulation of LIISA extraction system with $J = 16$ A/m^2 and $R_{ei} = 6$. The electron beam is dumped to the front of the puller electrode and not the electron dump.

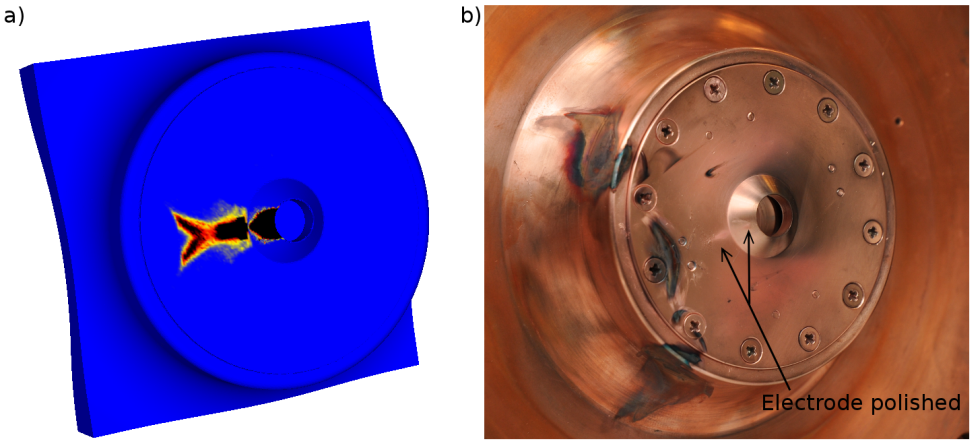

Figure 6.28: The power density distribution of the electron beam on the puller electrode according to simulation (a) has similarities with the marks left by the electron beam on puller electrode (polished regions and burn marks in photograph b).

Experiments with RF back plate

Initial testing with the LIISA ion source equipped with the RF back plate (configuration shown in figure 6.26) have been conducted. The tests have mostly been done with low RF power levels because operating the ion source, especially at RF power levels higher than 1 kW, causes faults in the central control system. It is suspected that this is due to high voltage sparking in the extraction, induced by higher co-extracted electron currents compared to filament-driven operation (e^-/H^- ratio has been about 100 in measurements while for typical run with filament back-plate the ratio is about 3–12). The highest intensity results with the test source have been 240 μA of H^- and 21 mA of electrons at 1500 W RF input (307 W reflected) with 15 V plasma-electrode bias and optimized pressure. The simulations with the RF driven plasma ($J = 2.5$ A/m^2 and $R_{ei} = 100$) show that also in this case the extracted electron beam is dumped on the puller electrode. It suspected that the cooling of the puller electrode may not be sufficient for handling heat loads of this magnitude for sustained periods of time. Therefore a more robust electron dump has been developed.

6.4.2 RADIS ion source and extraction

Based on the experiences in the initial tests, a completely new ion source chamber and extraction system have been designed and is being built. The new 127 mm long aluminum Modified MultiPole Structure (MMPS) [176] multicusp chamber, compatible with the existing RF back plate, has been built for RADIS and is shown in figure 6.29. The MMPS configuration of the chamber uses magnetic AISI 430 stainless steel strips to redirect the magnetic flux at the poles. The biggest plasma losses are at the magnetic poles and therefore the heat flow to the permanent magnets is smaller in MMPS compared to a conventional multicusp configuration, where magnets are located at the poles. The new chamber is going to be attached to a PELLIS-style front plate with an electromagnet filter field. The front plate is going to be electrically insulated from the plasma chamber to enable plasma-electrode biasing.

With the smaller plasma chamber, optimized filter field and plasma electrode bias and by being able to use higher RF power it is believed that H^- currents of up to 1 mA from a ⌀6 mm hole can be extracted (densities of up to 35 A/m^2). A new extraction system, which is capable of handling the expected 100 mA or more of co-extracted electron current and transporting the H^- beam to the following LEBT has been designed with IBSimu. The nominal plasma parameters used in the simulations were plasma potential $\phi_P = 5$ V, electron to ion beam current ratio $R_{ei} = 100$, negative ion and electron transverse temperature $T_t = 1.0$ eV, positive ion temperature $T_p = 0.5$ eV, ratio of fast compensating positive ions to total negative charges $R_f = 0.5$, extracted negative ion beam current density $J_{H^-} = 35$ A/m^2 and initial drift energy of extracted particles $E_0 = 3$ eV. Three dimensional simulation of the extraction system being

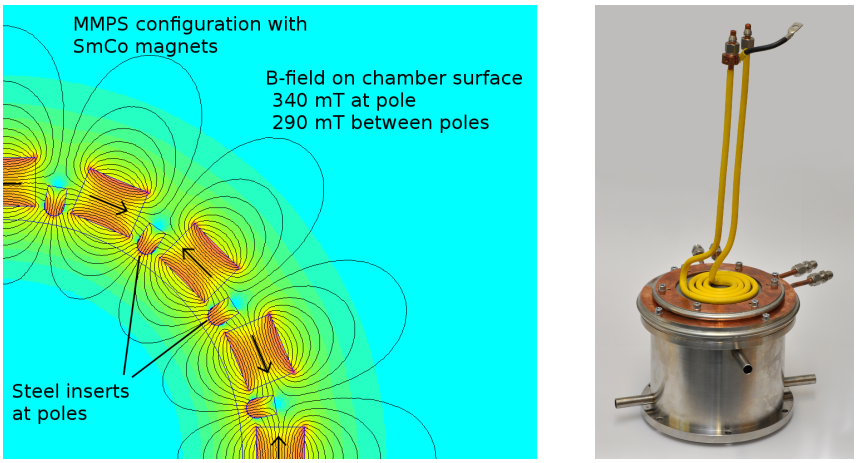

Figure 6.29: FEMM simulation image of the SmCo MMPS multicusp configuration on the left and photograph of the finished chamber with the RF back plate on the right.

developed is shown in figure 6.30. The simulations predict a normalized rms transverse emittance of 0.064 mm mrad at $z = 120$ mm (theoretical minimum according to eq. (4.43) is 0.049 mm mrad).

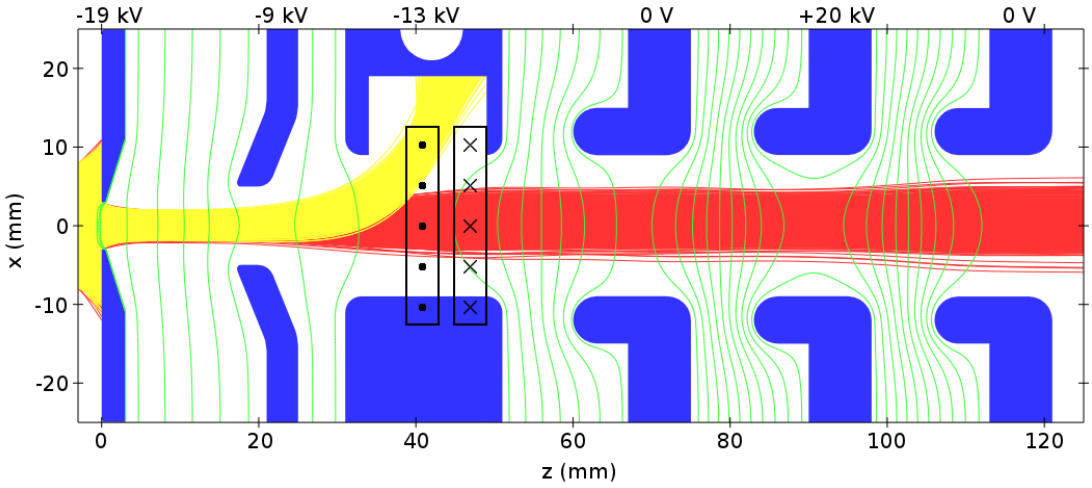

Figure 6.30: Three-dimensional simulation with 1 mA of H⁻ and 100 mA of electrons being extracted with the new extraction system. A parallel beam is achieved with the shown electrode voltages.

The extraction uses a similar electron dumping scheme that has been planned to be used at SNS [9] and is being tested at CERN Linac4 [90, 170]. The new extraction is going to have an adjustable voltage on puller electrode for experimental matching to the plasma density for optimum beam quality. The electron dumping will be performed on the following decelerating einzel lens by a transverse magnetic field. The ion beam deflection is compensated by an anti-parallel magnetic field. The magnetic fields are

constructed using SmCo magnets embedded inside the einzel lens. The electron beam dumping is performed nominally at 6 keV energy leading to about 600 W of heat being dumped on the electrode at 100 mA electron current. The peak power density on the electron dump surface is about 90 W/mm^2 according to simulations as shown in figure 6.31. The einzel lens is cooled with ⌀8 mm water channel 3 mm away from the dump surface. Thermal and fluid mechanics simulations have been made to verify that the SmCo magnets stay cool enough to avoid demagnetization. The electron dump einzel lens is followed by a grounded electrode and another accelerating einzel lens for adjusting the beam focusing and for enabling space charge compensation in the following beam line. The extraction presented here has also been used as a test problem in the previous chapter using the nominal plasma parameters mentioned above.

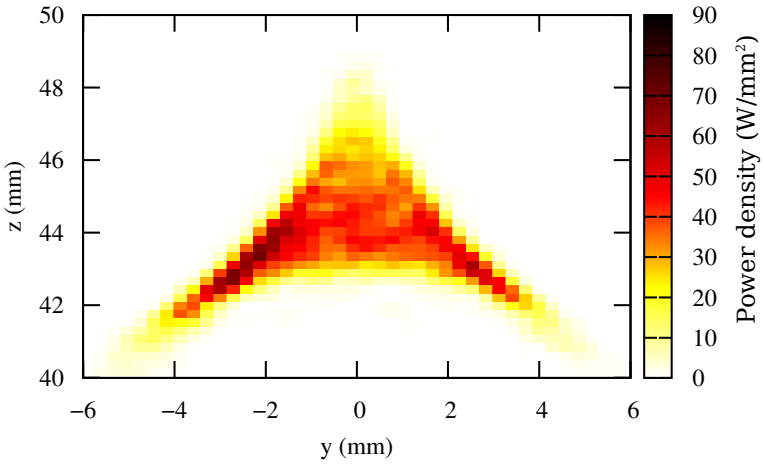

Figure 6.31: Power distribution on the electron dump surface from 100 mA electron beam.

The experimental work with the RADIS ion source and extraction is on-going during the writing of this thesis in spring and summer months of 2013 [1].

[1] A 1 mA H^- beam has been produced with 3200 W RF power and extracted from the ion source at 7.5 keV energy together with 27 mA of electrons.

Chapter 7

Conclusions

The use of ion extraction simulation software plays an important role in ion source development. The codes are the main tool for designing new systems and they are also used in analyzing and improving existing hardware. Especially in the case of negative ion extraction the modelling needs to be done in three-dimensional domain because of the asymmetry created by co-extracted electron dumping. Several examples of such work were presented in the previous chapter. The early work with the Texas A&M University H^- ion source suggested that this type of code could be used for modelling negative ion extraction systems successfully. The SNS baseline case provided a more complicated, higher current density system to model and measured emittance data to compare against. The emittance values were well reproduced in simulations in the typical operating parameter range, where the current density is higher than optimum. The main cause for the high beam emittance from the ion source was verified as the highly convex plasma sheath. A proposed new electrostatic extraction for SNS was also studied, which is intended to provide higher beam intensities at lower emittance to the SNS RFQ accelerator in the future.

The PELLIS ion source developed at JYFL was intended for low-emittance beam production. Therefore it was systematically characterized with current measurements and emittance scans to find the parameters for optimum beam production. The data was also used for making thorough comparisons between experiments and simulations allowing one to estimate the accuracy of predictions given by the simulations. The transverse ion temperature and the electron density coefficient were fitted to match the simulations to experimental data while other plasma parameters were fixed to values which are typical for filament-driven multicusp ion sources. The simulated emittance values achieved this way are within ± 10 % of the experimental values at flat and convex sheath conditions. This can be considered as a good match. At concave plasma sheath conditions the simulations predict higher emittance than what is observed. The reason for the discrepancy is not obvious. It is possibly due to an effect in the vicinity of plasma sheath (or presheath), which is not being modelled

correctly by the simulations. One such effect, which may cause this deviation is the variation of the current density and incorrect angular distribution of the particle flux arriving to the plasma sheath as the local slope of the sheath changes in these simulations. This results from the planar definition of the beam flux at the simulation boundary and is illustrated in figure 7.1. In case of highly concave plasma sheath, this effect may result in increased emittance compared to the case where beam would be formed by acceleration perpendicular to the sheath from a uniform plasma. The same phenomenon may also cause artefacts in the convex plasma sheath case, even if no evidence of it was observed in this comparison.

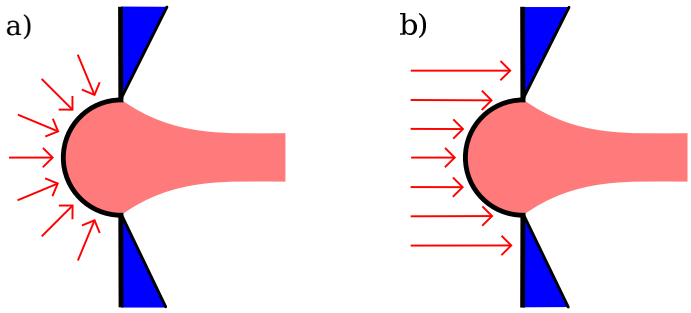

Figure 7.1: Schematic illustration of beam flux arriving to the plasma sheath a) perpendicular to the sheath from a uniform plasma surrounding the sheath and b) as a planar flux from artificial presheath condition used in the simulations. Use of non-zero transverse temperature of the beam mitigates the effects of the planar flux in real simulations.

In the PELLIS case, the best simulation match is achieved with an electron density coefficient R_{ec} of 3. This is very high compared to the SNS case in which a good agreement between simulated emittance and experiment was found with $R_{ec} = 1$ (see figure 6.12). In both cases there is a significant magnetic field in the plasma sheath region, but there are also significant differences. The extracted H^- current density, for example, is two orders of magnitude higher in the SNS case. The dynamics of the electrons near the sheath is dependent not only on the magnetic field, but on the combination of many phenomena which are not taken into account by the plasma model used in this work.

The reasons for the deviation at low plasma density and the phenomena affecting the observations, which are explained in this work by the electron density coefficient R_{ec} require further study. More information about the beam formation can be acquired, for example, with systematic emittance measurements at different e^-/H^- ratios at constant pressure, achieved by adjusting the magnetic filter field on the PELLIS ion source. Another experimental study to be made is a comparison of H^+ and H^- beam emittances of the PELLIS ion source.

The beam formation is also going to be investigated by using PIC simulations capable

of including the presheath area, modelling collisions and tracking the electron trajectories correctly in the magnetic filter field. The PIC simulations are also capable of modelling the beam formation self-consistently with an arbitrary potential distribution in the plasma. The assumption of the non-existence of the potential saddle-point in the extraction is the most fundamental limiting assumption in the negative ion plasma extraction model used in this work. Hopefully as a result of PIC simulation studies, a new more refined plasma model could be developed for the gun-type codes in the future.

Taken together, the results suggest that three-dimensional gun-type simulation codes such as the one described in this work can be used for modelling and designing new systems with relatively high confidence. Still, extraction system designs should be made intelligently to have enough adjustability to adapt to differences between modelling and reality, and variations in day-to-day operations of the plasma devices. The designs should also avoid being dependent on highly sensitive plasma parameters in cases where well trusted data is not available. Despite the shortcomings of the gun-type codes they have their place in the design process of high-space-charge plasma extraction systems as alternative methods can not be used for optimization of geometries and voltages with parametric scanning due to their computational inefficiency.

The IBSimu code developed in this work has already achieved a position among the most used gun-type extraction software. The code has been used in at least 17 laboratories or companies for ion source extraction modelling. Even though the code is publicly available it is not to be considered as a ready-made product but rather as an open research project, which in the same time provides tools for the community. The next planned major step in the code development is to implement a possibility for having a fine mesh region near the plasma sheath area, which would be solved together with the rest of the mesh without additional approximations. This feature would allow studying of systems with small plasma electrode apertures without tricks used in the PELLIS case. It would also improve the accuracy of modelling in all cases because the modelling is most sensitive to mesh-induced artefacts near the plasma sheath.

Due to the open nature of IBSimu the users of the code can implement new features and methods in the code to solve their specific problems, which can not be investigated with the existing capabilities of the code. Examples of such work include modelling of the erosion of the BNL magnetron cathode by the backstreaming positive ions formed near the extraction by ionization of the residual gas [177] and modelling of the CERN Linac4 LEBT space charge compensation [178]. The availability of the source code also promotes openness of research. IBSimu is not a "black box" tool like most of the other extraction codes. The methods of the code are not only described in this work on a general level, but also the details of the implementation are available in the form of open source code.

Appendix A

List of commonly used symbols

For reference purposes a list of commonly used symbols used in this work is presented here with the typical unit (and value if applicable) in parenthesis. The input parameters of the IBSimu code are listed separately in appendix B.

ϵ_0	Permittivity of free space ($8.85418782 \cdot 10^{-12}$ m^{-3} kg^{-1} s^4 A^2)
k	Boltzmann constant ($1.3806488 \cdot 10^{-23}$ J/K)
e	elementary charge ($1.60217657 \cdot 10^{-19}$ C)
c	speed of light ($2.99792458 \cdot 10^8$ m/s)
x, y, z	spatial coordinates (m)
x', y'	tangents of inclination angle of a particle trajectory (mrad)
v	velocity (m/s)
p	momentum (kg m/s)
m	mass (kg)
q	charge (C)
Q	charge state
E_K	kinetic energy (J)
T	temperature (K)
n	particle density (m^{-3})
λ_D	Debye length (m)
ν	collision frequency (s^{-1})

ϵ	emittance (mm mrad)
σ	cross section (m^2)
F	force (kg m s^{-2})
ϕ	potential (V)
V	voltage of a conducting entity (V)
$\vec{E}$	electric field (V/m)
$\vec{B}$	magnetic flux density (T)
ρ	space charge density (C/m^3)

Appendix B

Input parameters of the simulation code

B.1 Negative plasma model parameters

The input parameters for the negative ion extraction plasma model are listed here with the unit used in the code. For a detailed description of the plasma model, see section 5.2.

ϕ_P	plasma potential (V)
ϕ_{Bsup}	magnetic field suppression threshold potential (V)
ϕ_{ec}	electron density coefficient threshold potential (V)
T_e	transverse electron temperature (eV)
T_t	transverse ion temperature (eV)
T_p	temperature of the thermal compensating positive ion population* (eV)
J	current density of particle flux (A/m^2)
E_0	initial drift energy of extracted particles (eV)
R_{ei}	electron to ion beam current ratio
R_f	ratio of fast compensating positive ions to total negative charges
R_{ec}	electron density coefficient

* Several thermal species can be defined in the plasma model, but in this work only one has been used. Therefore it is sufficient to represent the temperature with a single value T_p and no parameter is needed for charge fractions of the species.

B.2 Other parameters

In addition to the plasma parameters, also other parameters need to defined to run a simulation. The most important parameters needed are listed here.

h	grid step size (m)
n_p	number of particles per grid cell
α	space charge under-relaxation factor
$\epsilon_{\text{Poisson}}$	accuracy requirement for Poisson solver
ϵ_{part}	accuracy requirement for particle iterator

Appendix C

Methods specific for two dimensional systems

Many systems that are simulated do not require fully three-dimensional simulations. In extraction and beam transport, two types of systems are commonly encountered for which the dimensionality of the simulations can be reduced: slit beam systems and cylindrically symmetric systems.

C.1 Slit beam systems

Geometries, which have no variation in one linear direction can be described fully with Cartesian (x, y) coordinates. Strictly speaking such systems do not exist, but the two dimensional description can be used as an approximation of the real system. In some ion sources the beam is extracted through a slit in the plasma electrode. If everything in the modelled extraction has the same symmetry the center of the slit beam extraction ($z = 0$) can be modelled just by using (x, y) coordinates. In practise this is a good approximation in systems with slit length-to-width ratio of 10 or higher.

The 2D simulations of slit beam systems use very similar methods to the 3D simulations: in most methods the 2D procedure is like the 3D counterpart — the methods just neglect the z-coordinate. The only significant difference with the 2D simulations is that the simulated particle trajectories are not localized in z-direction. Each particle represents an infinitely long line of beam and therefore the current they carry is measured in A/m. Because the particles have no location or velocity in z-direction the magnetic field components B_x and B_y have to be zero in this approximation. The B_z can be nonzero and it will cause bending of charged particles in (x, y) plane.

In most cases with slit beam systems 2D simulations can be used for initial design

work. Before final design the effects of the slit ends should be studied and this work has to be done with a 3D code.

C.2 Cylindrically symmetric systems

Cylindrically symmetric geometries are abundant in extraction systems — in a vast majority of systems the ion beam is extracted from a round plasma electrode aperture and in many cases the whole system is cylindrically symmetric with the exception of the mechanical mounting of electrodes. Even if the system requires three dimensional modelling due to asymmetry, initial work can often be done by assuming full cylindrical symmetry.

C.2.1 FDM formulation of Poisson equation

In modelling cylindrical symmetric systems the cylindrical coordinate system (z, r, θ) is used with θ being omitted due to the symmetry. The computation nodes are defined as

$$(z_i, r_j) = (z_{\min} + h \cdot i,\ h \cdot j), \tag{C.1}$$

where the grid line $j = 0$ is selected as the symmetry axis $r = 0$. In cylindrical symmetry, where $\frac{\partial \phi}{\partial \theta} = 0$ the Poisson equation becomes

$$\frac{1}{r}\frac{\partial \phi}{\partial r} + \frac{\partial^2 \phi}{\partial r^2} + \frac{\partial^2 \phi}{\partial z^2} = -\frac{\rho}{\epsilon_0}. \tag{C.2}$$

Off-axis ($r \neq 0$), this can be directly discretized as

$$\left(1 + \frac{1}{2j}\right)\phi_{i,j-1} + \left(1 - \frac{1}{2j}\right)\phi_{i,j+1} + \phi_{i-1,j} + \phi_{i+1,j} - 4\phi_{i,j} = -h^2\frac{\rho}{\epsilon_0} + O(h^2). \tag{C.3}$$

On the symmetry axis a formulation is required, which is valid at $j = 0$. To find such expression, a limit of (C.2) is taken as $r \to 0$. By using Bernoulli-L'Hôpital rule, the first term

$$\lim_{r \to 0} \frac{1}{r}\frac{\partial \phi}{\partial r} = \frac{\partial^2 \phi}{\partial r^2}. \tag{C.4}$$

The resulting expression

$$2\frac{\partial^2 \phi}{\partial r^2} + \frac{\partial^2 \phi}{\partial z^2} = -\frac{\rho}{\epsilon_0}. \tag{C.5}$$

can then be discretized as

$$2\phi_{i,-1} + 2\phi_{i,+1} + \phi_{i-1,0} + \phi_{i+1,0} - 6\phi_{i,0} = -h^2\frac{\rho}{\epsilon_0} + O(h^2), \tag{C.6}$$

where $\phi_{i,-1} = \phi_{i,+1}$ can be substituted because on the axis $\frac{\partial\phi}{\partial r}(r=0) = 0$. The finite difference formula for the axis becomes

$$4\phi_{i,+1} + \phi_{i-1,0} + \phi_{i+1,0} - 6\phi_{i,0} = -h^2\frac{\rho}{\epsilon_0} + O(h^2). \tag{C.7}$$

Similarly to the 3D case, finite difference formulas for the Neumann boundary nodes and near-solid nodes are constructed.

C.2.2 Particle calculation

In cylindrically symmetric simulations each particle represents a ring of beam carrying a specific current. In most simulations, where a uniform beam with radius $\tilde{r}$ is defined, the beam is defined as N_p macro particles each starting at radii $r_i = \tilde{r}\frac{i-0.5}{N_p}$, where $1 \leq i \leq N_p$. The current of each macro particle is chosen to achieve uniform beam. Therefore, the current of macro particle i is given by

$$I_i = \frac{2\pi r_i dr}{\pi\tilde{r}^2} = \frac{2r_i}{\tilde{r}N_p}. \tag{C.8}$$

The particle coordinates used in calculating the trajectories in cylindrical symmetry are (z, v_z, r, v_r, ω). Each particle is a ring and therefore has no location θ, but the azimuthal velocity $v_\theta = r\omega$ is needed to properly model the effects of finite transverse beam temperature [145]. In early extraction codes the azimuthal velocity was neglected, which resulted in over-estimation of space charge and under-estimation of the beam transverse temperature close to the axis. The particle propagation in cylindrically symmetric systems is defined by the Lorentz force law formulated as a system of ordinary differential equations [179]:

$$\frac{dz}{dt} = v_z \tag{C.9}$$

$$\frac{dr}{dt} = v_r \tag{C.10}$$

$$\frac{dv_z}{dt} = a_z = \frac{q}{m}(E_z - r\omega B_r) \tag{C.11}$$

$$\frac{dv_r}{dt} = a_r + r\omega^2 = \frac{q}{m}(E_r + r\omega B_z) + r\omega^2 \tag{C.12}$$

$$\frac{d\omega}{dt} = \frac{1}{r}\left(a_\theta - 2\frac{dr}{dt}\omega\right) = \frac{1}{r}\left(\frac{q}{m}(v_z B_r - v_r B_z) - 2\frac{dr}{dt}\omega\right) \tag{C.13}$$

in the non-relativistic approximation.

The transverse (projectional) emittance data in (x, x') coordinates is calculated from cylindrical coordinate data by rotating each trajectory point on the emittance plane

arond the axis with N_{rot} steps. The (x, x') emittance is therefore given by expectation values

$$\langle x^2 \rangle = \frac{1}{I_{\text{tot}}} \sum_{i=1}^{N_p} \sum_{j=1}^{N_{\text{rot}}} x_{ij}^2 \frac{I_i}{N_{\text{rot}}} \tag{C.14}$$

$$\langle x'^2 \rangle = \frac{1}{I_{\text{tot}}} \sum_{i=1}^{N_p} \sum_{j=1}^{N_{\text{rot}}} x'^2_{ij} \frac{I_i}{N_{\text{rot}}} \tag{C.15}$$

$$\langle x x' \rangle = \frac{1}{I_{\text{tot}}} \sum_{i=1}^{N_p} \sum_{j=1}^{N_{\text{rot}}} x_{ij} x'_{ij} \frac{I_i}{N_{\text{rot}}}, \tag{C.16}$$

where

$$x_{ij} = r_i \sin\left(\frac{2\pi j}{N_{\text{rot}}}\right) \tag{C.17}$$

$$x'_{ij} = \frac{v_{r,i}}{v_{z,i}} \sin\left(\frac{2\pi j}{N_{\text{rot}}}\right) + \frac{v_{\theta,i}}{v_{z,i}} \cos\left(\frac{2\pi j}{N_{\text{rot}}}\right) \tag{C.18}$$

and I_i is the current carried by particle i.

Bibliography

[1] E. O. Lawrence and M. S. Livingston, *The production of high speed light ions without the use of high voltages*, Plasma Rev. **40**, 19 (1932).

[2] R. M. Jones, *Accelerators for America's Future*, U.S. Department of Energy Report, October 26, 2009.

[3] P. Heikkinen and E. Liukkonen, *Cyclotron development program at Jyväskylä*, Proc. of the 16th International Conference on Cyclotrons and Their Applications, East Lansing, Michigan, USA, 2001, p. 89 (`http://www.jacow.org/`).

[4] G. I. Dimov, INP Novosibirsk Preprint, No. 304, 1969.

[5] R. J. Van de Graaff, *Tandem electrostatic accelerators*, Nucl. Instrum. Meth. **8**, 195 (1960).

[6] R. Hemsworth, H. Decamps, J. Graceffa, B. Schunke, M. Tanaka, M. Dremel, A. Tanga, H. P. L. De Esch, F. Geli, J. Milnes, T. Inoue, D. Marcuzzi, P. Sonato, and P. Zaccaria, *Status of the ITER heating neutral beam system*, Nucl. Fusion **49**, 045006 (2009).

[7] T. Kalvas, O. Tarvainen, T. Ropponen, O. Steczkiewicz, J. Ärje, and H. Clark, *IBSimu: A three-dimensional simulation software for charged particle optics*, Rev. Sci. Instrum. **81**, 02B703 (2010).

[8] T. Kalvas, O. Tarvainen, H. Clark, J. Brinkley, and J. Ärje, *Application of 3D code IBSimu for designing an H^-/D^- extraction system for the Texas A&M facility upgrade*, 2nd International Symposium on Negative Ions, Beams and Sources, Takayama, Japan, AIP Conf. Proc. **1390**, 150 (2011).

[9] T. Kalvas, R. F. Welton, O. Tarvainen, B. X. Han, and M. P. Stockli, *Simulation of H^- ion source extraction systems for the Spallation Neutron Source with IBSimu*, Rev. Sci. Instrum. **83**, 02A705 (2012).

[10] T. Kalvas, O. Tarvainen, J. Komppula, M. Laitinen, T. Sajavaara, H. Koivisto, A. Jokinen, and M. P. Dehnel, *Recent negative ion source activity at JYFL*,

3rd International Symposium on Negative Ions, Beams and Sources, Jyväskylä, Finland, AIP Conf. Proc. **1515**, 349 (2013).

[11] T. Kalvas, *Beam extraction and transport*, To be published in the *CAS — CERN Accelerator School: Ion Sources*, 29 May – 8 June, 2012 Senec, Slovakia.

[12] H. M. Mott-Smith, *History of Plasmas*, Nature **233**, 219 (1971).

[13] J. A. Bittencourt, *Fundamentals of plasma physics*, 3rd edition, Springer Science + Business Media, LLC, 2004.

[14] P. Debye and E. Hückel, *Zur Theorie der Elektrolyte. I. Gefrierpunktserniedrigung und verwandte Erscheinungen*, Physik Z. **24**, 185 (1923).

[15] H. Tawara, Y. Itikawa, H. Nishimura, M. Yoshino, *Cross sections and related data for electron collisions with hydrogen molecules and molecular ions*, J. Phys. Chem. Ref. Data **19**, 617 (1990).

[16] R. J. Goldston and P. H. Rutherford, *Introduction to plasma physics*, IOP Publishing Ltd, London, 1995.

[17] K. U. Riemann, *The Bohm criterion and sheath formation*, J. Phys D. **24**, 493 (1991).

[18] D. Bohm, *Minimum ionic kinetic theory for a stable sheath* in *The Characteristics of Electrical Discharges in Magnetic Fields*, edited by A. Guthrie and R. K. Wakerling, McGraw-Hill, New York, pp. 77–86, 1947.

[19] B. N. Chapman, *Glow discharge processes*, John Wiley & Sons Inc, 1980.

[20] M. A. Lieberman and A. J. Lichtenberg, *Principles of plasma discharges and materials processing*, John Wiley & Sons Inc, 2005.

[21] T. Morishita, M. Ogasawara, and A. Hatayama, *Estimate of cusp loss width in multicusp negative ion source*, Rev. Sci. Instrum. **69**, 968 (1998).

[22] R. A. Bosch and R. L. Merlino, *Confinement properties of a low-beta discharge in a spindle cusp magnetic field*, Phys. Fluids **29**, 1998 (1986).

[23] A. Kumar and V. K. Senecha, *Cusp loss width in multicusp negative ion source: A rigorous mathematical treatment*, 2nd International Symposium on Negative Ions, Beams and Sources, Takayama, Japan, AIP Conf. Proc. **1390**, 113 (2011).

[24] A. Fukano, T. Mizuno, A. Hatayama, and M. Ogasawara, *Estimation of the cusp loss width in negative-ion sources*, Rev. Sci. Instrum. **77**, 03A524 (2006).

[25] K. Tsumori, H. Nakano, M. Kisaki, K. Ikeda, K. Nagaoka, M. Osakabe, Y. Takeiri, O. Kaneko, M. Shibuya, E. Asano, T. Kondo, M. Sato, S. Komada, and H. Sekiguchi, *Polar distribution of ions and electrons in extracted region of a large-scaled caesium seeded ion source*, 3rd International Symposium on Negative Ions, Beams and Sources, Jyväskylä, Finland, AIP Conf. Proc. **1515**, 149 (2013).

[26] T. Sakurabayashi, A. Hatayama, and M. Bacal, *Effects of a weak transverse magnetic field on negaative ion transport in negative ion sources*, J. Appl Phys **95**, 3937 (2004).

[27] W. C. Martin, A. Musgrove, S. Kotochigova, and J. E. Sansonetti, *Ground Levels and Ionization Energies for the Neutral Atoms* (version 1.3, 2011). National Institute of Standards and Technology, Gaithersburg, MD.

[28] M. B. Shah, D. S. Elliott, and H. B. Gilbody, *Pulsed crossed-beam study of the ionisation of atomic hydrogen by electron impact*, J. Phys B. **20**, 3501 (1987).

[29] E. Krishnakumar and S. K. Srivastava, *Electron correlation effects in the dissociative ionization of H_2*, J. Phys. B **27**, L251 (1994).

[30] M. B. Shah, D. S. Elliott, P. McCallion, and H. B. Gilbody, *Single and double ionisation of helium by electron impact*, J. Phys B **21**, 2751 (1988).

[31] W. R. Thompson, M. B. Shah, and H. B. Gilbody, *Single and double ionization of atomic oxygen by electron impact*, J. Phys. B **28**, 1321 (1995).

[32] L. Calabretta, D. Rifuggiato, and V. Shchepounov, *High intensity proton beams from cyclotrons for H_2^+*, Proc. of the 1999 Particle Accelerator Conference, New York, USA, 1999, pp. 3288–3290 (`http://www.JACoW.org/`).

[33] L. Calabretta, L. Celona, S. Gammino, D. Rifuggiato, G.Ciavola, M. Maggiore, L. A. C. Piazza, J. R. Alonso, W. A. Barletta, A. Calanna, and J. M. Conrad, *Preliminary design study of high-power H_2^+ cyclotrons for the DAEδALUS experiment*, arXiv:1107.0652v1, 2011.

[34] D. R. Lide (ed), *CRC Handbook of Chemistry and Physics*, 84th Edition, CRC Press, 2003.

[35] R. Geller, *Electron cyclotron resonance ion sources and ECR plasmas*, Institute of Physics Pub., 1996.

[36] R. Becker, *Electron beam ion sources and traps*, Rev. Sci. Instrum **71**, 816 (2000).

[37] I. G. Brown, *The Physics and Technology of Ion Sources*, 2nd edition, Wiley-VCH Verlag GmbH & Co, Weinheim, 2004.

Bibliography

[38] B. Wolf, *Handbook of ion sources*, CRC Press, 1995.

[39] G. I. Kuznetsov, *IrCe cathodes for EBIS*, 9th International Symposium on Electron Beam Ion Sources and Traps, J. Phys. Conf. Series **2**, 35 (2004).

[40] C. J. Smithells, *Metal reference Book, Vol III*, Butterworths, London, 1967.

[41] H. B. Michaelson, *The work function of the elements and its periodicity*, J. Appl. Phys. **48**, 4729 (1977).

[42] G. Rouleau, E. Geros, J. Stelzer, E. Chacon-Golcher, R. Keller, et al., *Tungsten filament material and cesium dynamic equilibrium effects on a surface converter ion source*, Rev. Sci. Instrum. **79**, 02A514 (2008).

[43] P. C. Thonemann, *High-Frequency Discharge as an Ion Source* Nature **158**, 61 (1946).

[44] T. Schenkel, J. W. Staples, R. W. Thomae, J. Reijonen, R. A. Gough, K. N. Leung, R. Keller, R. Welton, and M. Stockli, *Plasma ignition schemes for the Spallation Neutron Source radio-frequency driven H^- source*, Rev. Sci. Instrum. **73**, 1017 (2002).

[45] R. F. Welton, M. P. Stockli, Y. Kang, M. Janney, R. Keller, et at., *Ion source antenna development for the Spallation Neutron Source*, Rev. Sci. Instrum. **73**, 1008 (2002).

[46] J. Peters, *The new HERA H^- RF volume source*, Proc. of the 21st Linear Accelerator Conference, Gyeongju, Korea, 2002, pp. 422–424 (`http://www.JACoW.org/`).

[47] M. A. Lieberman, *Principles of plasma discharges*, lecture notes, University of California, Berkeley, 2003.

[48] J. Staples and T. Schenkel, *High-efficiency matching network for RF-driven ion sources*, Proc. of the 19th Particle Accelerator Conference, Chicago, USA, 2001, pp. 2108–2110 (`http://www.JACoW.org/`).

[49] C. Lyneis, D. Leitner, M. Leitner, C. Taylor, and S. Abbott, *The third generation superconducting 28 GHz electron cyclotron resonance ion source VENUS*, Rev. Sci. Instrum. **81**, 02A201 (2010).

[50] T. Andersen, H. K. Haugen, and H. Hotop, *Binding Energies in Atomic Negative Ions: III*, J. Phys. Chem. Ref. Data **28**, 1511 (1999).

[51] S. G. Bratsch, *Electron Affinities of the Lanthanides*, Chem. Phys. Lett. **98**, 113 (1983).

[52] S. G. Bratsch and J. J. Lagowski, *Electron Affinities of the Actintides*, Chem. Phys. Lett., **107**, 136 (1984).

[53] J. Heinemeier and P. Hvelplund, *Production of 15–90 keV negative heavy ions by charge exchange with Mg vapour*, Nucl. Instrum. Meth. **148**, 65 (1978).

[54] D. J. Nicholas, C. W. Trowbridge, and W. D. Allen, *Lifetime of a Negative Helium Ion*, Phys. Rev. **167**, 38 (1968).

[55] A. S. Schlachter, D. H. Loyd, P. J. Bjorkholm, L. W. Anderson, and W. Haeberli, *Charge-Exchange Collisions Between Helium Ions and Cesium Vapor in the Energy Range 1.5–25 keV*, Phys. Rev. **174**, 201 (1968).

[56] M. Bacal, *Physics basis and future trends for negative ion sources*, Rev. Sci. Instrum. **79**, 02A516 (2008).

[57] P. Vankan, D. C. Schram, and R. Engeln, *High rotational excitation of molecular hydrogen in plasmas*, Chem, Phys. Lett. **400**, 196 (2004).

[58] R. I. Hall, I. Čadež, M. Landau, F. Pichou, and C. Schermann, *Vibrational Excitation of Hydrogen via Recombinative Desorption of Atomic Hydrogen Gas on a Metal Surface*, Phys. Rev. Lett. **60**, 337 (1988).

[59] M. Capitelli, M. Cacciatore, R. Celiberto, O. De Pascale, P. Diomede, F. Esposito, A. Gicquel, C. Gorse, K. Hassouni, A. Laricchiuta, S. Longo, D. Pagano, and M. Rutigliano, *Vibrational kinetics, electron dynamics and elementary processes in H2 and D2 plasmas for negative ion production: modelling aspects*, Nucl. Fusion **46**, S260 (2006).

[60] J. R. Hiskes, *Cross sections for the vibrational excitation of the* $H_2X^1\Sigma_g^+(\nu)$ *levels generated by electron collisional excitation of the higher singlet states*, J. Appl. Phys. **70**, 3409 (1991).

[61] V. A. Shakatov and Yu. A. Lebedev, *Collisional-Radiative Model of Hydrogen Low-Temperature Plasma: Processes and Cross Sections of Electron-Molecule Collisions*, High Temperature **49**, 257 (2011).

[62] K. Hassouni, A. Gicquel, and M. Capitelli, *The role of dissociative attachment from Rydberg states in enhancing* H^- *concentration in moderate and low pressure* H_2 *plasma sources*, Chem. Phys. Lett. **290**, 502 (1998).

[63] B. Rasser, J. N. M. Van Wunnik, and J. Los, *Theoretical models of the negative ionization of hydrogen on clean tungsten, cesiated tungsten and cesium surfaces at low energies*, Surf. Sci. **118**, 697 (1982).

[64] K.-N. Leung and K. W. Ehlers, H^- *ion formation from a surface conversion type ion source*, J. Appl. Phys. **52**, 3905 (1981).

[65] G. D. Alton, *High-intensity, heavy negative ion sources based on the sputter principle*, Rev. Sci. Instrum. **65**, 1141 (1994).

[66] L. Schiesko, M. Carrère, J.-M. Layet, and G. Cartry, *A comparative study of H^- and D^- production on graphite surfaces in H_2 and D_2 plasmas*, Plasma Sources Sci. Technol. **19**, 045016 (2010).

[67] Yu. Belchenko, *Surface negative ion production in ion sources*, Rev. Sci. Instrum. **64**, 1385 (1993).

[68] J. K. Nørskov and B. I. Lundqvist, *Secondary-ion emission probability in sputtering*, Phys. Rev. **B** 19, 6551 (1979).

[69] O. Tarvainen, *The effects of cesium equilibrium on H^- ion beam production with LANSCE surface converter ion source*, Nucl. Instrum. Meth A **601**, 270 (2009).

[70] J. Peters, *Negative ion sources for high energy accelerators*, Rev. Sci. Instrum **71**, 1069 (2010).

[71] O. Tarvainen, T. Kalvas, J. Komppula, H. Koivisto, E. Geros, J. Stelzer, G. Rouleau, K. F. Johnson, and J. Carmichael, *Effect of Ion Escape Velocity and Conversion Surface Material on H^- Production*, 2nd International Symposium on Negative Ions, Beams and Sources, Takayama, Japan, AIP Conf. Proc. **1390**, 113 (2011).

[72] R. K. Janev, D. Reiter, and U. Samm, *Collision Processes in Low-Temperature Hydrogen Plasmas*, Berichte des Forschungszentrums, Institute für Plasmaphysik, Jülich (2003).

[73] A. V. Phelps, *Cross sections and swarm coefficients for H^+ H_2^+, H_3^+, H, H_2, and H^- in H_2 for energies from 0.1 eV to 10 keV*, J. Phys. Chem. Ref. Data **19**, 653 (1990).

[74] T. Kuo, R. Baartman, G. Dutto, S. Hahto, J. Ärje, and E. Liukkonen, *A high intensity dc H^- source for low energy injection*, Rev. Sci. Instrum. **73**, 986 (2002).

[75] Y. S. Hwang, G. Cojocaru, D. Yuan, M. McDonald, K. Jayamanna, G. H. Kim and G. Dutto, *Characterization of TRIUMF dc H^- ion sources for enhanced brightness*, Rev. Sci. Instrum **77**, 03A509 (2006).

[76] D. Riz and J. Paméla, *Modeling of negative ion transport in a plasma source*, Rev. Sci. Instrum **69**, 914 (1998).

[77] R. R. Stevens Jr., R. L. York, J. R. McConnell, R. Kandarian, *Status of the new high intensity H^- injector at LAMPF*, Proc. of the Linear Accelerator Conference, Seeheim, Germany, 1984, pp. 226–228 (`http://www.jacow.org/`).

[78] R. F. Welton, *Overview of high-brightness H^- ion sources*, Proc. of the 21st International Linear Accelerator Conference, Gyeongju, Korea, 2002, pp. 559–563 (`http://www.jacow.org/`).

[79] D. P. Moehs, *Negative hydrogen ion sources for accelerators*, IEEE T Plasma Sci. **33**, 1786 (2005).

[80] J. Peters, *Negative ion sources for high energy accelerators*, Rev. Sci. Instrum. **71**, 1069 (2000).

[81] T. Kuo, D. Yuan, K. Jayamanna, M. McDonald, R. Baartman, P. Schmor, and G. Dutto, *On the development of a 15 mA direct current H^- multicusp source*, Rev. Sci. Instrum. **67**, 1314 (1996).

[82] R. F. Welton, M. P. Stockli, S. N. Murray, and R. Keller, *Recent advances in the performance and understanding of the SNS ion source*, 10th Int. Symp. on Prod. and Neutralization of Neg. Ions and Beams, Kieve, Ukraine, AIP Conf. Proc. **763**, 296, (2004).

[83] R. F. Welton J. Carmichael, N. J. Desai, R. Fuga, R. H. Goulding, B. X. Han, Y. Kang, S. W. Lee, S. N. Murray, T. Pennisi, K. G. Potter, M. Santana, and M. P. Stockli, *The continued development of the Spallation Neutron Source external antenna H^- ion source*, Rev. Sci. Instrum. **81**, 02A727 (2010).

[84] M. Kronberger, D. Küchler, J. Lettry, Ø. Midttun, M. O'Neil, M. Paoluzzi, and R. Scrivens, *Commissioning of the new H^- source for Linac4*, Rev. Sci. Instrum. **81**, 02A708 (2010).

[85] R. Keller, O. Tarvainen, E. Chacon-Golcher, E. G. Geros, K. F. Johnson, G. Rouleau, J. E. Stelzer, and T. J. Zaugg, *H^- Ion Source Development for the LANSCE Accelerator Systems*, 1st International Symposium on Negative Ions, Beams and Sources, Aix-en-Provence, France, AIP Conf. Proc. **1097**, pp. 161–170 (2008).

[86] R. Keller, D. Cheng, R. DiGennaro, R. A. Gough, J. Greer, K. N. Leung, A. Ratti, J. Reijonen, R. W. Thomae, T. Schenkel, J. W. Staples, R. Yourd, A. Aleksandrov, M. P. Stockli, and R. W. Welton, *Ion-source and low-energy beam-transport issues with the front-end systems for the spallation neutron source*, Rev. Sci. Instrum. **73**, 914 (2002).

[87] C. D. Child, *Discharge from Hot CaO*, Phys. Rev. **32**, 492 (1911).

[88] J. R. Pierce, *Rectilinear Electron Flow in Beams*, J. Appl. Phys. **11**, 548 (1940).

[89] L. R. Grisham, C. C. Tsai, J. H. Whealton, and W. L. Stirling, *Effect of emission aperture shape upon ion optics*, Rev. Sci. Instrum. **48**, 1037 (1977).

[90] Ø. Midttun, T. Kalvas, M. Kronberger, J. Lettry, H. Pereira, C. Schmitzer, and R. Scrivens, *A new extraction system for the Linac4 H^- ion source*, Rev. Sci. Instrum. **83**, 02B710 (2012).

[91] H. Liebl, *Applied Charged Particle Optics*, Springer-Verlag, Berlin Heidelberg, 2008.

[92] H. Wollnik, *Optics of Charged Particles*, Academic Press, Inc., Orlando, Florida, 1987.

[93] V. Kumar, *Understanding the focusing of charged particle beams in a solenoid magnetic field*, Am. J. Phys. **77**, 737 (2009).

[94] R. Becker and W. B. Herrmannsfeldt, *Why π and mrad*, Rev. Sci. Instrum. **77**, 03B907 (2006).

[95] M. P. Stockli, R. F. Welton, and R. Keller, *Self-consistent, unbiased root-mean-square emittance analysis*, Rev. Sci. Instrum. **75**, 1646 (2004).

[96] K. R. Crandall and D. P. Rusthoi, *TRACE 3-D documentation*, Third edition, LA-UR-97-886, Los Alamos National Laboratory, May 1997.

[97] V. Toivanen, T. Kalvas, H. Koivisto, J. Komppula, and O. Tarvainen, *Double einzel lens extraction for the JYFL 14 GHz ECR ion source designed with IBSimu*, JINST **8**, P05003 (2013).

[98] P. W. Allison, J. D. Sherman, and D. B. Holtkamp, *An emittance scanner for intense low-energy ion beams*, IEEE Trans. Nucl. Sci. **30**, 2204 (1983).

[99] S. Humphries, *Charged Particle Beams*, John Wiley & Sons, 1990.

[100] R. Baartman and D. Yuan, *Space charge neutralization studies of an H^- beam*, Proc. of the European Particle Accelerator Conference, Rome, Italy, 1988, p. 949 (`http://www.JACoW.org/`).

[101] A. Ben Ismail, R. Duperrier, D. Uriot, and N. Pichoff, *Space charge compensation studies of hydrogen ion beams in a drift section*, Phys. Rev. ST Accel. Beams **10**, 070101 (2007).

[102] J. Sherman, M. Olivo, and E. Mariani, *H^+ beam neutralization measurements at 870 keV beam energy*, Rev. Sci. Instrum. **63**, 2776 (1992).

[103] P. Veltri, M. Cavenago, and G. Serianni, *Study of space charge compensation phenomena in charged particle beams*, Rev. Sci. Instrum. **83**, 02B709 (2012).

[104] N. Chauvin, O. Delferrière, R. Duperrier, R. Gobin, P. A. P. Nghiem, and D. Uriot, *Transport of intense ion beams and space charge compensation issues in low energy beam lines*, Rev. Sci. Instrum. **83**, 02B320 (2012).

[105] H. C. Kim, F. Iza, S. S. Yang, M. Radmilović, and J. K. Lee, *Particle and fluid simulations of low-temperature plasma discharges: benchmarks and kinetic effects*, J. Phys. D **38**, R283 (2005).

[106] C. K. Birdsall and A. B. Langdon, *Plasma Physics via Computer Simulation*, McGraw-Hill, Inc., 1985.

[107] E. Chacon-Golcher and K. J. Bowers, *Particle-in-Cell with Monte Carlo Collisions Gun Code Simulations of a Surface-Conversion H^- Ion Source*, Commun. Comput. Phys. **4**, 659 (2008).

[108] S. Mattei, M. Ohta, A. Hatayama, J. Lettry, Y. Kawamura, M. Yasumoto, and C. Schmitzer, *RF Plasma modeling of the Linac4 H^- ion source*, 3rd International Symposium on Negative Ions, Beams and Sources, Jyväskylä, Finland, AIP Conf. Proc. **1515**, 386 (2013).

[109] S. Mochalskyy, A. F. Lifschitz, and T. Minea, *3D modelling of negative ion extraction from a negative ion source*, Nucl. Fusion **50**, 105011 (2010).

[110] S. Mochalskyy, A. F. Lifschitz, and T. Minea, *Extracted current saturation in negative ion sources*, J. Appl. Phys. **111**, 113303 (2012).

[111] F. Taccogna, P. Minelli, P. Diomede, S. Longo, M. Capitelli, and R. Schneider, *Particle modelling of the hybrid negative ion source*, Plasma Sources Sci. Technol. **20**, 024009 (2011).

[112] G. Fubiani, G. J. M. Hagelaar, J. P. Boeuf, and S. Kolev, *Modeling a high power fusion plasma reactor-type ion source: Applicability of particle methods*, Phys. Plasmas **19**, 043506 (2012).

[113] D. C. Carey, K. L. Brown, and F. Rothacker, *Third-Order TRANSPORT with MAD Input — A Computer Program for Designing Charged Particle Beam Transport Systems*, FERMILAB-Pub-98/310, Fermi National Accelerator Laboratory, October 1998.

[114] Simion, Scientific Instrument Services, Inc., `http://simion.com/`.

[115] Vector Fields Opera, Cobham plc., `http://www.cobham.com/`.

[116] Lorentz, Integrated Engineering Software, `http://www.integratedsoft.com/`.

[117] S. A. Self, *Exact solution of the collisionless plasma-sheath equation*, Phys. Fluids **6**, 1762 (1963).

[118] J. H. Whealton, *Optics of single-stage accelerated ion beams extracted from a plasma*, Rev. Sci. Instrum. **48**, 829 (1977).

[119] J. H. Whealton, E. F. Jaeger, and J. C. Whitson, *Optics of ion beams of arbitrary perveance extracted from a plasma* J. Comp. Phys. **27**, 32 (1978).

[120] J. E. Boers, *PBGUNS: a Digital Computer Program for the Simulation of Electron and Ion Beams on a PC*, International Conference on Plasma Sciences, Vancouver, BC, 7–9 June 1993.

[121] R. Becker, IGUN — *A program for the simulation of positive ion extraction including magnetic fields*, Rev. Sci. Instrum. **63**, 2756 (1992).

[122] P. Spädtke, *KOBRA3-INP User Manual*, 2000.

[123] T. Kalvas, *Ion Beam Simulator*, The distribution website of IBSimu code, `http://ibsimu.sourceforge.net/`.

[124] S. D. Kovaleski, *Calculation of the ion extraction boundary of a plasma ion source*, IEEE Trans. Plasma Science **34**, 23 (2006).

[125] R. Becker, *NIGUN: A two-dimensional simulation program for the extraction of H^- ions*, Rev. Sci. Instrum. **75**, 1723 (2004).

[126] R. Becker, *Mathematical formulation and numerical modelling of the extraction of H^- ions*, 10th Int. Symp. on Prod. and Neutralization of Neg. Ions and Beams, Kieve, Ukraine, AIP Conf. Proc. **763**, 194 (2005).

[127] A. R. Mitchell and D. F. Griffiths, *The Finite Difference Method in Partial Differential Equations*, Wiley, New York, 1980.

[128] S. Humphries, *Finite-element Methods for Electromagnetics*, `http://www.fieldp.com/femethods.html`, 2010.

[129] C. A. Brebbia, J. C. F. Telles, and L. C. Wrobel, *Boundary Element Techniques: Theory and Applications in Engineering*, Springer-Verlag, Berlin, 1984.

[130] L. Rineau, *Maillages de volumes bornés par des surfaces lisses par morceaux*, Ph. D. Thesis, Université Paris-Diderot — Paris VII, France, 2007.

[131] L. Rineau and M. Yvinec, *A generic software design for Delaunay refinement meshing*, Comput. Geom. Theory Appl., **38**, 100 (2007).

[132] D. Cubric, B. Lencova, F. H. Read, and J. Zlamal, *Comparison of FDM, FEM and BEM for electrostatic charged particle optics*, Nucl. Instrum. Meth. A **427**, 357 (1999).

[133] F. A. Fernandez and L. Kulas, *A simple finite difference approach using unstructured meshes from FEM mesh generators*, Proc. of 15th International Conference on Microwaves, Radar and Wireless Communications, Warsow, Poland, 2004, pp. 585–588.

[134] W. E. Lorensen and H. E. Cline, *Marching cubes: a high resolution 3D surface construction algorithm*, Computer Graphics **21**, 163, (1987).

[135] G. M. Nielson and B. Hamann, *The asymptotic decider: resolving the ambiguity in marching cubes*, Proc. of the 2nd conference on Visualization, San Diego, California, 1991, pp. 83–91.

[136] R. Segura, F. R. Feito, J. Ruiz de Miras, C. Ogayar, and J. C. Torres, *An Efficient Point Classification Algorithm for Triangle Meshes*, Journal of Graphics, GPU, and Game Tools **10**, 27, (2005).

[137] Y. Saad, *Iterative Methods for Sparse Linear Systems*, 2nd edition, Society of Industrial and Applied Mathematics, Philadelphia, 2003.

[138] R. Barrett, M. Berry, T. F. Chan, J. Demmel, J. Donato, J. Dongarra, V. Eijkhout, R. Pozo, C. Romine, and H. Van der Vorst, *Templates for the Solution of Linear Systems: Building Blocks for Iterative Methods, 2nd Edition*, SIAM, Philadelphia, PA, 1994.

[139] J. M. Ortega and W. C. Rheinboldt, *Iterative Solution of Nonlinear Equations in Several Variables*, Academic Press, New York, NY, 1970.

[140] T. A. Davis, *Algorithm 832: UMFPACK, an unsymmetric-pattern multifrontal method*, ACM Transactions on Mathematical Software **30**, 196 (2004).

[141] H. A. van der Vorst, *Bi-CGSTAB: A fast and smoothly converging variant of Bi-CG for the solution of nonsymmetric linear systems*, SIAM J. Sci. Statist. Comput. **13**, 631 (1992).

[142] A. Brandt, *Multi-Level Adaptive Solutions to Boundary-Value Problems*, Mathematics of Computation **31**, 333 (1977).

[143] Z. C. Li, C. S. Chien, and H. T. Huang, *Effective condition number for finite difference method*, Journal of Comp. Appl. Math. **198**, 208 (2007).

[144] I. M. Sobol, *On the distribution of points in a cube and the approximate evaluation of integrals*, Zh. Vychisl. Mat. Mat. Fiz. **7**, 784–802 (1967).

[145] C. F. Chan, W. S. Cooper, J. W. Kwan, and W. F. Steele, *Dynamics of skew beams and the projectional emittance*, Nucl. Instrum. Meth. A **306**, 112 (1991).

[146] M. Galassi et al., *GNU Scientific Library Reference Manual*, 3rd Ed., v 1.12 (2009).

[147] J. H. Whealton, *Ion extraction and optics arithmetic*, Nucl. Instrum. Meth. **189**, 55 (1981).

[148] I. Langmuir and K. B. Blodgett, *Currents limited by space charge between coaxial cylindrers*, Phys. Rev. **22**, 347 (1923).

[149] I. Langmuir and K. B. Blodgett, *Currents Limited by Space Charge between Concentric Spheres*, Phys. Rev. **24**, 49 (1924).

[150] M. Cavenago and G. Bisoffi, *Cylindrically symmetric extractors with space charge dominated flow*, Rev. Sci. Instrum **62**, 1970 (1991).

[151] R. Becker and R. A. Jameson, *Emittance growth as mesh artefact*, Nucl. Instrum. Meth. A **558**, 32 (2006).

[152] T. Kalvas, S. K. Hahto, F. Giquel, M. King, H. Vainionpää, J. Reijonen, K. N. Leung, and T. G. Miller, *Fast slit-beam extraction and chopping for neutron generator*, Rev. Sci. Instrum. **77**, 03B904 (2006).

[153] J. Lettry, J. Alessi, D. Faircloth, A. Gerardin, T. Kalvas, H. Pereira, and S. Sgobba, *Investigation of ISIS and Brookhaven National Laboratory ion source electrodes after extended operation*, Rev. Sci. Instrum. **83**, 02A728 (2012).

[154] D. C. Faircloth, S. Lawrie, A. Letchford, C. Gabor, M. Perkins, M. Whitehead, T. Wood, O. Tarvainen, J. Komppula, T. Kalvas, V. Dudnikov, H. Pereira, J. Simkin, and S. Elliot, *Developing the RAL FETS source to deliver a 60 mA, 50 Hz, 2 ms H^- Beam*, 3rd International Symposium on Negative Ions, Beams and Sources, Jyväskylä, Finland, AIP Conf. Proc. **1515**, 359 (2013).

[155] Z. Izaola, A. Zugazaga, J. Feuchtwanger, D. Fernández-Cañoto, I. Bustinduy, J. L. Munoz, D. Faircloth, and S. R. Lawrie, *Upgrade of the ITUR extraction system at ESS-Bilbao*, 3rd International Symposium on Negative Ions, Beams and Sources, Jyväskylä, Finland, AIP Conf. Proc. **1515**, 587 (2013).

[156] *A proposed facility upgrade for the Texas A&M University Cyclotron Institute*, White paper, Texas A&M University, 2001.

[157] G. Tabacaru, D. P. May, J. Arje, G. Chubarian, H. Clark, G. J. Kim, and R. E. Tribble, *The rare isotope beams production at the Texas A&M university Cyclotron Institute*, 22nd International Conference on Application of Accelerators in Research and Industry, Ft. Worth, TX, USA, AIP Conf. Proc. **1525**, 507 (2012).

[158] J. Reijonen, P. Heikkinen, E. Liukkonen, and J. Ärje, *An improved extraction for the multicusp-type light ion-ion source apparatus*, Rev. Sci. Instrum. **69**, 1138 (1998).

[159] O. Chubar, P. Elleaume, and J. Chavanne, *Radia3D — A computer program for calculating static magnetic fields*,

http://www.esrf.eu/Accelerators/Groups/InsertionDevices/Software/Radia/

[160] R. Thomae, R. Gough, R. Keller, K. N. Leung, T. Schenkel, A. Aleksandrov, M. Stockli, and R. Welton, *Beam measurements on the H⁻ source and low energy beam transport system for the Spallation Neutron Source*, Rev. Sci. Instrum. **73**, 2016 (2002).

[161] A. Ratti, C. Fong, M. Fong, R. MacGill, R. Gough, J. Staples, M. Hoff, R. Keller, S. Virostek, and R. Yourd, *Conceptual Design of the SNS RFQ*, Proc. of the 19th International Linac Conference, Chicago, IL, USA, 1998, pp. 276–278 (http://www.jacow.org/).

[162] R. Keller, W. Abraham, J. J. Ayers, D. W. Cheng, P. Cull, R. DiGennaro, L. Doolittle, R. A. Gough, J. B. Greer, M. D. Hoff, K.-N. Leung, S. Lewis, C. Lionberger, R. MacGill, Y. Minamihara, M. Monroy, D. Oshatz, J. Pruyn, A. Ratti, J. Reijonen, T. Schenkel, J. W. Staples, D. Syversrud, R. Thomae, S. Virostek, and R. Yourd, *Progress with the SNS front-end systems*, Proc. of the 19th Particle Accelerator Conference, Chicago, IL, 2001, pp. 70–72 (http://www.jacow.org/).

[163] M. P. Stockli, private communications, 2012.

[164] B. X. Han, T. Kalvas, O. Tarvainen, R. F. Welton, S. N. Murray, Jr., T. R. Pennisi, M. Santana, and M. P. Stockli, *Low-energy beam transport studies supporting the spallation neutron source 1-MW beam operation*, Rev. Sci. Instrum. **83**, 02B727 (2012).

[165] M. P. Stockli, K. D. Ewald, B. X. Han, S. N. Murray Jr., T. R. Pennisi, C. Piller, M. Santana, J. Tang, R. F. Welton, *Recent Performance of the SNS H⁻ Ion Source and Low-Energy Beam Transport System*, to be published in Rev. Sci. Instrum.

[166] B. X. Han, M. P. Stockli, R. F. Welton, T. R. Pennisi, S. N. Murray, M. Santana, and C. D. Long, *Emittance studies of the Spallation Neutron Source external-antenna H⁻ ion source*, Rev. Sci. Instrum. **81**, 02B721 (2010).

[167] B. X. Han and M. P. Stockli, *The new LEBT for the spallation neutron source power upgrade project*, Proc. of the 22nd Particle Accelerator Conference, Albuquerque, NM, USA, 2007, pp. 1823–1825 (http://www.jacow.org/).

[168] B. X. Han, D. J. Newland, W. T. Hunter, and M. P. Stockli, *Physics design of a prototype 2-solenoid LEBT for the SNS injector*, Proc. of the 24th Particle Accelerator Conference, New York, NY, USA, 2011, pp. 1564–1566 (http://www.jacow.org/).

[169] R. F. Welton, N. J. Desai, B. X. Han, E. A. Kenik, S. N. Murray, T. R. Pennisi, K. G. Potter, B. R. Lang, M. Santana, and M. P. Stockli, *Ion source development at the SNS*, Proc. of the 2nd International Symposium on Negative Ions, Beams and Sources, Takayama, Japan, 2010, pp. 226–234.

[170] Ø. Midttun, J. Lettry, and R. Scrivens, *Measurement of Linac4 H^- ion source beam with a magnetized einzel lens electron dump*, to be published in Rev. Sci. Instrum.

[171] D. C. Meeker, Finite Element Method Magnetics, Version 4.0.1. (3 Dec 2006 build), `http://www.femm.info/`.

[172] J. Sherman, E. Pitcher, R. Stevens, and P. Allison, *H^- beam neutralization measurements in a solenoidal beam transport system*, 6th International Symposium on the Production and Neutralization of Negative Ions and Beams, Upton, New York, USA, AIP Conf. Proc. **287**, 686 (1992).

[173] R. Norarat, T. Sajavaara, M. Laitinen, P. Heikkinen, K. Ranttila, K. Ylikorkala, V. Hänninen, M. Rossi, P. Jones, V. Marjomäki, L. Gilbert, and H. J. Whitlow, *Development of the Jyväskylä microbeam facility*, Nucl. Instrum. Meth. B **272**, 158 (2012).

[174] P. Heikkinen, *Commissioning of the JYFL MCC30/15 Cyclotron*, Proc. of the 19th International Conference on Cyclotrons and Their Applications, Lanzhou, China, 2010, p. 310 (`http://www.jacow.org/`).

[175] Y. An, W. H. Cho, K-J Chung, K. Lee, S. B. Jang, S. G. Lee, and Y. S. Hwang, *Wave frequency dependence of H^- ion production and extraction in a transformer coupled plasma H^- ion source at SNU*, Rev. Sci. Instrum. **83**, 02A727 (2012).

[176] H. Koivisto, P. Suominen, O. Tarvainen, and D. Hitz, *A modified permanent magnet structure for a stronger multipole magnetic field*, Rev. Sci. Instrum. **75**, 1479 (2004).

[177] H. Pereira, J. Lettry, J. Alessi and T. Kalvas, *Estimation of Sputtering Damages on a Magnetron H^- Ion Source Induced by Cs^+ and H^+ Ions*, 3rd International Symposium on Negative Ions, Beams and Sources, Jyväskylä, Finland, AIP Conf. Proc. **1515**, 81 (2013).

[178] C. A. Valerio-Lizarraga, J.-B. Lallement, I. Leon-Monzon, J. Lettry, Ø. Midttun, R. Scrivens, *Space Charge Compensation in the Linac4 Low Energy Beam Transport Line with Negative Hydrogen Ions*, to be published in Rev. Sci. Instrum.

[179] G. R. Brewer, *Focusing of high-density electron beams* in *Focusing of charged particles, Vol. II*, edited by A. Septier, Academic Press, New York, pp. 73–121, 1967.